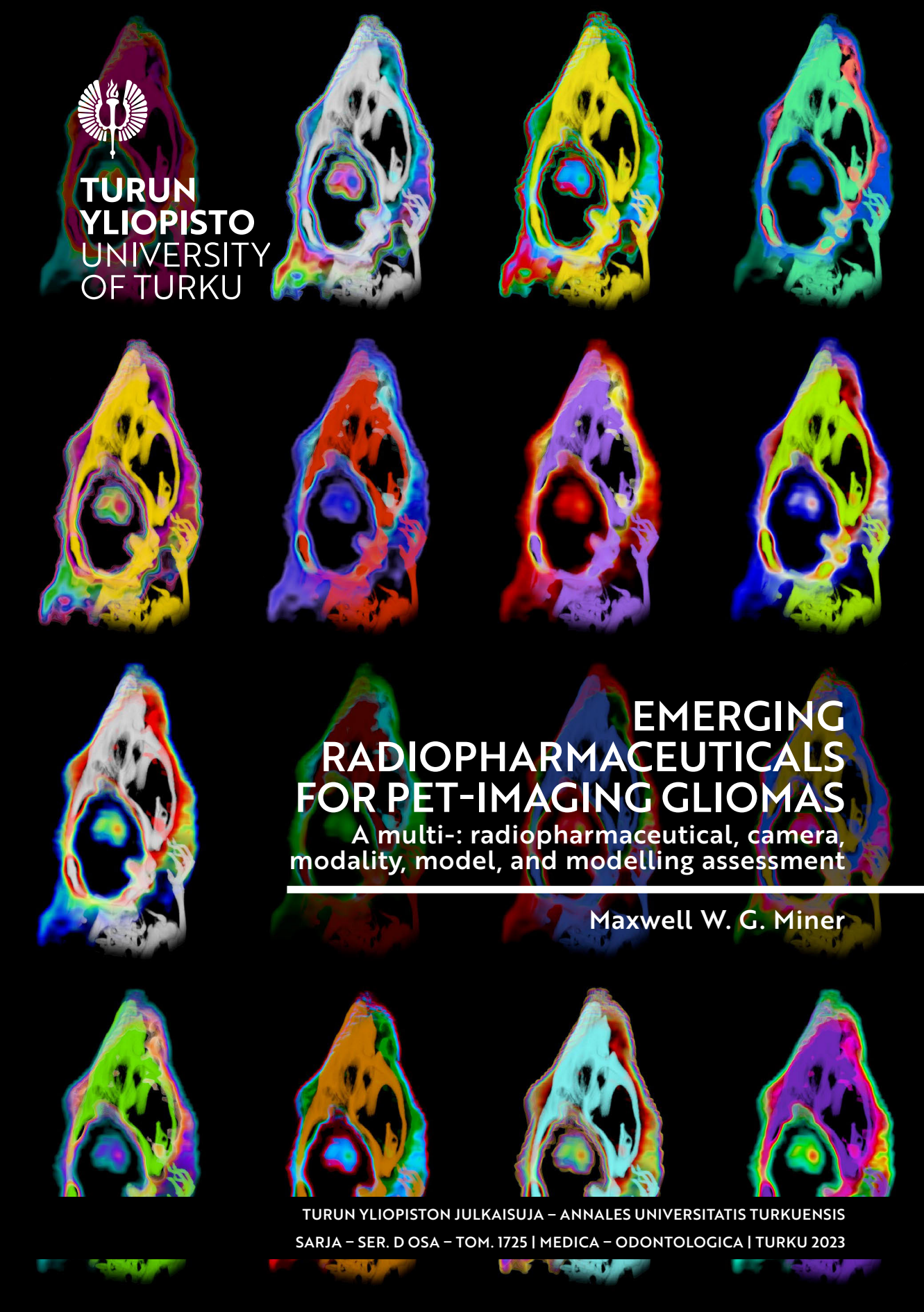

TURUN YLIOPISTO
UNIVERSITY OF TURKU

EMERGING RADIOPHARMACEUTICALS FOR PET-IMAGING GLIOMAS

A multi-: radiopharmaceutical, camera, modality, model, and modelling assessment

Maxwell W. G. Miner

TURUN YLIOPISTON JULKAISUJA – ANNALES UNIVERSITATIS TURKUENSIS
SARJA – SER. D OSA – TOM. 1725 | MEDICA – ODONTOLOGICA | TURKU 2023

TURUN
YLIOPISTO
UNIVERSITY
OF TURKU

EMERGING RADIOPHARMACEUTICALS FOR PET-IMAGING GLIOMAS

A multi-: radiopharmaceutical, camera, modality, model, and modelling assessment

Maxwell W. G. Miner

TURUN YLIOPISTON JULKAISUJA – ANNALES UNIVERSITATIS TURKUENSIS
SARJA – SER. D OSA – TOM. 1725 | MEDICA – ODONTOLOGICA | TURKU 2023

University of Turku

Faculty of Medicine
Department of Clinical Physiology and Nuclear Medicine
Drug Research Doctoral Programme (DRDP)
Turku PET Centre

Supervised by

Professor Anne Roivainen, PhD
Turku PET Centre and
Turku Center for Disease Modeling
University of Turku
Turku, Finland

Assistant Professor Xiang Guo-Li, PhD
Department of Chemistry and
Turku PET Centre
University of Turku
Turku, Finland

Reviewed by

Docent, Kirsi Timonen, MD, PhD
Ylilääkäri | Chief physician
Sairaala Nova, Hospital Nova
Wellbeing Services County of
Central Finland
Jyväskylä, Finland

Docent, Kim Bergström, PhD
Ylikemisiti | Chief Clinical Chemist
HUS Diagnostic Center Cyclotron Unit
HUS Group, the joint authority for
Helsinki and Uusimaa
Helsinki, Finland

Opponent

Professor Klaus Kopka, PhD
Director of the Institute of Radiopharmaceutical Cancer Research
Helmholtz-Zentrum Dresden-Rossendorf (HZDR)
Dresden, Germany

The originality of this publication has been checked in accordance with the University of Turku quality assurance system using the Turnitin Originality Check service.

Cover Image: Maxwell W. G. Miner

ISBN 978-951-29-9337-6 (PRINT)
ISBN 978-951-29-9338-3 (PDF)
ISSN 0355-9483 (Print)
ISSN 2343-3213 (Online)
Painosalama, Turku, Finland 2023

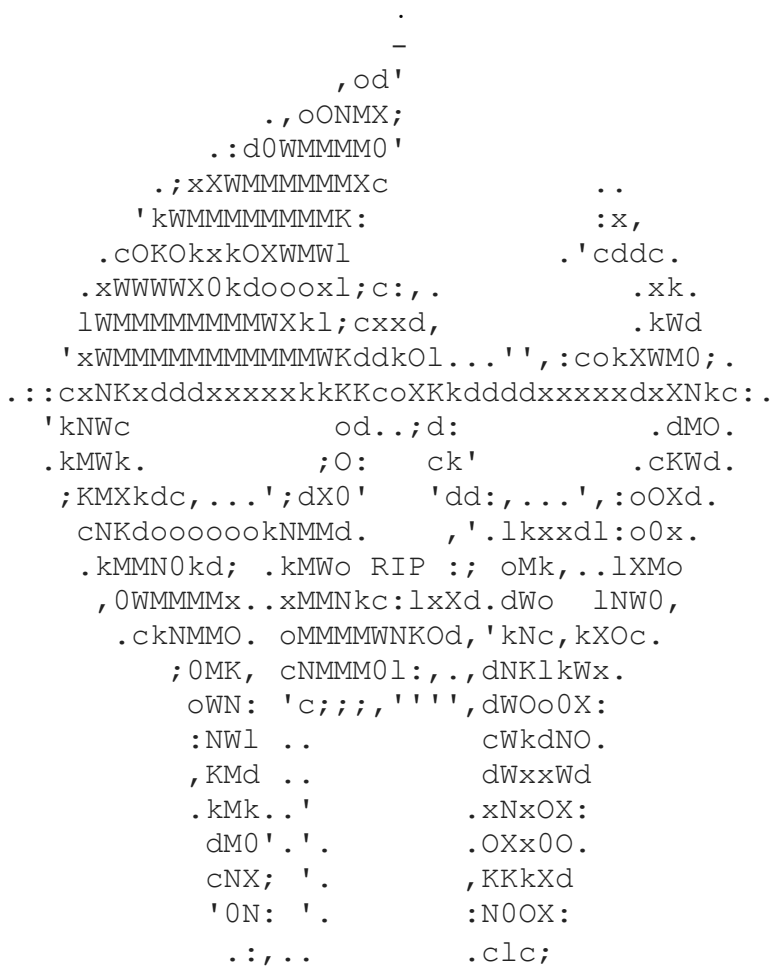

Thanks for the poetic inspiration throughout these years, Daniel

-M

UNIVERSITY OF TURKU
Faculty of Medicine
Clinical Physiology and Nuclear Medicine
MAXWELL W. G. MINER: Emerging radiopharmaceuticals for PET-imaging gliomas. A multi-: radiopharmaceutical, camera, modality, model, and modelling assessment
Doctoral Dissertation, 205 pp.
Drug Research Doctoral Programme (DRDP)
June 2023

ABSTRACT

Gliomas, which are a type of brain tumour derived from the non-neuronal and nutrient-supplying glial cells of the brain, are particularly devastating disease due to the importance and delicate nature of cerebral matter. Surgical removal, chemotherapy, and radiation therapy often have unwanted consequences depending on a variety of physiological and probability factors. With the human life expectancy averaging 12–15 months after clinical diagnosis (with treatment) for aggressive brain tumours, accurately detecting and characterizing these tumours non-invasively is important for treatment planning. Currently, the highest anatomical resolution imaging modality available for brain imaging is magnetic resonance imaging (MRI), but this lacks biochemical information. Positron emission tomography paired with computed tomography for anatomical reference (PET-CT) divulges quantifiable biochemical information. By selecting imaging radiopharmaceuticals for PET imaging that have relevance to tumour surface proteins or other cellular metabolic processes it is possible to not only aid in detecting or delineating gliomas, but also gain specific biochemical-property insight into these lesions.

The aim of these studies was to evaluate the two emerging radiopharmaceuticals (2*S*, 4*R*)-4-[^{18}F]fluoroglutamine ([^{18}F]FGln) and Al[^{18}F]F-NOTA-Folate ([^{18}F]FOL) and to directly compare them with routinely clinically-used radiopharmaceuticals 2-deoxy-2-[^{18}F]fluoro-D-glucose ([^{18}F]FDG) and L-[^{11}C]methionine ([^{11}C]Met) for the PET imaging of gliomas in animal models. Other parameters, such as the *in vivo* stability, *ex vivo* biodistribution, *in vitro* binding and blocking, and the presence of relevant receptors on human tissue samples were investigated in to divulge additional information.

The results demonstrated that both [^{18}F]FGln and [^{18}F]FOL provided an enhanced level of contrast between tumour and adjacent non-tumour brain tissue versus that of the clinically used radiopharmaceuticals [^{18}F]FDG and [^{11}C]Met in animal models.

KEY WORDS: glioma, cancer, positron emission tomography, fluoroglutamine, folate

TURUN YLIOPISTO
Lääketieteellinen tiedekunta
Kliininen fysiologia ja isotooppilääketiede
MAXWELL W. G. MINER: Uudet radiolääkeaineet glioomien PET-kuvantamiseen. Tutkimuksia radiolääkeaineista, modaliteeteista, kameroista, kokeellisista malleista ja mallintamisesta
Väitöskirja, 205 s.
Lääketutkimuksen tohtoriohjelma
Kesäkuu 2023

TIIVISTELMÄ

Glioomat ovat aivokasvaimia, jotka syntyvät ravinteiden kuljetusta hoitavista glia- eli hermotukisoluista. Ne ovat erityisen tuhoisia sairauksia aivokudoksen tärkeyden ja herkkyyden vuoksi. Kirurgisella leikkauksella, kemoterapialla, ja sädehoidolla on usein ei-toivottuja seurauksia riippuen fysiologisista ja todennäköisyystekijöistä. Koska elinajanodote aggressiivisen aivokasvaimen diagnoosin jälkeen on keskimäärin 12–15 kuukautta (hoidon kanssa), ei-invasiivinen tarkka havaitseminen ja karakterisointi on tärkeää hoidon suunnittelussa. Tällä hetkellä parhaat työkalut aivojen kuvantamiseen ovat magneettikuvaus (MRI), joka mahdollistaa parhaimman anatomisen tarkkuuden, ja positroniemissiotomografia (PET), joka paljastaa biokemiallisen informaation.

Valitsemalle PET-kuvantamiseen radiolääkeaine, joka kiinnittyy syöpäsolun pintaproteiineihin tai liittyy solun aineenvaihduntaprosessiin on mahdollista paitsi havaita tai rajata glioomia, myös saada erityistä biokemiallista tietoa näistä leesioista.

Tämän tutkimuksen tavoitteena oli arvioida kahta uutta radiolääkeainetta; (2*S*, 4*R*)-4-[^{18}F]fluoriglutamiinia ([^{18}F]FGln) ja Al[^{18}F]F-NOTA-folaattia ([^{18}F]FOL) ja verrata niitä kliinisessä käytössä oleviin 2-deoxy-2-[^{18}F]fluori-D-glukoosiin ([^{18}F]FDG) ja L-[^{11}C]metioniiniin ([^{11}C]Met) glioomien PET-kuvantamisessa. Stabiilisuutta, biologista jakautumista, sitoutumista ja sitoutumisen salpautumista, sekä farmakokineettista mallintamista tutkittiin *in vivo*, *ex vivo* ja *in vitro* olosuhteissa eläinmalleissa ja kudosnäytteillä.

Tulokset osoittivat, että eläinmalleissa sekä [^{18}F]FGln että [^{18}F]FOL mahdollistavat paremman kontrastin tuumorin ja viereisen tuumorittoman aivokudoksen välillä verrattuna kliinisessä käytössä oleviin [^{18}F]FDG ja [^{11}C]Met radiolääkeaineisiin.

AVAINSANAT: glioma, syöpä, positroniemissiotomografia, fluoroglutamiini, folaatti

Table of Contents

Abbreviations

[^{11}C]Met	L-[^{11}C]methionine
[^{18}F]FDG	2-deoxy-2-[^{18}F]fluoro-D-glucose
[^{18}F]FET	L-[^{18}F]fluoroethyl-tyrosine
[^{18}F]FOL	Aluminium fluorine-18 labelled 1,4,7-triazacylononane-1,4,7-triacetic acid-conjugated folate analogue, Al[^{18}F]F-NOTA-Folate
[^{18}F]FGln	(2*S*, 4*R*)-4-[^{18}F]fluoroglutamine
A	Adenine
BAT	Brown adipose tissue
BBB	Blood-brain-barrier
Boc	tertiary-butyloxycarbonyl
C	Cytosine
CNS	Central nervous system
CSF	Cerebral spinal fluid
CT	Computed tomography (most often referring to x-ray imaging source)
DAPI	4',6-diamindino-2phenylindole; fluorescent dye for staining cellular nuclei
DNA	Deoxyribonucleic acid
EGFR	Epidermal growth factor receptor
FR	Folate receptor
FR-α	Folate receptor-alpha
FR-β	Folate receptor-beta
G	Guanine
GBI	Glioblastoma isocitrate dehydrogenase (gene)-wild type
GBM	Glioblastoma multiforme (term no longer used and replaced by other more-specific classification terms such as GBI in 2021)
H&E	Haematoxylin and Eosin
HPLC	High performance liquid chromatography
IDH	Isocitrate dehydrogenase (protein, when italicised: referring to gene)
MRI	Magnetic resonance imaging
mRNA	Messenger ribonucleic acid
MTHFD	Methenyltetrahydrofolate reductase
NOTA	1,4,7-triazacylononane-1,4,7-triacetic acid
OTs	Tosylate (where the "O" is oxygen linking to the tosyl-group)

PBS	Phosphate-buffered saline
PEG	Polyethylene glycol
PET	Positron emission tomography
PSL	Photostimulated luminescence
RCY	Radiochemical yield
RFC	Reduced Folate Carrier (family of transmembrane transport proteins)
RNA	Ribonucleic acid
ROI	Region of interest (referring to an area or volume of a 2 or 3D image
S19A1	Solute carrier family 19, member 1 (protein)
STUK	Säteilyturvakeskus (fi), Radiation and Nuclear Safety Authority of Finland (en)
SUV	Standardized uptake value
T	Thymidine
t-Bu	Tertiary-butyl
TBR	Tumour to brain ratio; (Tumour mean)/(brain mean)
TBR_{peak}	Maximum TBR reached during a frame over the duration of a dynamic PET image; (Tumour mean at peak (t))/(brain mean (t))
TCA	The citric acid cycle (aka: Krebs cycle, or tricarboxylic acid cycle)
TERT	Telomerase reverse transcriptase
TFA	Trifluoroacetic acid
Tmob	*S*-2,4,6-trimethoxybezly
WAT	White adipose tissue

List of Original Publications

This dissertation is based on the following original publications, which are referred to in the text by their Roman numerals:

I **Maxwell W.G. Miner**, Heidi Liljenbäck, Jenni Virta, Joni Merisaari, Vesa Oikonen, Jukka Westermarck, Xiang-Guo Li, Anne Roivainen. (2*S*, 4*R*)-4-[^{18}F]fluoroglutamine for *in vivo* PET imaging of glioma xenografts in mice: an evaluation of multiple pharmacokinetic models. *Molecular Imaging and Biology* 22(4):969-978, 2020.

II **Maxwell W.G. Miner**, Heidi Liljenbäck, Jenni Virta, Semi Helin, Olli Eskola, Petri Elo, Jarmo Teuho, Kerttu Seppälä, Vesa Oikonen, Guangli Yang, Andrea Kindler-Röhrborn, Heikki Minn, Xiang-Guo Li, Anne Roivainen. Comparison of: (2*S*, 4R)-4-[^{18}F]Fluoroglutamine,[^{11}C]Methionine, and 2-Deoxy-2-[^{18}F]Fluoro-D-Glucose and Two Small-Animal PET/CT Systems Imaging Rat Gliomas. *Frontiers in Oncology* 11:730358, 2021.

III **Maxwell W.G. Miner**, Heidi Liljenbäck, Jenni Virta, Salli Kärnä, Riikka Viitanen, Petri Elo, Maria Gardberg, Jarmo Teuho, Piritta Saipa, Johan Rajander, Hasan Mansour A Mansour, Nathan A. Cleveland, Philip S. Low, Xiang-Guo Li, Anne Roivainen. High folate receptor expression in gliomas can be detected in vivo using folate-based positron emission tomography with high tumour-to-brain uptake ratio divulging potential future targeting possibilities. *Frontiers in Immunology* 14:2410, 2023.

1 Introduction

The accumulation of random DNA mutations can sometimes build up and escape corrective methods employed by a cell. When an organism fails to amend such errors and they accumulate with enough detrimental properties, the result can be an out-of-control replicating cancerous mass (Weinberg, 2013). The plethora of different types of cells and genes in a mammal, let alone additionally different genetic individuals, can make each cancer almost unique. Some specific mutations are more common and thus can be generally grouped together as a "type of cancer" based on their cellular origins. These types of cancers can then be further subtyped by specific genetic mutations to describe biologically relevant properties. The wide variety of cancers that exist can make generalized detection and treatment difficult, though the scientific community is continually pushing the boundaries of what is possible through personalized-medicine approaches matched to each cancer type. The personalized specific treatment of cancer is not the only important factor in patient care. The detection and biochemical characterization of cancerous lesions is also a crucial factor in planning treatment approaches so that time is not wasted on ineffective care strategies.

Since the invention of the positron emission tomography (PET) camera in the 1970's (Phelps *et al.*, 1975), the device has undergone extraordinary development both in terms of image reconstruction mathematics and physical hardware. It is often coupled with MRI or CT imaging (PET-MRI and PET-CT respectively) to overlay higher resolution structural images for spatial reference. PET imaging has also caused the field of radiochemistry to have its most useful purpose actualized: The non-invasive imaging and quantification of biochemical processes within living subjects. Nuclear medicine and PET imaging has come a very long way since their inception and the continued development of new radiopharmaceuticals remains as another exciting frontier of science with a multitude of useful imaging compounds being continually discovered. With personalized medicine being a considerable focus of modern healthcare, PET imaging is poised to join the party whereby oncologists can potentially select imaging compounds specific to each patient's cancer type and even genetic subtype to get the best image to guide treatments. It is also possible for radiopharmaceuticals to be used to classify genetic markers of

cancerous lesions and predict whether a therapeutic approach based on the same cellular markers may have a positive impact (Naqa, 2014).

Head and neck cancers, particularly brain tumours, can be difficult to treat due to the complex delicate nature of the nervous system. Not only are brain matter and the spinal cord extraordinarily delicate, but they are also essential for movement and mental function. It is understood by most that exploratory brain surgery to examine a tumour's genotype, size and boundaries is not ideal. By attaching a detectable radionuclide (radiolabelling) to a cancer-relevant molecule, it is possible to track the molecule's accumulation via PET imaging. The most common example of this approach is with 2-deoxy-2-[^{18}F]fluoro-D-glucose ([^{18}F]FDG) which is an analogue of glucose (Macheda, Rogers and Best, 2005). Through tracking the accumulation of cellular energy in the form of [^{18}F]FDG, it is possible to detect anomalous cells that are amassing an increased amount of this sugar analogue. One of the hallmarks of cancer is uncontrolled replication and this inherently requires a high amount of cellular energy to fuel this task. In this way it is possible to non-invasively detect cancer lesions or other biological phenomena that utilize additional levels of glucose (Kelloff *et al.*, 2005).

Many different radiopharmaceuticals are currently produced worldwide with countless more waiting to be discovered and developed. Selecting the appropriate imaging agent for each patient's specific cancer type may improve imaging ability and even patient outcomes (Fani, Peitl and Velikyan, 2017; Barca *et al.*, 2021). Thoroughly testing and analysing newly emerging radiopharmaceuticals for this purpose is essential to the continued development of the field of radiochemistry, furthers the understanding of biochemical processes in the body, and ultimately results in better disease-treatment outcomes.

2 Review of the Literature

2.1 Gliomas and Brain Cancer Foreword

The development of cancer for any organism is an inherently complex subject due to not only the wide variety of cancers for single species, but also cancer subtypes, genetic and phenotypic differences. Although there are traits that make a cancer, or a group of types of cancers, more treatable, there are plethora of additional factors that can influence patient outcomes. Biopsy often plays a critical role in the treatment process since, here, a cancerous cell sample is removed and can be tested for various properties. This type of biopsy is always taken with brain tumours due to the extremely delicate nature of the brain, though can be obtained if deemed helpful for patient treatment planning. Post-biopsy sample tests can include looking for specific cell receptors, morphological characteristics, numerous other properties, or the cells can even be grown in cell culture for additional testing and research (Robert H. Whitehead *et al.*, 1985; Herreño *et al.*, 2018). The additional information gleamed from such a sample can be invaluable. For example: if a tested breast cancer cellular sample indicated that the cells do not possess estrogen receptors, hormone therapy based on this receptor would be a waste of potentially precious time (Ostrom *et al.*, 2018).

The development of a glioma, which is a type of brain tumour originating from the glial cells in the central nervous system (CNS), is a relatively uncommon and rare form of cancer affecting around 6 of 100,000 people (0.06%) . The patient outcomes are, however, especially grim due to a combination of the often-aggressive nature of the tumours and delicate properties of the brain and CNS. An aggressive glioblastoma is a particularly devastating form of this cancer found in humans. Even with treatment, the average survival time is a mere 12-15 months (Bernard and Christopher, 2014 WHO World Cancer Report). On the other hand, a patient with a benign or slow-growing low grade glioma may benefit more from a less aggressive treatment approach while experiencing decades of relatively normal life (Oberheim Bush and Chang, 2016).

> *But how to quickly and effectively determine whether it is aggressive or benign without removing a sample and testing it?*

With particularly delicate organs such as the brain, there are inherent additional risks for taking a tumour sample via biopsy when compared with other cancer types such as, for example, breast cancer. While it is not uncommon for a glioma needle biopsy to be taken from a patient, there still exists some controversy and conflicting opinions on whether a higher risk of surgical morbidity will have an overall more detrimental effect on the average patient in comparison with the additional information gleamed from such a sample (Jiang *et al.*, 2017). It is possible that due to the large variability in glioma and brain tumour development in general, a personalized approach on a case-by-case basis may benefit the patient the most. For this reason, modern reviews of literature attempting to examine the patient outcomes while comparing whether initial needle biopsy or total surgical resections yielded inconclusive results (Hart *et al.*, 2019).

Other non-invasive techniques are always first explored to detect the tumours and provide valuable information before planning a treatment and committing to biopsy or surgical removal (Trusheim *et al.*, 2017). Magnetic resonance imaging (MRI) is often used and gives the highest resolution image of brain tissue (under 1 mm, dependant on magnetic field strength), but this lacks biochemical information. Recent developments to *ex vivo* whole-brain MRI imaging have seen this resolution increased below 0.1 mm though this is with excised brains, not in living subjects, and sometimes merged with other imaging modalities (Edlow *et al.*, 2019; Johnson *et al.*, 2023). PET imaging can grant insight into biochemical properties by using a biologically relevant imaging radiopharmaceutical. These radiopharmaceuticals are often analogues of natural compounds, which have an added positron emitting radionuclide that can be detected by PET cameras. For example: by selecting a radiopharmaceutical that behaves similarly to glucose, one can detect regions of cells that are utilizing a disproportionately higher amount of sugar, which is common trait of rapidly dividing cells (Macheda, Rogers and Best, 2005).

2.2 Brain and Glial Cell Morphology: The Progenitors

Understanding the underlying systems and cells related to brain function is imperative to understanding the changes that a cancerous mutation brings and to ultimately be able to take advantage of them. Here, some of the most relevant cell types to this thesis are explored to further understand the differences between their healthy and cancerous counterparts. It is done so that niches that may be exploited for detecting and/or treating these types of cancer subtypes become more evident.

2.2.1 Glial Cells

Glial cells are the non-neuronal cells of the CNS residing in the brain, spinal cord and peripheral nervous system. They do not produce electrical nerve impulses like neurons, but instead provide structure, insulation, nutrients, oxygen and protection to neuron cells (Jäkel and Dimou, 2017). They comprise the blood brain barrier (BBB) which separates the neuronal tissue from the rest of the body and are also the barrier to the of cerebral spinal fluid (CSF). The glial cell types most relevant to common gliomas are further described briefly in the following:

2.2.1.1 Astrocytes

Astrocytes are the most common of glial cell types and provide a complex network of blood, oxygen and nutrient delivery system for the brain and neural cells (Jessen, 2004). They comprise the BBB and because of this, contain all of the tools to effectively absorb and process nutrients from the blood stream in high levels and transport them to other cells. With this function in mind, they are well-suited to support a high level of uncontrolled division with the direct efficient import of raw materials. Additionally, they have been shown to be a key factor in immune system activation by producing chemokine cascades, which are chemicals that signal instructions to immune cells (Pineau *et al.*, 2010). It is possible to also consider a mutation which prevents this immune system activation pathways in conjunction with uncontrolled self-replication promotion that would lead to particularly problematic cancer types.

2.2.1.2 Microglia

In practical terms, microglia are the resident immune system cells of the CNS. Likely because of the BBB, microglia are essential for fulfilling some of the roles that macrophages perform throughout the rest of the body. Microglia are capable of sensing and phagocytosing foreign cells similarly to macrophages (Cronk and Kipnis, 2013), but normally these cells remain semi-dormant in the healthy brain. Microglial activation occurs when chemokine signals, such as those produced by astrocytes, are released after sensing something foreign. In this active state, microglia also release chemokine cascades, which activate additional nearby microglia creating a positive feedback-loop effect. When active they may proliferate rapidly to increase their numbers to find and destroy foreign pathogens. A rapidly dividing glioma in the brain often damages the BBB leading to the “leaking” of blood, foreign particles, and also macrophages into the brain. Discerning histochemically between the resident microglia and infiltrating macrophage immune cells can be difficult as they both share similar characteristics (Pineau *et al.*, 2010).

Activated macrophages, however, will express high levels of folate receptor β (FR-β) while this receptor has not be reported to be directly present on other cell types including microglia (Puig-Kröger, Amaya 2009, O'Shannessy, Daniel J 2015).

2.2.2 Gliomas

Glioma: the cancerous development of tissue originating from glial cells (see: 2.2.1, above). The term is often inaccurately used interchangeably with other glioma subtypes and to make matters worse; glioma nomenclature has changed a few times over the years. This is due to additional discoveries being made, which allowed the differentiation of tumours more accurately. From more specific cellular morphology based on histologically present macro-features to specific genetic markers are nowadays used to accurately subtype these tumours (Louis *et al.*, 2021). One such prevalent naming nomenclature change is the no longer used "glioblastoma multiforme" (GBM) to describe multiple different tumour subtypes. Now, a major subtype division comes with respect to the isocitrate dehydrogenase (IDH) protein and the mutation of the *IDH* gene that codes for it. The most predominant is now designated as "glioblastoma *IDH*-wild type" (GBI), which emphasizes the normal state of the of *IDH*-gene though its level of expression is often highly increased in many cancers (Tan *et al.*, 2012; Zarei *et al.*, 2017) and specifically gliomas (Wahl *et al.*, 2017). This genetic variant is further discussed later in its specific subsection: 2.2.2.1.1.

The current (and consistently updated) classification guide published with the World Health Organization (WHO) (Louis *et al.*, 2021) describes four "grades" or levels of a glioma that correlates with the seriousness of the disease. *i.e.*: The more serious, infiltrative, specifically mutated, and fast growing a tumour, the higher the grade. A comprehensive review of all the types and underlying genetic mutations that contribute to a glioma's detrimental effect to an organism is its own field of pathology and beyond the scope of this work. Generally, nearly all gliomas are a very serious form of cancer with poor patient survival rates if the proliferation rate is high and the tumour is aggressive. Their infiltrative nature into the very delicate brain or other CNS tissue makes them particularly difficult to eradicate and the side effects of surgical removal are inevitable (Claes, Idema and Wesseling, 2007). Below is an overview of some of the main types of gliomas and a brief description some of their general characteristics.

2.2.2.1 Glioblastomas

Glioblastomas are one of the more aggressive brain tumour types with an extremely high probability of recurrence after combined surgical and chemotherapy treatment

(Lu *et al.*, 2018). For an aggressive-characterized subtype, the average survival duration is very short at 12-15 months *if* the patient receives aggressive treatment (Bernard and Christopher, 2014). Such aggressive treatments are very likely to significantly lower the patient's quality of life as they involve the surgical removal of the tumour and some brain tissue followed by chemotherapy and radiation therapy in combination.

The origins of glioblastomas are not so clearly characterized as they are mainly derived from blast cells or "immature precursor cells", which have not yet finished differentiation into other cell subtypes (Fan, Salford and Widegren, 2007). Mutating from this early undefined stage can potentially allow them to increase their plasticity and allow for more mutations to accumulate. The histochemical staining profiles frequently mimic those of astrocytes and astrocytomas (Li *et al.*, 2021), which had them grouped together as recently as the 2016 WHO CNS tumour classification guide. Their increased metabolite import mechanisms, metabolism rate, and often-infiltrative nature provides some physical observations to support this grouping. Part of the aggressiveness of these tumours likely comes from their similar astrocyte components (Kawamura *et al.*, 2018). As astrocytes form the barrier between the brain and the complex vascular system that interconnects the rest of the brain, glioblastomas are positioned to easily take advantage of this network through the same molecular mechanisms. Using the brain's vasculature, they can potentially both grow along this network of rich flowing nutrients or potentially join it to migrate into other parts of the brain or body (Farin *et al.*, 2006).

2.2.2.1.1 Glioblastoma *IDH*-wild type (GBI) and *IDH*-mutants

> *Note: Nomenclature for this tumour subclass has divided in year 2021 from GBM into more specific genetic subdivisions to differentiate between the very common IDH-wild type and other genetic variants which were previously grouped under the same term* (Louis *et al*., 2021). *There still exists genetic variability within subgroups.*

Glioblastoma *IDH*-wild type (GBI), formerly under the larger umbrella classification of "Glioblastoma multiforme" (GBM), comprises nearly 95% of glioblastoma cases in adults (Alzial *et al.*, 2022). It is an aggressive type of glioma and has no structural mutations to the IDH gene, hence the wild-type affix. This does not mean, however, that the gene is not entirely unaffected as many GBI's can have copy number or other gene promoter changes while retaining the normal wild-type integrity of the gene(Calvert *et al.*, 2017). Increases in *IDH* gene copy number has been shown to not always increase gene expression (Georgescu, 2021) and the messenger ribonucleic acid (mRNA) production changes can be influenced by other factors.

The IDH protein has long been known to catalyse the conversion of isocitrate into α-ketoglutarate (LaPorte, Thorsness and Koshland, 1985) and it is particularly relevant to energy production in cancer cells. By increasing its expression and production, you are effectively speeding up the metabolic conversion that it performs and thus create cellular energy more quickly (see later metabolic section on glutamine catabolism and energy production 2.3.4).

Other important characterized genetic variants that fall within the GBI grouping include alterations to the telomerase reverse transcriptase (TERT) promoter region which, when its expression is increased, results in the elongation of tumour cell telomeres and ultimately the prevention of natural cell death. The third main genetic factor currently used to subdivide the GBI group is the status of the epidermal growth factor receptor (EGFR) gene (Louis *et al.*, 2021). EGFR is a commonly over-expressed gene in many cancers and the additionally produced receptors result in many various increased signalling effects (Nicholson, Gee and Harper, 2001). The ultimate result of this is that the cells receive increased growth signals producing additional proteins related to replication and form a particularly aggressive type of cancer (Sigismund, Avanzato and Lanzetti, 2018).

GBI is characterized as WHO grade 4 and at this grade tumours are described as highly infiltrative, proliferating through the brain microvasculature, and spreading rapidly (Louis *et al.*, 2021). The lack of this type of infiltrative nature is generally indicative of a different glioma subtype. The survival rate at this grade level is understandably low and short even when aggressive treatment is applied (Davis, 2016). One of the main issues with highly infiltrative gliomas is that their tumour boundaries are often very poorly defined. Along these infiltrative branches, there is a gradient of tumour cell concentration. To completely eradicate such lesions surgically would require the removal of a lot of additional tissue to completely ensure their removal. Generally, treatment is comprised of surgical removal and then intense chemo and/or radiotherapy to attempt to eradicate the remaining cancerous cells. Unfortunately, it is possible for just a few easily missed cells to escape the immune system-led clean-up and quickly re-establish themselves as a new tumour mass after surgery. This is also partly due to the inherent aggressive nature of GBI. The complete treatment of this disease is not possible with surgery alone due to how the tumours grow. Further developments in biochemical therapies are needed to effectively get rid of the remaining tumour cells, but this is no small task. One exceptionally challenging aspect of treatment is the highly heterogeneous nature of these tumours (Nicholson and Fine, 2021). The cells that comprise these gliomas tend to have different mutations, which in turn gives them potentially different characteristics and biomarkers. These biomarkers, which are usually more homogenous in most other cancers, on the cell surfaces are often what is targeted when developing a more cell-specific targeted therapy.

When considering the recent 2021 nomenclature shift due to more discrete biochemical marker elucidation, this leaves the question of: "*what about the IDH-mutant type?*" It should be noted that some of the glioblastoma *IDH*-mutant subtypes have been now designated into the astrocytoma and oligodendroglioma sub-groups. Although the nomenclature may (and should) be updated further as future discoveries are made, for the sake of flow and clarity they are expanded upon here. For up-to-date classification, it is best to examine the most recent issue of WHO Classification of CNS Tumours (currently: Louis et al., 2021).

Mutations to the IDH protein have been shown in various common cases to render it less effective and, considering its integral role in energy production, this can lower the aggressiveness of the tumour increasing patient survival duration (SongTao *et al.*, 2012). Parsons et al., 2008 reported that 12% of glioblastomas will have a mutation to the *IDH* gene. Quite interestingly, at least in terms of relatively unlikely probability, one known *IDH* mutation point has been shown to be commonly prevalent in 90% of *IDH* mutations (Ohba and Hirose, 2016) and it affects metabolism quite unexpectedly. The mutation occurs on IDH protein codon #132, which changes an arginine amino acid into a histidine (R132H). This change prevents the normal enzymatic conversion of isocitrate into α-ketoglutarate and, instead, allows it to convert α-ketoglutarate into D-2-hydroxyglutarate (Figure 1) (Dang *et al.*, 2009). As will become apparent in later sections, namely glutamine catabolism and energy production 2.3.4, this lowers the overall production of α-ketoglutarate and draws from the remaining α-ketoglutarate pool causing an overall decrease in cellular energy production.

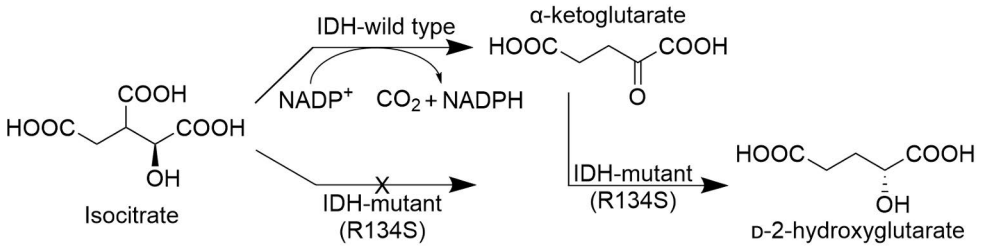

Figure 1. Conversion of isocitrate to α-ketoglutarate via the normal wild type IDH enzyme while this function is inhibited in the mutant R134S IDH enzyme, which instead now converts α-ketoglutarate into D-2-hydroxyglutarate.

Although there are still other major mechanisms to allow for the production of α-ketoglutarate, and the rate at which it converts α-ketoglutarate is 10^7-fold lower than its wild-type producer (Saha *et al.*, 2014), this change has significant effects. The increases in patient survival duration are significantly present (SongTao *et al.*, 2012). This new D-2-hydroxyglutarate compound is quite interesting as it does not

occur normally in the body and is therefore termed oncometabolite. It is not readily taken up by cells in culture (Bunse *et al.*, 2018) but can influence immune cells negatively (Du and Hu, 2021). The altered IDH protein can be a potential cancer-cell-specific-protein to target in cancer treatment, but: *what will that accomplish given its draw away from cancer cell energy pools?*

Although the D-2-hydroxyglutarate oncometabolite does not normally exist in the body, it is still reported to have some unexpected interactions with native proteins. Studies have shown that it interferes with DNA repair mechanisms via the inhibition of the α-ketoglutarate-dependent alkB homolog DNA repair protein (P. Wang *et al.*, 2015). This has two direct effects: Firstly, the cells accumulate more mutations and DNA damage due to the inhibition of the DNA repair mechanism. Secondly, it allows more DNA methylation to occur, which effectively "turns off" or blocks some other genes from being activated. With enough accumulated negative mutations, this can render the cells unviable and lead them to an early cell death. This, combined with the lowering of energy production results in an overall slowing of the tumour's growth rate. The unfortunate catch is that these additional mutations and gene silencing via methylation can increase the heterogeneity of the tumour mass resulting in larger differences between cells (Kusi *et al.*, 2022). This can potentially make it harder to have a specific treatment for this cancer type since there are so many differing cancer cells in the same lesion, but this is no uncommon trope to most gliomas (Perrin *et al.*, 2019). There are many instances of tumour heterogeneity in other cancer types and they are largely attributed to three main factors; stem-cell-like early development of the cells, differences in tumour microenvironment (consider blood vessel adjacent cells versus non-) and epigenetic silencing (methylation) of the genome (Prasetyanti and Medema, 2017), all of which are highly prevalent attributes in gliomas. Many have reported in surgically obtained patient samples a wide variety of glioma cell tumour differences ranging from cell shape to receptor expression creating an exceptionally problematic lesion to target specifically without blowback to other cells.

2.2.2.2 Astrocytomas

Astrocytomas, originating from astrocytes (2.2.1.1), are generally classified from WHO grades 2 to 4, which suggests a wide range of subtypes that are slightly more weighted towards a more aggressive nature. As the vast complex network of astrocytes are responsible for nutrient transfer from the blood and delivery to nearby cells, it comes as no surprise that they can be part of the more aggressive classification group of brain tumours. Mutations causing an over expression in the production of metabolite import proteins have one less barrier to overcome with respect to maximizing the import of energy-producing substrates and building blocks

for replication directly from the blood stream. Due to the year 2021 shift in nomenclature discussed in Glioblastomas 2.2.2.1, they have been separated into their own category divided by the presence of a mutation to the IDH protein-encoding gene. Other mutational and differentiating variants are also found in this group, though due to the relative rarity and numerous nature they are not expanded upon here. These tumours can exist in both anaplastic and diffuse mass variations though recent classification guidelines fit them mostly in the diffuse category (Louis *et al.*, 2021). Since they are integral to the complex vasculature system of the brain and exist in close proximity along its tendril-like nature, it is very common for tumours to present diffuse morphology. This insidious growth pattern via the spread along blood vessels and microvasculature can make them extraordinarily difficult to treat surgically without the removal of excessive tissue. Furthermore, the proximity these tumour cells have to the vasculature system makes it easier for them to migrate into it and either form neoplasms elsewhere in the brain or metastases elsewhere in the body. As with most gliomas, astrocytomas will also often disrupt the BBB via their growth along the vascular network while they practically push other cells outwards even as a small early lesion.

2.2.2.3 Current Treatment Strategies

The current standard patient treatment after surgical excision of the feasibly removable tissue is to follow up with temozolomide chemotherapy (Xu *et al.*, 2020). This compound's mechanism of action is to methylate DNA on guanine residues effectively silencing parts of the DNA from being read (General mechanism and effects further elaborated upon in folate section 2.4.2) which leads to the death of the cell (Wesolowski, Rajdev and Mukherji, 2010). This treatment is far from cell-specific, though does affect rapidly proliferating cells more (proportionally) since they are reading DNA more than other cells in order to make a copy of everything for division. Due to this non-specific approach, which has shown to be (mathematically) significantly effective throughout literature (Dinnes *et al.*, 2002), there are definitely some patient side effects. Additionally, the treatment is not always entirely effective due to glioblastoma resistance development (Lee, 2016) and more research in this area is desperately needed. Although already stated twice before, it is imperative to emphasize that; when these tumours are treated with a proportionally aggressive and standard strategy the average result is still that the patient only lives for 12-15 months post-diagnosis (Bernard and Christopher, 2014).

Some promising emerging therapy strategies to note (which inherently often also apply to the treatment of other cancer types) utilize the body's immune system. T-cell therapy has been used to reprogram immune cells to express receptors that target cancer cells (though it is not trivial to find receptors that target solely the cancer

cells) and inject them into the patient (Bagley *et al.*, 2018). Along this same strategy lies vaccine therapy, which can stimulate the immune system to detect cancer cells better via similar methods (Srivastava *et al.*, 2019). Additionally, viral therapy may also be a viable method in the future whereby a virus is reprogrammed to target immune cells specifically (Martikainen and Essand, 2019). Overall, there is a lot of promising work being done in the detection and treatment of cancer. While there is still much glioma research to be done to progress treatment, the not-so-distant future seems like a more promising halcyon era.

2.3 Glutamine

The natural roles of glutamine in the mammalian body are vast and briefly understanding the variety of roles is essential to understanding how a radiopharmaceutical based on its structure may behave. While any chemical modifications technically make an entirely new molecule, they do not always run the risk of making it impossible for the new molecule to follow similar biological pathways. Proteins that bind or process the molecule can often still function normally if the modifications do not block its ability to interact. To predict whether they do or do not is beyond the scope of this work and is its own field of molecular modelling. Nearly all amino acids exist in an "L" or "D" (*laevus* or *dexter*, left or right) enantiomeric form dependent on the bond direction on carbon 2 (Figure 2). If both L- and D-amino acids were used interchangeably, it would lead immediately to protein misfolding due to the differing bond angles of the enantiomers. The most biologically relevant version to life on earth is generally L-amino acids, though some niche uses for D-ones exist in rarer cases (Fuchs *et al.*, 2005; Kolodkin-Gal *et al.*, 2010).

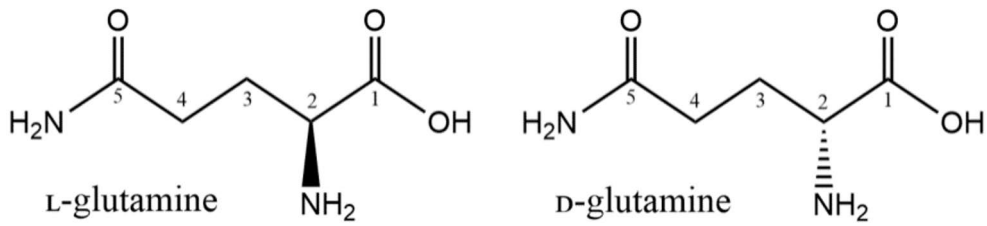

Figure 2. Chemical structure of L- and D-glutamine. Note the direction of the C2 bond where the L version on the left points out of the page and the D vesion points into the page.

The ubiquity of glutamine throughout the body is partly based on its ability to be a nitrogen donor from carbon 5 (Figure 2) or nitrogen acceptor in the missing-C_5-nitrogen glutamate form. This biochemistry allows for the safe transport of ammonia (via glutamine) and export of ammonia waste by-products (via conversion to

glutamate via the formation of urea) in urine. Cellular dumping of ammonia directly into the blood in large amounts (hyperammonaemia) would radically change blood pH levels causing many health problems and thus glutamine is a very common compound in the blood. With this in mind, developing pathways to synthesize, break down, and use this same molecule for additional tasks seems almost evolutionarily guaranteed. Of particular importance is Section 2.3.4 where the catabolism, *i.e.,* the breakdown of glutamine for energy, is discussed. Aggressive cancers can take advantage of this pathway to fuel their need for additional energy and support increased rates of replication.

2.3.1 Cellular Import

The transport into and out of cells is essential for effectively using a molecule in all the different ways a compound such as glutamine can be used. There exist multiple redundant import proteins and ways to move it in and out of cells with more being discovered and added to this growing list. A dedicated review of the many pathways can be found in published literature (Bode, 2001) and they are generally classified into two major categories: Generalists, which import a variety of compounds and amino acids, and Specialists, which are focused (mostly) on glutamine. One such generalist is the solute carrier 1 (SLC1) whose gene family accounts for most of the amino acid transport across cellular membranes. Being a "generalist" importer type, many different amino acids (*or potentially even modified amino acids*) can be transported through this import/export system (Stehantsev *et al.*, 2021).

Perhaps most relevant to this thesis is that the BBB allows for the free transport of glutamine through multiple amino acid transporters (Hawkins *et al.*, 2006). This is essential for the removal of excess waste. This removal ensures that these potentially harmful compounds to not accumulate in the brain playing an indirect, but key, role in neuronal relaxation after synapse activation.

2.3.2 Protein Synthesis

> *[Proteins]: …The cause and solution to all of life's [biochemical] problems - H.J.S.*

The generation of linear amino acid chains leading to the ultimate folding of a large three-dimensional functional protein is the essence of life, as we know it. The majority of biological problems can be summarized into one of the following simplifications:

1) There is a protein that *does not perform* a function that is *intended*.

2) There is a protein that *performs* a function that is *not intended*.

In its primary structure, the amino acid chain (shown as a two-unit dipeptide in Figure 3) allows for a long string of proteins of differing amino acids to be coded. Glutamine, being a common amino acid, is incorporated into amino acid chains to ultimately form larger complex three-dimensional proteins. Life is practically restricted to using the L-version of amino acids as using the D- or L- forms interchangeably would cause completely different bond angles causing the resulting three-dimensional structure to be malformed. The bond angles formed by D-amino acids have been shown to not favour the formation of common higher structures such as alpha helices and beta sheets (Mitchell and Smith, 2003).

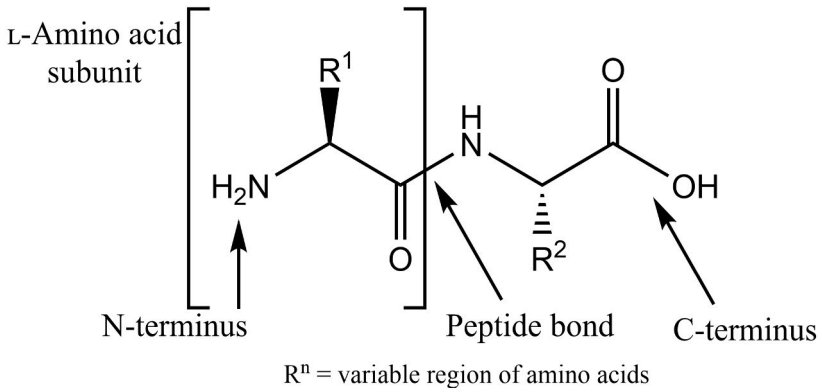

Figure 3. Dipeptide L-amino acid chain structure and peptide bond been subunits.

2.3.3 Signalling

There are many cases where glutamine can be used as a signalling molecule, though due to its ubiquity in the mammalian body, it generally affects systems in a gradient manner. Excess cellular amino acids are often a requirement before triggering cellular replication (Durán *et al.*, 2012) since the process would fail if there were not enough building material to make duplicates of essential compounds to divide between two new cells. It should be noted that signalling involving the rarer D-glutamine isomer has been reported, albeit rarely, in both lower organisms (*e.g.:* biofilms (Kolodkin-Gal *et al.*, 2010) and even in higher organisms in a human neurosignalling pathway (Fuchs *et al.*, 2005).

2.3.4 Catabolism and Energy Production

An exceptionally important thing to note about glutamine is its potential use as a substrate for cellular energy production. Of course, a rapidly dividing mass of cells will require fuel to sustain processes associated with replication and rapidly dividing cancer cells are no exception. While most people are at least vaguely familiar with how fat and glucose sugar are used in the body for aerobic and anaerobic energy production (respectively), many do not realize that some amino acids such as glutamine can be used as an energy source. The metabolic pathways for any amino acid are generally diverse and for one as ubiquitous as glutamine there are perhaps more than almost any other amino acid. A detailed map of many of the catabolic and anabolic pathways known thus far has been elegantly described in literature (Yelamanchi *et al.*, 2016) though the most relevant one to energy production are described.

The first conversion step in the production of energy from glutamine requires the reversible removal of the terminal amine group in the conversion to glutamic acid (Figure 4).

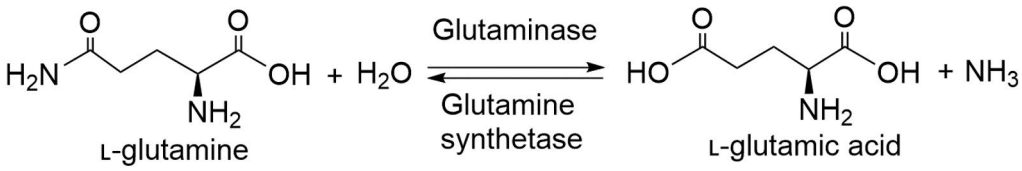

Figure 4. Reversible enzymatic conversion of L-glutamine to L-glutamic acid

The reverse of this initial step is also a major way that the body can get rid of waste ammonia, transport it safely through the blood stream to the liver, and ultimately produce and excrete urea (note the production of ammonia in the forward direction). In cases where glutamine consumption for energy is extremely high, it has been shown that blood circulating blood glutamine levels can be detectibly decreased (Chen and Russo, 2012).

The next step Is to process the glutamic acid into α-ketoglutarate, which can be used in the tricarboxylic acid (TCA) (aka: Krebs) cycle. Interestingly, there exist two separate main forms of the enzymes to process this reaction, which are specialized to their microenvironment. Glutamate oxaloacetate transaminases (GOT1 and GOT2) are homodimers that exist in the cytoplasm and mitochondria (respectively). These enzymes can complete this next deamination without releasing free ammonia by simultaneously aminating oxaloacetate into L-aspartate (Figure 5), which is primarily used as an amino acid for protein synthesis.

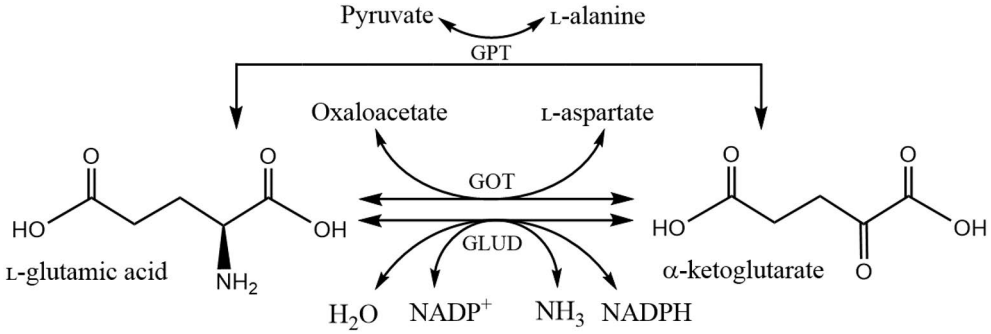

Figure 5. Conversion of L-glutamic acid to α-ketoglutarate

Another important enzyme family called Glutamate Dehydrogenase (GLUD) can also catalyse this important body reaction but release ammonia in the forward conversion into α-ketoglutarate. As a side reaction, it also catalyses the conversion of $NADP^+$ into NADPH, which is a biochemical energy substrate used for many other reactions. The GLUD enzymes exist in two major forms (GLUD1 and GLUD2) residing in the mitochondria and endoplasmic reticulum (Mastorodemos *et al.*, 2009). GLUD1 is practically solely found in the liver (in large amounts) and acts as both a significant contributor to energy production and a reducer of blood ammonia levels when catalysing the conversion back to glutamate (Hu *et al.*, 2014). GLUD1 has been shown to be vital in regulating blood ammonia homeostasis (Bera *et al.*, 2016).

GLUD2 is found in high concentration in neuronal cells and also acts as a glutamate homeostasis regulator, though with differing regulatory mechanisms. Many neurons activate via the expulsion of glutamate to signal to an adjacent neuron and then during the relaxing phase must uptake lost glutamine to fire again. During periods of extensive activation, it is possible for an attempted signal to not quite pass the threshold for signalling due to depleted glutamate levels. GLUD2 is thought to act as an extra regulator to prevent glutamate shortfalls and regulate glutamate levels in environments that require a very active and precise concentration gradient (Shashidharan and Plaitakis, 2014). Another notable cell type with high GLUD enzyme levels are the Sertoli cells in the male testis. These cells are responsible for aiding the production of sperm cells and are thus constantly consuming energy to support the proliferative process as well as synthesizing proteins (Spanaki *et al.*, 2010).

The third main known enzyme family in this conversion into α-ketoglutarate is glutamate pyruvate transaminase (GPT). GPT1 and 2 exist structurally as homodimers in the cell cytoplasm and mitochondrial matrix (respectively). They function by catalysing the transfer of the amine group of glutamine, forming

glutamate, to pyruvate which converts the pyruvate into L-alanine (Chen and Giblett, 1971). There are reports in literature that correlate high GPT2 expression with aggressive cancer subtypes (Cao *et al.*, 2017), which seems reasonable due to its relation to metabolic activity. The final unanswered question remains:

how is cellular energy made from glutamine?

After converting it into glutamate and then into α-ketoglutarate, essentially removing all the amine groups, it is now a substrate for the Krebs cycle (aka: the TCA cycle, or the citric acid cycle). In this biochemical cycle, most of life as we know it can break down one sugar molecule (glycolysis) into three pyruvate molecules (via multiple intermediary steps), which can each be input into the Krebs cycle pictured in Figure 6. Though not shown for the sake of simplicity, this cycle produces a large net gain of cellular chemical energy (catalysing the conversion of energetic compounds into higher-energy compounds). This production occurs through many of the intermediary steps as a by-product of their conversion through the cycle. It is important to note that glutamine as a fuel will not produce nearly as much biochemical energy as glucose. This is both because glucose is broken down into three pyruvate molecules (effectively running the Krebs cycle thrice), whereas glutamine input in the form of α-ketoglutarate pushes the cycle forward once.

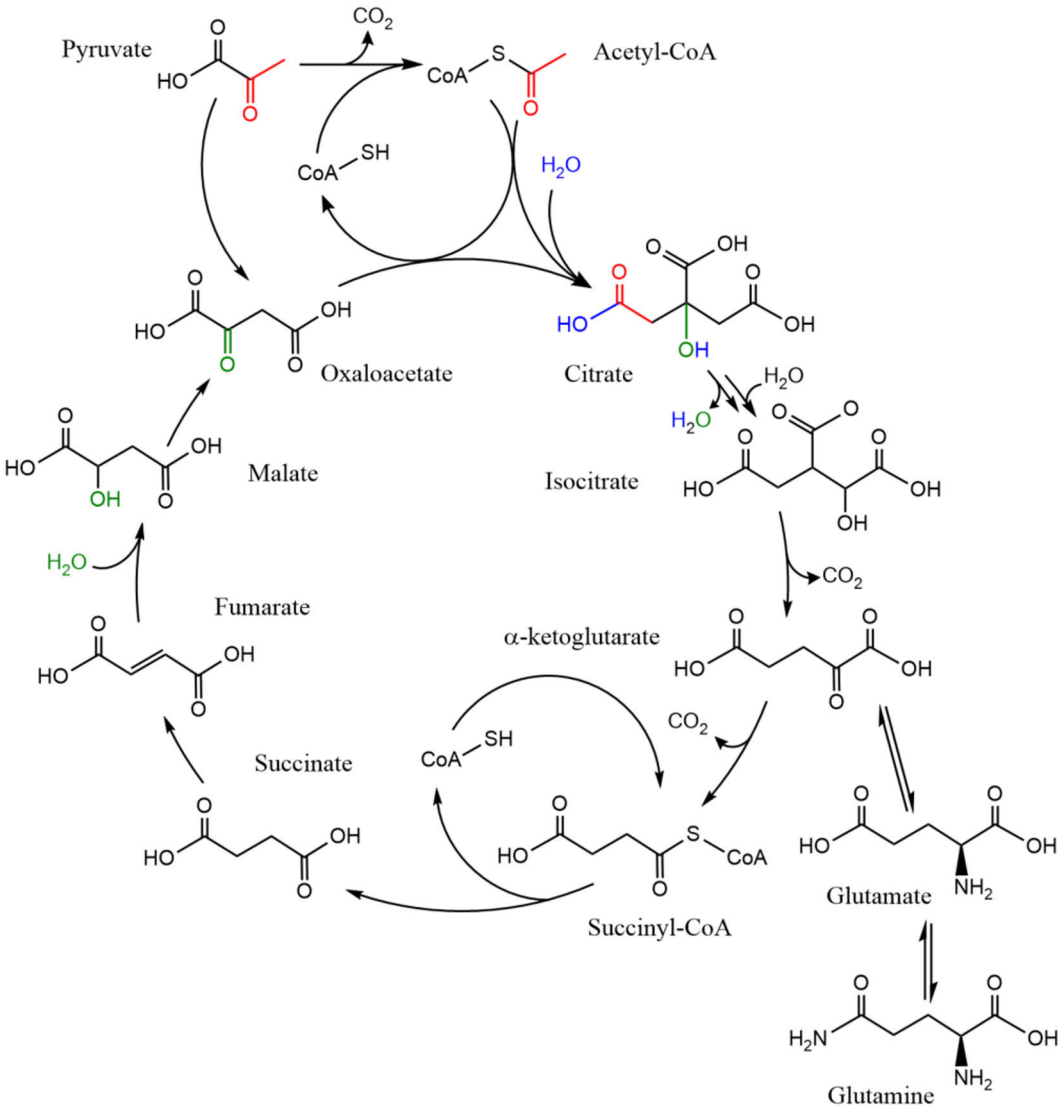

Figure 6. Simplified overview of Krebs cycle.

2.3.5 Anabolism and *De Novo* Synthesis

For most mammals, including ourselves as humans, we classify the various amino acids as “essential” or “non-essential”. This is to differentiate between the ones that must be ingested via dietary means (essential) or those that can be created within the body from other substrates via *de novo* synthesis (non-essential). The ability to synthesis amino acids outright or biochemically change various amino acids into other ones is a valuable tool for biology. When dietary inputs do not give the correct

balance of amino acids, being able to synthesize any shortfall is the difference between a functioning organism versus one that may have health or energy issues. Glutamine production occurs via numerous known pathways with some outlined already previously in Figure 4 and Figure 5. A very thorough description of many of the known pathways is published in existing literature (Yelamanchi *et al.*, 2016).

2.3.6 Purine and Pyridine Production

The building blocks of DNA owe part of their structure to glutamine. As many know, the DNA "code" is comprised of Adenine (A), Thymine (T), Guanine (G), and Cytosine (C) (Purines and Pyridines). These A's, T's, G's, and C's make up the instructions for cells to basically produce everything that makes them what they are for all life on earth. Practically all cells in most organisms will have a copy of their DNA to be transcribed into mRNA and ultimately used to synthesize proteins. When a cell divides, it will make a copy of the DNA to be split between the two dividing daughter cells. This involves the production of a lot of new DNA, which, in turn requires the production of a lot of A's, T's, G's, and C's. part of this production requires the addition of an amine group, which can conveniently be donated from glutamine. The following Figure 7 shows the purine and pyridine chemical structures of as well as highlights (in red) the nitrogen atom in their structures which owes its origin from a glutamine molecule (Boza *et al.*, 2000). Additionally, though not discussed her in substantial matter is that, the nitrogen atom on the uracil molecule (ribonucleic acid RNA), is also added from glutamine.

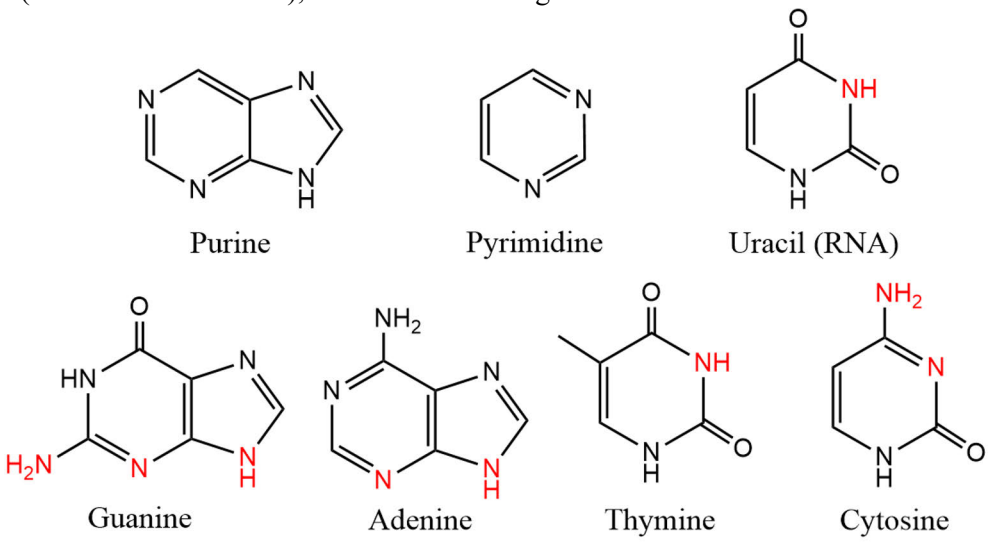

Figure 7. Purine and pyridine structures along with amine groups donated from glutamine in their production highlighted in red.

2.3.7 Summary

Overall, a very high flux of glutamine (intertwined with glutamate) in areas of the body which are processing large amounts of biochemical energy can be observed. Whether in the form of using energy to signal, proliferate, build proteins, or process waste ammonia, glutamine usage is universal to all mammalian life (Meister, 1974). Many of the hallmarks of glutamine consumption become amplified as a cell becomes more active and proliferative (Matés *et al.*, 2002). These functions, especially cellular division, require both large amounts of biochemical energy as well as glutamine specifically for protein production. In the case where a cell may be replicating uncontrollably, glutamine and its related enzymes or pathways are clearly a viable target to exploit for the detection and treatment of many overly proliferative diseases.

2.4 Folic Acid

The term folate is generally used to refer to several similar compounds in the vitamin B family, though for the sake of simplicity this manuscript will focus on folic acid specifically due to its significance in the research presented. Many folate compounds have a similar dietary necessity and function with sometimes differing specific (or sometimes generally acting) enzymes to process it. Folic acid (Figure 8), also referred to as vitamin B9, has been known for a long time to be an essential part of human nutritional requirements (Davis and Nicol, 1988). It is particularly important for pregnant women due to the quickly dividing cells that are constructing the growing fetus and a deficiency is linked to a plethora of new-born disease (Crider *et al.*, 2022). The wide range of issues stemming from a lack of dietary folate intake derive from the human body's inability to synthesize the vitamin. Folate holds a variety of functions in the human body and biochemically speaking it is an extremely

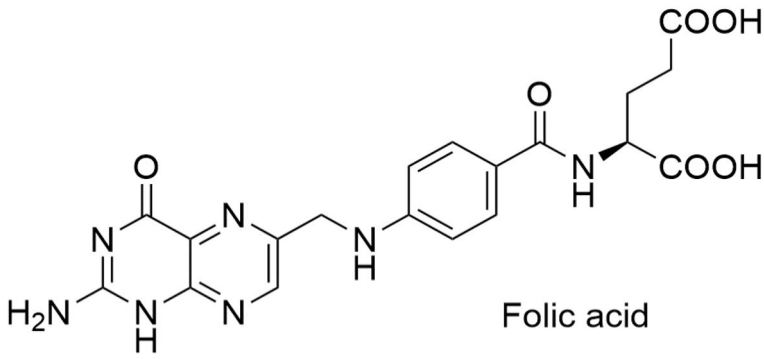

Figure 8. Folic acid chemical structure.

important cofactor in the synthesis of DNA (Scaglione and Panzavolta, 2014) and the single-carbon-addition (methylation) donor to DNA (Liu, Liu and Zhang, 2020). Clearly, the synthesis of DNA is extremely important for a rapid dividing fetus while it creates new cells and structures, but also for fully formed humans as there are many cell types, which are still continually replenished (*e.g.* hair, skin, stomach lining, blood cells, wound repair and much more). The methylation aspect, which happens after further biochemical conversions, is also vitally important for cell development. Methylation is one of the primary methods which cells use to block various genes and "turn off" specific parts of genetic code so that a cell can specialize and become a specific cell type such as a neuron or muscle cell while still retaining a full copy of an organism's DNA.

These important uses for dietary folate intake have many overlapping similarities to cancer cells, which are also dividing rapidly. Since cellular division requires a lot of DNA synthesis, we expect to see an upregulation of mechanisms to intake and process folate for aggressively growing cancer types. For this reason, folate receptors have a long and varied history of being used as a target for an exceptionally high number of cancer types (Matherly, Hou and Deng, 2007; Scaranti *et al.*, 2020). Even though there is a lot of research already done on imaging (Boss and Ametamey, 2020; Kim *et al.*, 2020) and treatment (Shen *et al.*, 2018; McCord *et al.*, 2021), there is still more to learn and most importantly: exploit to benefit human health.

2.4.1 Cellular Import

The first step in understanding a drug or compound's ability to affect a specific cell or organ is often to understand *how* the molecule enters a cell (Tan, Tan and Chung, 2008). For important biological substrates, and folate is no exception, there often exist multiple transport proteins that can act on a single molecule. Evolving multiple redundant pathways for something essential to the organism's continued health seems like a logical reason for this, though often different proteins are required so that they can be controlled/amplified via differing specific pathways. For example, stimulating immune cell replication would benefit from having a different activation pathway compared to hair follicle cells so that additional energy during an infection isn't wasted to promote hair growth.

Practically all cells require folate at some point in their development and thus nearly all have the widely distributed reduced folate carrier (RFC) types of proteins (Bailey and Gregory, 1999; Wagner, 2001). These transmembrane proteins allow for folate to enter a cell via the exchange of a sodium ion (Na^+) out and function in either direction allowing folate to flow along a chemical gradient. The first to be characterized in detail, and perhaps most widely studied RFC since, is the solute carrier family 19, member 1 (S19A1) protein (Chan *et al.*, 1995). The widespread

nature of this protein within mammals demonstrates the importance of how folate interacts with cells. Interestingly, research has shown a link between subtle mutations in the gene that codes for this protein and the subject's lack of response to chemotherapy treatments that target it (Hou and Matherly, 2014).

Two particularly important and relevant folate receptors in relation to cancer are the folate receptor alpha (FR-α) and folate receptor beta (FR-β). These specific folate receptors have a much higher binding affinity for folate than the solute exchange-based RFC transporters (Schaber *et al.*, 2021) allowing them to very quickly and efficiently take up small amounts of folate into the cells. These receptors intake folate by first binding to the molecule and then cause the cell membrane to fold in on itself and separate from the membrane inwards in a process known as receptor-mediated endocytosis (Sabharanjak, 2004). If one considers the process and how it may look in three-dimensions, it is possible to imagine that a modification to the end of the folate molecule, which does not interfere with the binding to the FR (yet is small enough to still be encapsulated by the endocytic process) it may be possible to traffic along some additional chemical addition with it.

FR-α has been shown to be considerably upregulated and expressed in many cancer cell types and highly elevated levels are linked to poor patient outcomes (Ginter *et al.*, 2017). Some type of folate import mechanism upregulation seems reasonable, given what is known about the use of folate and how active cellular proliferation would drive it's requirement. As of such, FR-α has been given extensive attention as both a target for imaging (Ke, 2004; Low and Kularatne, 2009; van Dam *et al.*, 2011) and in treating cancer (Assaraf, Leamon and Reddy, 2014; Z. Wang *et al.*, 2015; Cheung *et al.*, 2016).

FR-β is an interesting variant to the many other folate receptors as it is virtually only expressed on activated macrophages (Xia *et al.*, 2009). High folate requirements for these cells would be expected due to their ability to proliferate locally in response to a foreign pathogen (Jenkins, Stephen J. 2011). It is logical to imagine that macrophages would have their own systems for dealing with increased metabolic substrate requirements for replication as an additional checkpoint to ensure that they can be activated without influencing the metabolic activity of nearby cells.

Folate receptors and transport proteins have been a target for the cancer chemotherapy drugs in clinical practice since the 1950's (Burchenal *et al.*, 1954). One such compound, methotrexate (Figure 9) , functions by antagonizing the ability of the transport proteins to function (Matherly, Hou and Deng, 2007). Because of this mode of action, this class of drugs has also been used to treat other diseases intertwined with proliferation such as inflammatory-derived issues (Chan and Cronstein, 2010).

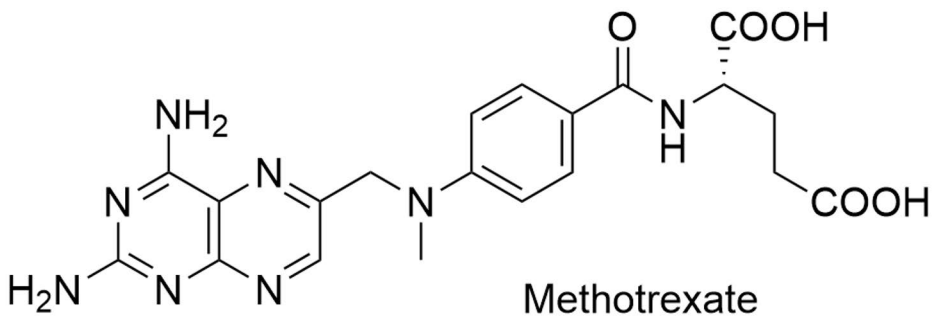

Figure 9. Methotrexate chemical structure. *Note the structural similarities to folic acid in the preceding figure.

2.4.2 Cellular Use in DNA Synthesis and Methylation

The most relevant driver for cellular folate uptake in the context of cancer cells is its usage in DNA synthesis. As with nearly all biochemical pathways in cells, the usage of a compound is seldom a straightforward single reaction. Folate is no exception and there are many known steps and enzymes that deal with its usage for a single molecular task in a specific organelle, let alone the multiple biochemical tasks in different organelles utilizing different forms of folate (Rozen, 2010). The most essential roles and biochemical reactions revolve around one-carbon transfer chemistry. In practice, these chemical reactions are not so simple as a single carbon addition to or removal from a molecule doesn't leave space for additional atoms that would lower the energy required to make the reaction happen more easily. Practically speaking, and something that chemists learn in the lab when working with highly reactive single-carbon addition facilitating compounds like methyl iodide, it is a difficult reaction to complete- especially in a non-cell-exploding manner in a delicate cellular environment. Part of the nucleotides that make up DNA (discussed previously in 2.3.6) also owe some of their structure to folate. The carbon atoms drawn in red (Figure 10) show which ones owe their origins to a folate molecule methylation reaction (Boza *et al.*, 2000). Again, for a cell to divide it needs to synthesize an additional copy of DNA to split the two copies between the daughter cells and to synthesize this requires a lot of nucleotides.

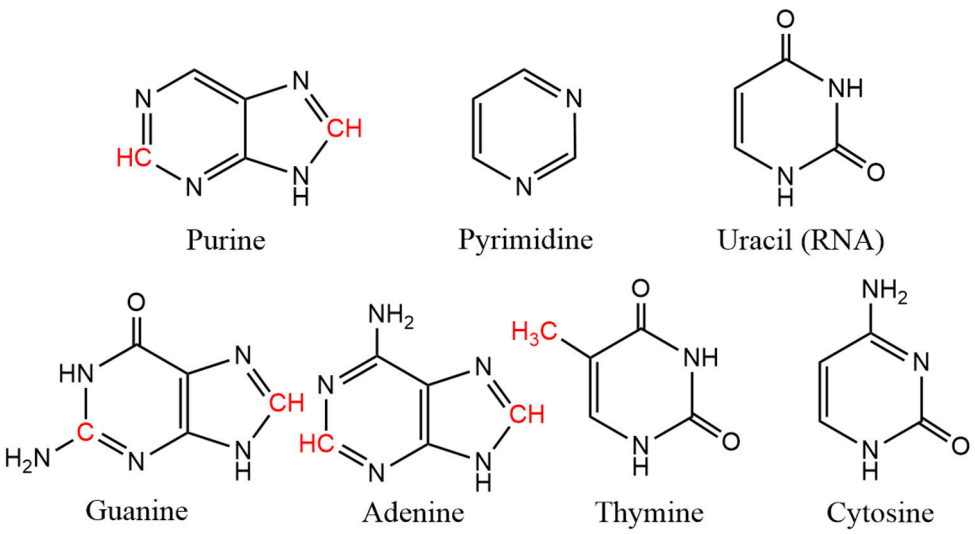

Figure 10. DNA nucleotides with carbons owing their origins to a folate-based methylation reaction highlighted in red.

The reaction occurs through many reversible steps (whose detailed description and chemistry could be yet another entire thesis) starting with the conversion of various folates into 10-formyltetrahydrofolate. For example, one pathway converts folates into 5,10-methylenetetetrahydrofolate (not shown) upon which it can be converted into 5,10-methenyltetetrahydrofolate (via a substrate-specific protein). This can then be converted into 10-formyltetrahydrofolate (Figure 11) via the compound-specific enzyme methenyltetrahydrofolate cyclohydrolase (MTHFD). In this form, the compound is ready to perform a one-carbon methylation (transient methylating carbon shown in blue, Figure 11) (Christensen and MacKenzie, 2008).

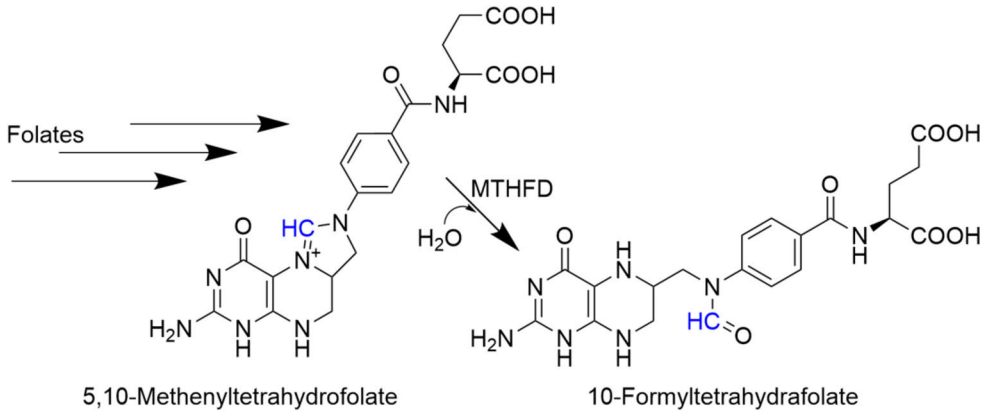

Figure 11. Folate conversion basics for future methylation utilizing the carbon highlighted in blue.

Another important task of the methylation abilities of 10-formyltetrahydrofolate is the methyl addition to various amino acids to convert them into different amino acids. Namely, glycine production and the conversion of serine into methionine. This ensures that amino acid homeostasis can be balanced and that there is little risk of "running out" of some specific amino acid which would halt all protein transcription and production.

The third main essential function of folate-based methylation is the methylation of histones (Garcia *et al.*, 2016; Serefidou, Venkatasubramani and Imhof, 2019). This is one of the processes that, to put simply, "turns off or silences" genes by physically blocking their transcription. It is an essential process to allow cells to differentiate and specialize into specific cell types (Ebert *et al.*, 2006). When a cell replicates, not only must it make a second copy of its DNA, but it (in most cases) needs to copy all the methylations on the histones to ensure that the daughter cells remain the same (Hashimoto, Vertino and Cheng, 2010). The amount of methylation is highly variable and dependant on which genes a cell will need to be that specific type of cell, so it is very difficult to quantify. It is a relatively high amount when considering the amount of DNA stored in a cell, further demonstrating the high levels of folate needed for division.

2.5 Positron Emission Tomography (PET)

From radioactivity to multidimensional image output

The basic principle of positron emission tomography (PET) imaging is to use a ring-arrangement of photomultipliers to capture two photons originating from a single decay event that travel in (nearly) equally opposite directions. This photon pair can then be used to trace back the origin location where they formed and ultimately create a 3D (and sometimes 4D with respect to time) map of colocalized detections within a given volume. These detections are ultimately used to make a PET image (Basu *et al.*, 2011).

Radionuclide production

PET imaging is only possible with the production of a sample of unstable radionuclides which will release a positron particle upon their decay. One of the most common positron-emitting radionuclides is fluorine-18 ($[^{18}F]F^-$), which has one less neutron than the more common and stable fluorine-19. Although the formation of these unstable isotopes does occur in nature, the relevant ones for modern PET imaging are made reliably by a cyclotron or other particle accelerator. By

accelerating protons and colliding them with a target filled with oxygen-18-enriched water the following reaction takes place:

$$^{18}O + p \rightarrow {}^{18}F + n$$

This describes how an oxygen molecule with an atomic mass of 18 has a proton collide with it, stick to it and bump out a neutron changing the identity of the atom (Clark and Silvester, 1966). This new atomic configuration, however, is unstable due to an imbalanced number of protons and neutrons and will spontaneously decay. The average decay rate is measured in physical half-life where half of a given sample of atoms will have decayed by that time point.

Radiopharmaceutical synthesis

The radionuclide is transferred to a lead-shielded fume hood where mostly remote-controlled valves allow for the manipulation of the radioactive sample via a properly designed apparatus (*e.g.*: Figure 12) to shield the chemist from the radiation that is constantly being released. Many different radiosynthesis devices are commercially

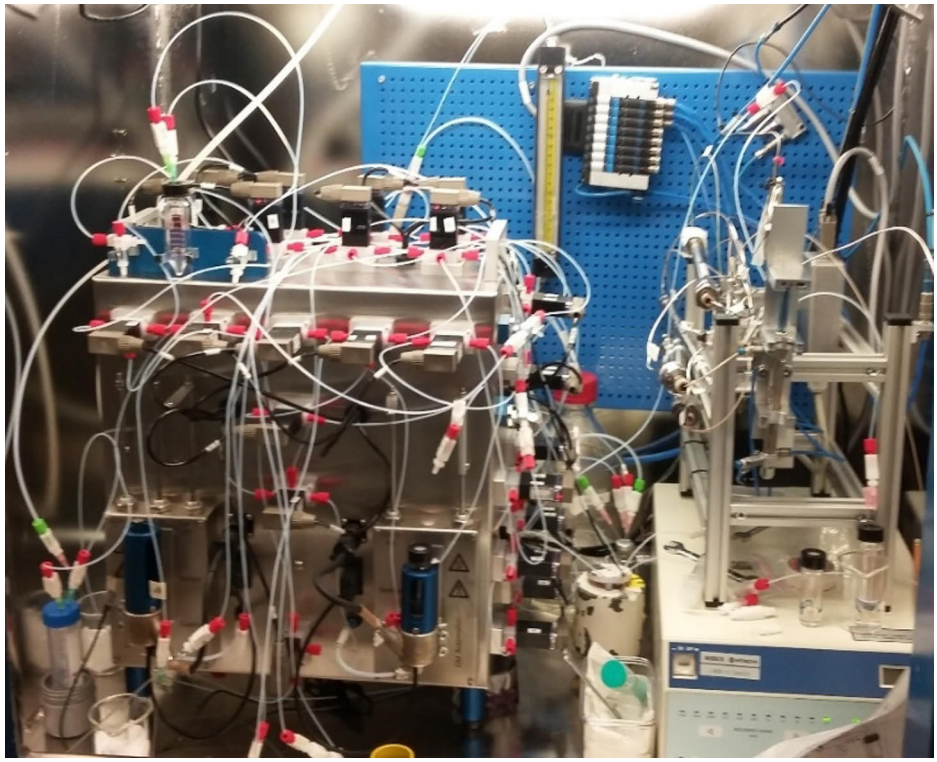

Figure 12. Multi-use radiochemistry synthesis device with a plethora of automated valves, purification systems, heating apparatuses, and collection vials.

available with preassembled cassette style being often preferred for the most routinely produced radiopharmaceuticals to reduce the chance of user error (Vyas *et al.*, 2022). For more experimental radiopharmaceutical syntheses, a general-purpose device is usually employed while for more niche or experimental syntheses, custom hardware and software additions are not uncommon (Pascali *et al.*, 2014; Fu *et al.*, 2023).

The devices are generally setup so that as little as possible is done in a hands-on manner and instead via the manipulation of remote controlled valves (Radchenko, Baimukhanova and Filosofov, 2021). Solvents, buffers, HPLC columns, filters, reaction vessels, and more are pre-loaded into their appropriate spots. Nitrogen gas is often used to push liquids into new vessels for reactions or loading onto separation cartridges. Pneumatic systems are often employed to manipulate syringes to suck up or inject a solution into a new vessel. The same general rules and techniques of chemistry apply, though with an added radiation safety factor that must be accounted for to expose the chemist to as low of an amount of radiation as reasonably achievable. After the desired product is synthesized or radiolabelled with the newly created radionuclide, a smaller sample can be tested for quality control while the bulk of the product is transported to its intended facility or recipient(s) as the approval of quality can then arrive electronically moments before use ensuring that no unnecessary additional decay of the product takes place.

Decay

As time goes on and the unstable atoms decay, they do so in a process that releases energy in the form of radiation. The type of radiation and energy depends on many factors stemming from the identity of the parent nuclide and whether the nuclei imbalance skews towards excess protons or excess neutrons. In the case of fluorine-18, the physical half-life is 109.8 minutes and the decay releases back out a proton in the form of a charged beta particle (β^+, also denoted as "positron"), effectively changing the atom back into oxygen-18 as shown below:

$$^{18}F \rightarrow {}^{18}O + \beta^+$$

The physics behind signal collection and conversion into an image

After this happens, the β^+ particle, also known as an anti-electron, travels some distance (based on its energy and nearby particles to interact with) in a random direction losing speed as it interacts with nearby matter. At some point it interacts closely and slowly enough with an electron and the two particles annihilate each other. At this moment, the two particles transform into energy following Einstein's $E=mc^2$ in the form of two photons. Due to the conservation of momentum, these two

photons begin to travel in nearly equal and opposite directions (plus some momentum energy from the β^+ particle travel) with a discrete energy level of 511 kiloelectron-volt (keV). This discrete energy level and equal and opposite direction of travel is quite useful practically. With a ring-arranged detector system of photomultipliers and some extremely clever computations it is possible to detect two photons at nearly the same time and trace back their probable point of origin. Filter out photons whose energy values fall too far below 511 keV suggesting some scattering, adjust the for the slightly lower-than-511 keV that may have interacted with bone tissue that you already have a 3D map of from an x-ray scan, and its complete! The technique is vastly more complex than the simplification outlined here as there can be millions of signals per second and the reconstruction methods use elegant mathematics that reinforce the expectation of signal from a specific region. Nevertheless, the method can be used to produce a map of signals down to 4 mm resolution (Lodge *et al.*, 2018) (even more resolution for smaller preclinical cameras at 1mm as the ring diameter can be smaller (Herschman, 2003)) and create a heat-map of where radioactivity is located within a subject. While this may not seem like such cutting-edge spatial resolution compared to other technologies such as x-ray computed tomography (CT) (*e.g.* Figure 13) and MRI, these imaging modalities can be (and are very often) paired and fused (overlapped) with a PET image for accurate physiological reference. With PET imaging there is the significant bonus of being able to divulge biochemical information via selecting a biochemically relevant radiolabelled compound. These are most often administered intravenously as a bolus, though other methods (such as infusion or inhalation) exist. PET imaging can also take place over a specific time window post-injection to create a video of where the radioactivity "moves" and accumulates in a subject.

Modern PET imaging utilizes a multitude of different positron emitting radionuclides taking advantage of the radiochemistry of each and their mimicked properties with their "normal" non-radioactive stable isotope counterparts (Hamoudeh *et al.*, 2008). They all have different physical half-lives and energy

Figure 13. Modern human PET/CT camera system in the Turku PET Center

characteristics (Emery *et al.*, 1972), which can in influence their practical use and resulting PET image quality (Teuho et al., 2020). Over the years there are shifts to and from new and old β^+-producing radionuclides depending on what new discoveries are being made (Inubushi *et al.*, 2018). Although the most commonly used is $[^{18}F]F^-$, other common ones include carbon-11, and oxygen-15 due to their intertwined nature with life's biochemistry. This can make measuring interactions with naturally occurring molecules a more straightforward and replicative process. The relatively short physical half-lives of these radionuclide (compared with fluorine-18) of 2.04 and 20.4 minutes for oxygen-15 and carbon-11 respectively, however, make them a bit less practical to work with (Conti and Eriksson, 2016). Other common PET imaging radionuclides include metals and transition metals such as gallium-68, copper-64, and zirconium-89 (half lives: 67.1 min, 12.7 hr, and 3.3 days respectively). These are often used due to metals having an expanded electron shell with allows for more possibilities of non-ionic bonding through chelation-based chemistry. This can allow for a very complex compound to be prepared in advance and then the possibility for adding the radionuclide in a faster and simple one-step heating reaction (Liu, Liu and Hnatowich, 2010).

2.6 Radiopharmaceuticals for PET Imaging Gliomas

When designing a radiopharmaceutical for PET imaging cancer or gliomas the hypothetical "ideal goal" would be to have 100% of it go into the target tumour tissue. Practically, this is an absolute fantasy since the reality of a living biological system is considerably complex in the way it transports and breaks down compounds. The reality of a "good" PET tumour-imaging radiopharmaceutical lies within its ability to contrast and quantify regional differences in ongoing biochemical processes allowing for a biological cause to the detected discrepancies to be elucidated (Kunos *et al.*, 2021). Although different "modes of action" with respect to radiopharmaceutical type can dictate which measurable parameters are more significant than others, some discrete quantifiable properties generally include:

- Specificity: how well does it bind to a single specific protein, receptor, or target.
- Selectivity: How well does it uniquely target its intended target tissue or receptor in comparison with other similar targets.
- Binding affinity: how quickly and strongly will the radiopharmaceutical bind to the target and is there another rate at which it goes inside the cell.
- Dissociation constant: how quickly will it become unbound to the target (still potentially able to rebind).

- Clearance from the target: how quickly will it dissociate and leave the target region.
- Erythrocyte uptake: How fast and in what amount does it go into red blood cells and is thus unavailable to bind to the target.
- Clearance from the blood stream: How fast it "disappears" from blood circulation.
- Plasma protein binding: How fast and in what amount will it get stuck to proteins circulating in the blood plasma and is thus unable to bind to the target tissue.
- Metabolic break down: How fast it gets broken down into other compounds.

It is important to acknowledge that there are large inherent differences between types of radiopharmaceuticals and their type of relationship with an *in vivo* biological system (see 2.6.1, 2.6.2, and 2.6.3). These differences can alter the practical ability to quantify a radiopharmaceutical's effectiveness using all the previously listed parameters. For example, an energetic metabolite (*e.g.*: 2.6.1) that is taken up irreversibly and not metabolized will behave differently from one that is reversibly taken up by a cell, metabolized and excreted. These two examples would also behave inherently differently from a ligand-binding radiopharmaceutical (*e.g.*: 2.6.3) that may bind to the surface of a cell and can spontaneously unbind (or alternatively remain "stuck"). The difference between how much a radiopharmaceutical accumulates in the target tissue vs. adjacent (or non-adjacent) healthy tissue can also be a simple quantifiable value of how well they can be detected from a PET image (Vermeulen *et al.*, 2019). Having a region of healthy tissue in the same subject, *e.g.*: healthy kidney vs. damaged kidney, will simplify the comparison further. When considering clinical translation of a radiopharmaceutical, additional parameters can be examined to determine practical suitable for use in humans. Although not expanded upon in this preclinically-focused thesis, examining toxicity, immunogenicity, body dosimetry and cost effectiveness can be often considered (Allott and Aboagye, 2020).

Another important principle for imaging radiopharmaceuticals is to generally have the imaging dose many orders of magnitude below a level that would influence the biological system (Wadsak and Mitterhauser, 2010). This aspect has often caused imaging radiopharmaceuticals to be given the term "tracer" following Georg Hevesy's proposed properties for detecting trace amounts of radioactive iodine (von Hevesy, 1913). The PET imaging dose is often in the picomolar or even lower amount as imaging systems are quite sensitive in their ability to detect radiation (Missailidis and Perkins, 2007). In this way, an imaging radiopharmaceutical can act solely as a reporting probe that follows the natural flow or gradient of whichever processes that use it or its naturally occurring analogue. For example, an injected amount of 300 MBq of [^{18}F]FDG (~8.6×10^{-10} g) into a human will not overload any glucose transport or metabolic processes as it is many orders of magnitude lower than what would have an impact on the system.

Unfortunately, PET imaging the brain has an additional hurtle to overcome (or *barrier* to pass) due to the BBB that inhibits the free passage of many compounds from the blood into the brain (Pike, 2009). Due to this, additional properties must be considered when selecting an existing or creating a new radiopharmaceutical for brain imaging. The main properties that affect BBB passing are lipophilicity (related to the ability to go into fatty acid membranes) (Waterhouse, 2003), whether the compound can cross through existing transport proteins (Sasongko et al., 2005), and whether the compound can bind to receptors on the BBB allowing it to be bound or later taken in via other means. Coincidentally, the first widely used radiopharmaceutical, glucose analogue [^{18}F]FDG, has impeccable BBB transport ability since the brain uses glucose as its primary fuel and the [^{18}F]FDG structure mimics this (Hasselbalch *et al.*, 1996). Other radiopharmaceuticals, however, do not always have this high accumulation in the brain due to either their inability to pass the BBB or a lack factors driving the uptake into the brain.

An overview of some of the more common radiopharmaceuticals currently used for PET imaging gliomas and their method of accumulating in tumour tissue is presented in the following sections.

2.6.1 Energy Metabolites: [^{18}F]FDG

There are a few reasons why [^{18}F]FDG has remained the "king" of radiopharmaceuticals and the primary reason is that our bodies function primarily on glucose sugar as an energy source. The structure of [^{18}F]FDG is nearly the same as the structure of native glucose but with one important change: There is an [^{18}F] radionuclide (drawn in red, Figure 14) replacing the hydroxyl group (hence now: deoxy) at carbon position 2.

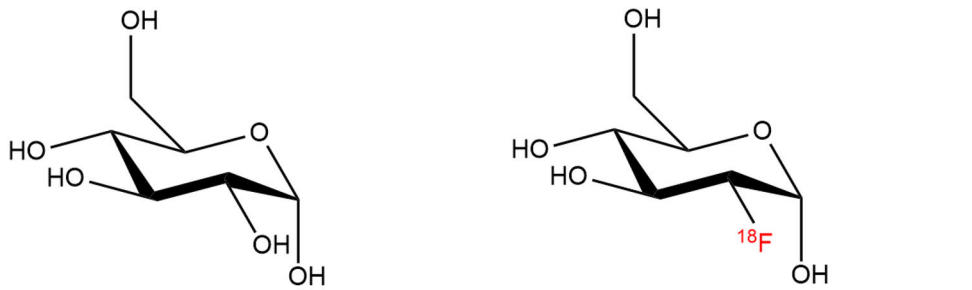

Figure 14. Chemical structures of glucose and [^{18}F]FDG drawn in "3D-chair" form. Note: the naturally occurring L-amino acids previously described do not suggest that the D-version of sugars are not normally used as the letters D and L describe only bond stereochemistry.

The addition of this radionuclide inherently adds a radionuclide that can decay and be detected, though the location of this substitution has another important effect. By removing the hydroxyl group at this location, it renders the molecule partially indigestible by the usual mammalian enzymes yet still allows it to pass through native transport proteins. In practical terms, it can go everywhere normal unadulterated glucose goes at a slightly slower rate (Reivich *et al.*, 1979), but as it gets digested, it will get stuck partway through metabolism and be trapped in the cell digesting it. In the digestive pathway, glucose is first phosphorylated into glucose-6-phosphate, though without the hydroxyl in the deoxy version, the process practically stops here (Burt *et al.*, 2001). This is quite an important feature as the radionuclide attached to this molecule will therefore accumulate as other molecules get trapped and ultimately produce an increase in detectible PET signal. Without this feature, [^{18}F]FDG would still produce a measurable increase in signal based upon overall cell metabolism, though the signal would not be as strong since there would be a flow of [^{18}F]F out of the cell. While there are some pathways that do eventually eject the phosphorylated [^{18}F]FDG (Southworth *et al.*, 2003), it does not go through the normal glycolytic metabolic pathway and occurs at such a slow rate that it is not practically relevant to PET imaging. As [^{18}F]FDG has been studied extensively over more than the past 50 years and has quite a deeply understood pharmacology, it is often used as a reference compound to compare newly developed radiopharmaceuticals to. Whether unfortunate that new compounds are not always making improvements and dethroning this radiopharmaceutical from its throne atop of the field of nuclear medicine, the field has been fortunate to have discovered such a well-suited molecule so early in its conception.

One important consideration when dealing with any sort of widely used energetic substrate as a molecule to radiolabel is that its normal analogue's use in the body can also provide additional hurtles. Sugar processing is quite universal, and it is especially so in the mammalian brain and other energy-processing organs. While this resulting large accumulation in specific organs can be a good thing in many cases, it can make it potentially more difficult to detect smaller regions within this area which have an increase in uptake. For the brain, which relies nearly exclusively on glucose metabolism for energy, this effect can be quite significant. There can be many reasons that drive the necessitation of brain PET imaging, though in the case of gliomas it can be important detect some specific pieces of information. The tumour(s) size(s), location(s), and relative aggressiveness are all important in potentially planning the treatment of a subject (Galldiks *et al.*, 2021). Having a high background signal of radiation from basal glucose consumption of the healthy cells surely doesn't make it easier to detect additional signals.

While entirely possible to photograph some stars during the day with sophisticated enough equipment, it is generally far easier to photograph them at night in the absence of additional background light pollution…

2.6.2 Amino Acids: [^{11}C]Met and [^{18}F]FET

Amino acid-based PET imaging is the next logical step after energy metabolite-based imaging with respect to cancers. As cells divide, they inherently need large amounts of L-amino acids to make copies of everything to divide between the daughter cells causing a large increase in the uptake and processing of amino acids (Nurse and Wiemken, 1974). Non-dividing cells will still require some amount of amino acids for normal function due to the production proteins and other normal biological processes, but a dividing cell will need more. The previous discussion of L and D isoforms (Section 2.3) demonstrates the importance of the L-form for the majority of known life. Perhaps the most commonly used amino acid-based PET imaging

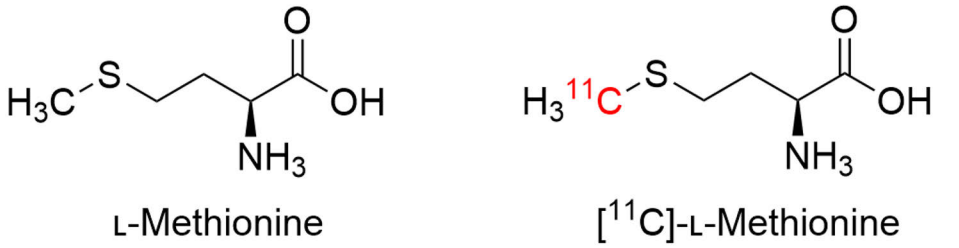

Figure 15. Chemical structure of natural L-methionine and the radiolabelled carbon-11 (highlighted in red) version used in nuclear medicine.

radiopharmaceutical for imaging brain tumours is L-(2*S*)-2-amino-4-[^{11}C]methylsulfanylbutanoic acid or carbon-11-labelled L-methionine ([^{11}C]Met) (Glaudemans *et al.*, 2013). By radiolabelling a compound with a radionuclide that is the same atom type (but different isotope) of the one it is replacing it is possible to ensure that the radiopharmaceutical has the exact biochemical characteristics as the non-radioactive version (Figure 15). Thus, [^{11}C]Met behaves just as normal methionine in the body apart from its decay from carbon-11 into boron-11 with a relatively short physical half-life of 20.38 minutes.

[^{11}C]Met can then follow this same gradient, in a glioma for example, and increases in accumulation can be detected in PET imaging. The downsides to this particular radiopharmaceutical are that methionine, despite being an important amino acid, is the second least used amino acid in the human genome (Pan *et al.*, 2014). The other shortfall, which is common to all carbon-11-based radiopharmaceuticals, is that the relatively short physical half-life of the radionuclide presents some difficulties with respect to practical handling. Synthesizing the

compound, transport to the patient, injection, and subsequent accumulation of the radiopharmaceutical all take time and every ~20 minutes half of the compound has decayed. Despite these issues, carbon-11-based radiopharmaceuticals are still an extremely valuable tool for nuclear medicine. The ability to accurately replicate a naturally occurring biochemical compound by replacing a stable carbon atom with one that will decay and release a positron requires no chemical changes to the compound, which would affect its natural function and pharmacokinetics in a living system. Therefore, it is straight-forward method to directly study where such a compound is going to and accumulating in the body as the addition of another atom, such as fluorine, can have wildly differing effects.

Another common amino acid PET radiopharmaceutical for PET imaging brain tumours is the tyrosine-based L-[^{18}F]fluoroethyl-tyrosine ([^{18}F]FET) (Figure 16) (Bashir, Asma et al 2019). Like most amino-acid-based radiopharmaceuticals, it relies on existing transport proteins for the native analogue to get into the brain.

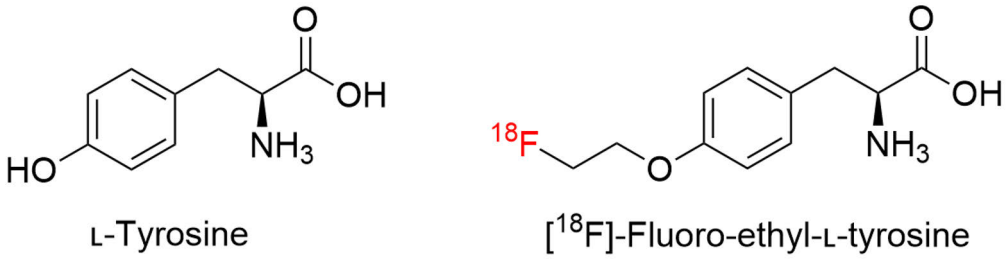

Figure 16. Chemical structure of natural L-tyrosine and the clinically used radiolabelled analogue [^{18}F]FET (right).

Cells with depleted levels of tyrosine create a gradient that allows the flux to favour the direction towards those cells. Although [^{18}F]FET does have some structural changes to it, it can still be brought along the same consumption gradients, which pull the natural analogues in for protein synthesis. It has been noted that this method of transport, common to most amino acids, has its uptake limited by also relying mostly on these passive gradients to get into brain (Hutterer *et al.*, 2013). With the generally low overall cellular replication rate of a developed brain, *i.e.*, it is mostly not actively dividing and growing in an adult subject, there are relatively fewer amino acid transport proteins on the blood brain barrier. With this overall low background uptake level, it is still quite possible to detect small regional increases in amino acid consumption using amino acid-based radiopharmaceuticals for PET imaging. With a lower background level, it is possible to increase relative contrast between a higher level. Thus, the general principal for imaging gliomas is simple: A rapidly dividing cell will consume a greater proportion of what few amino acids that are imported into the brain causing a local depletion. This depletion will then create

a gradient for more amino acids to travel along into these cells which amino-acid-based radiopharmaceuticals can also potential utilize leading to their accumulation in these cells. This increase in uptake is also therefore directly biochemically relevant to the aggressiveness (in terms of replication speed and underlying protein synthesis) of the tumour subtype and it has been shown extensively in literature that there is a strong correlation between these factors (Tsun and Possemato, 2015; Cormerais *et al.*, 2016).

2.6.3 Other: Ligands and Beyond

There are many other radiopharmaceutical design strategies for detecting cancer and more specifically brain tumours. Although not employed in the evaluations presented in this thesis, other approaches are important enough to warrant mentioning. One of the main types of approaches, alluded to in the folate section 2.4.1, is to exploit protein-ligand interactions. A ligand interaction occurs between a protein or proteins' surface and a target molecule (including another protein) with some 3D specificity which is dictated by its shape and chemical environment (Williams and Daviter, 2013). It is not a true non-covalent chemical bond which occurs in this state (normally and by definition, though exceptions technically exist), but instead interacts with the other chemical forces such as hydrogen bonding, its hydrophobicity, *etc.* The overall group of ligand interactions is broad and technically encompasses nearly all radiopharmaceuticals in some way since the vast majority require some type of interaction with a biological receptor to enter or interact with a cell. For example, the [^{18}F]FDG has a multitude of transporting proteins in cell membranes, which interact specifically with sugars to bring them into the cell.

Exceptions exist and include many simple smaller molecules like radiowater ([^{15}O]H_2O), which allows a direct measurement of water perfusion throughout the body, or salts like fluorine-18-enriched sodium fluoride ([^{18}F]NaF), which is absorbed into bone tissue (though arguably also transported via ion-exchange proteins in a "ligand-like" way).

The ligand-like interaction is a staple of many common drugs due to the potential cellular or proteo-specificity that can be achieved and nuclear medicine is no stranger to it. The basic principle is that you have a type of receptor or protein on a cell or target, which has a specific three-dimensional structure and interacts with specific molecules which fit the corresponding structure both physically and chemically. This type of ligand-target can be exploited by a wide variety of small to very large molecules depending on the target receptor shape. There is a very well-established history in nuclear medicine utilizing radiolabelled antibodies derived from immune cells (Kręcisz *et al.*, 2021), antibody fragments and small proteins (Fu *et al.*, 2018), short amino acid chains (Rangger and Haubner, 2020), small molecules that block

specific proteins (Hicks *et al.*, 2010), short mRNA and RNA peptides that bind to targets (Liu *et al.*, 2022) and the previously described single amino acids section (2.6.2).

2.6.4 (2*S*, 4*R*)-4-[^{18}F]fluoroglutamine ([^{18}F]FGln)

Much like the naturally occurring amino acid glutamine (Glutamine 2.3), [^{18}F]FGln (Figure 17) can act as both an amino acid as well as an energetic metabolite. During protein synthesis, which rapidly dividing cells inherently need to do at an increased rate to support their cell division, [^{18}F]FGln can be incorporated into proteins in the

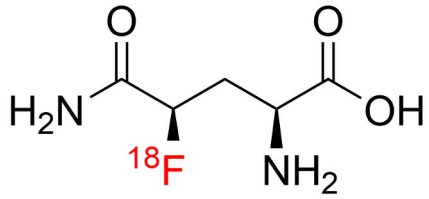

(2*S*, 4*R*)-4-[^{18}F]fluoroglutamine

Figure 17. Chemical structure of [^{18}F]FGln.

same manner as normal glutamine (Lieberman *et al.*, 2011; Dunphy *et al.*, 2018). The other stereochemistry combinations have been examined (*i.e.:* (2*S*, 4*S*)-, (2*R*, 4*R*)-, and (2*R*, 4*S*)-) but were found to not be taken up by cancer cells in as fast of a rate (Lieberman *et al*., 2011). The 2*S* designation, in this case, indicates that the amino acid is in the L-amino acid category giving some reasoning to its cellular-preferred format. After import, protein incorporation is not the only reason for [^{18}F]FGln to be taken into cells. It is also used as an energy-producing metabolite and can be broken down as an alternative fuel for the same Krebs cycle (Figure 6) as glucose. Although not as energy-producing per molecule as glucose, glutamine can be harnessed for energy and is done so naturally in humans during times of carbohydrate depletion (*e.g.,* during starvation, or a ketogenic diet and lack of carbohydrates (Palmer and Clegg, 2021). Coincidentally, many cancer types have long been shown to have developed additional methods of increasing glutamine uptake and breakdown for energy to support their excessive metabolic requirements (Wasa *et al.*, 1996; Venmar *et al.*, 2015). In some cases, cancers have been labelled "glutamine addicted" due to their extreme glutamine consumption, which can even deplete blood glutamine levels by a significant amount (Wise and Thompson, 2010). Due to these factors, [^{18}F]FGln can be used to effectively detect cancer lesions with an increased rate of glutamine consumption. This accounts for a significant proportion of cancers, but being an energetic substrate is not without inherent issues. The body is quite efficient at breaking down energy metabolites to use for energy

production and this digestion is generally not ideal for PET imaging. Perhaps the most problematic aspect of this is that defluorination (*i.e.,* breaking-off the $[^{18}F]F^-$ from the Gln).

To complicate things further, metabolism is often a messy process and is no exception in this case. There are multiple products that are formed via multiple pathways, and each has their own rate and factors that influence them. An in-depth description of the known glutamine processing pathways is elegantly presented in literature (Yelamanchi *et al.*, 2016) and many of those can be applied to [^{18}F]FGln provided the fluorine atom does not interfere with its interaction with digestive proteins.

2.6.4.1 Preclinical [^{18}F]FGln

Preclinical [^{18}F]FGln studies have investigated a wide variety of cancer types and report increased tumour uptake and positive sentiment towards PET image quality. Some animal models have utilized subcutaneously grafted animal glioma cells (Lieberman *et al.*, 2011) while others have investigated subcutaneously grafted human glioma cells in animal models (Venneti *et al.*, 2015; Zhou *et al.*, 2017). Fewer studies, however, have examined the radiopharmaceutical in intracranially grafted animal tumour models (Venneti *et al.*, 2015).

The main findings of these studies are that [^{18}F]FGln has positive PET imaging qualities with the drawback of showing considerable digestion of the compound. Unfortunately, as indicated via the bone uptake *in vivo*, it is often reported that defluorination is likely occurring. Generally, this is regarded as a sub-optimal attribute as it brings more radiation dose to bone tissue which can potentially have long term adverse effects. With this in mind, if there are any bone lesions, they will also be highlighted in a similar mechanism to [^{18}F]NaF imaging. To address the issue of defluorination, a few different studies have been published which modify the chemical structure in the hopes that they can retain its cancer-uptake properties while inhibiting the metabolism and ultimate defluorination (Zha *et al.*, 2018). Unfortunately, these studies have not be entirely successful in the sense that while they have reduced the defluorination and digestion problem, the additional modifications may have reduced the imaging efficacy and cellular uptake. This is understandable since glutamine is a relatively small amino acid, so changes to the chemical structure do not have so many locations to choose from and small additions may be quite impactful to its overall properties.

2.6.4.2 Clinical [^{18}F]FGln

The clinical trials of [^{18}F]FGln are ongoing (Clinical Trial ID: NCT01697930) and these, along with other human trials, have produced some inspiring early results published in literature (Venneti *et al.*, 2015; Dunphy *et al.*, 2018; Liu *et al.*, 2018; Xu *et al.*, 2018). Despite known issues with digestion in preclinical results carrying over to the clinic, the imaging capabilities of this radiopharmaceutical are promising. The first article to come forth from clinical evaluations demonstrated a situation where the usual [^{18}F]FDG PET imaging falls short (Venneti *et al.*, 2015).

In the presented figure from their work (Figure 18), they show an MRI (A) and two PET images (B and C) of the same subject that has two distinct glioma lesions pointed out with red arrows. The larger lower mass shows a clear positive signal in both the [^{18}F]FGln (B) and [^{18}F]FDG (C) images but the smaller lesion further towards the top of the images is not so clear in the [^{18}F]FDG scan. In such cases, it could be questioned whether the smaller upper region could be overlooked if the clinicians only had access to [^{18}F]FDG PET imaging. The higher background levels on this image makes it particularly more difficult to delineate smaller tumours as the extra noise can mask their signal.

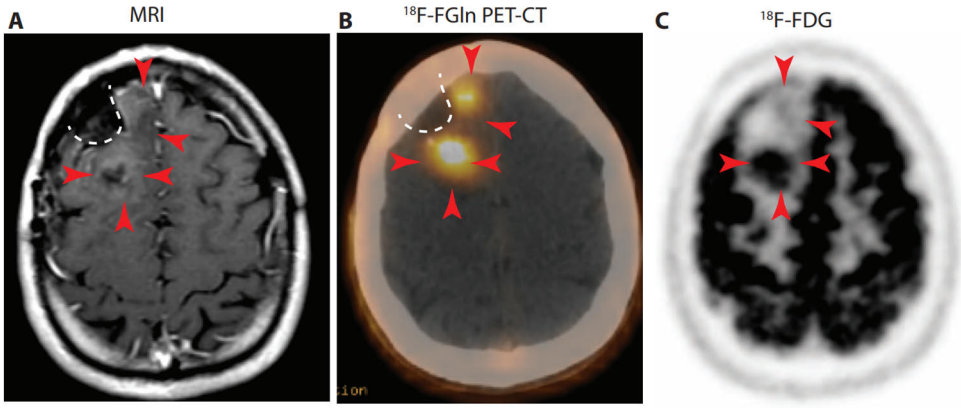

Figure 18. Panel array of a human subject *in vivo* imaged with multiple imaging modalities. A: Contrast enhanced MRI, B: [^{18}F]FGln PET merged with CT, C: [^{18}F]FDG PET
From: [Vinneti, S. et al 2015]. Reprinted with permission from AAAS.

Clearly, knowing about the existence of a secondary lesion can only help with patient treatment planning and considering its accumulation of [^{18}F]FGln (Figure 18, B, top area), this would suggest that it is somewhat metabolically active and very likely dividing. Missed cells are one of the major ways cancer relapse and the recurrence of brain tumours occurs which is why the current therapy standards employed use chemotherapy to attempt to eradicate the remaining cells (Current

Treatment Strategies 2.2.2.3). A large, missed mass of aggressive cancer cells is pretty much assuredly going to continue to grow.

Another more recent clinical study of [^{18}F]FGln has been reported by the same group in New York, USA and demonstrates the imaging effectiveness of the compound for a wide variety of cancer types including gliomas (Dunphy *et al.*, 2018) along with further research into the pharmacokinetics of the compound in humans (Grkovski *et al.*, 2020). Here, the authors report lower rates of metabolism and increased *in vivo* stability in human subjects ($n = 41$) when compared with existing literature preclinical results. Demonstrating that after 30- and 65-minutes post-radiopharmaceutical-injection 73% ± 8% and 69% ± 7% remained intact in the patients' blood circulation respectively. Bone uptake is still present in all clinical studies demonstrating a degree of defluorination, though the relative amount present in the PET images is qualitatively lower than soft tissue and cancer lesions versus what can be observed in animal imaging.

On the other side of the world in Beijing, China, more clinical investigations of [^{18}F]FGln are being performed. The need for a non-[^{18}F]FDG radiopharmaceutical for the brain that has low basal uptake is emphasized here by (Xu *et al.*, 2018). These authors also demonstrate favourable PET imaging characteristics for detecting various cancers throughout the body which have developed new brain metastases. The fourteen patients with suspected metastases that have formed new lesions In the brain have their primary lesions and cancer types traced back to: breast cancer, lung adenocarcinoma, melanoma, and ovarian cancer. Several of the imaged subjects were assessed with both [^{18}F]FGln as well as [^{18}F]FDG and present similar findings to other clinical research work. The same theme as the previously discussed Figure 18 is demonstrated in their sample figures, which show a clearly visible and delineated glioma lesion in the [^{18}F]FGln brain images, and lower (but positive) detection abilities in the [^{18}F]FDG counterparts. Here, the authors present favourable PET imaging characteristics of [^{18}F]FGln for detecting brain metastases. Two other important imaging factors are also discussed, most importantly that [^{18}F]FGln uptake is not dictate by oedema in the same manner as [^{18}F]FDG. This is an important factor especially when examining post-surgery and post-chemotherapy treatment assessment as after these events there will often be swelling of the affected area due to the physical damage of therapy and immune cell clean-up of dead cells from chemotherapy. Secondly, the authors also image the primary cancerous lesions in the subjects with mixed results. They report overall positive imaging characteristics but note that imaging organs with high native glutamine uptake (such as the liver) may not be as useful. Furthermore, as bone uptake is present of the defluorinated [^{18}F]F^-, caution must be taken when attempting to assess whether the increased bone uptake signal is a bone lesion.

2.6.5 Al[^{18}F]F-NOTA-folate ([^{18}F]FOL)

Various folate-based radiopharmaceuticals have been developed over the rich history of the scientific community's research into folate and its relation to cancer cell replication (Müller, 2013; Boss and Ametamey, 2020; Scaranti *et al.*, 2020). The aims of all of these imaging radiopharmaceutical variants of the folate molecule are more or less the same: to detect and characterize the increased use of folate in cells along with its accompanying often-increased expression of folate receptors. Both parameters are hallmarks of many different cancer types due to the intrinsic relation between folate and DNA synthesis required for cellular replication (Ulrich and Potter, 2007). The natural forms of folate have been well-characterized biochemically with respect to what portions of the molecule interact with receptors and other proteins. With this knowledge in mind, it becomes ever-so-slightly more straightforward to alter the structure on the opposite side of the binding side to allow for various radiolabelling possibilities without interfering with its functionality. The most important factor when designing a radiolabelled analogue of a naturally occurring compound is, after all, to usually ensure that the compound can still interact with native transport proteins despite the chemical structure modifications.

Although there are many different radiolabelled folate analogues that exist, the specific Al[^{18}F]F-1,4,7-triazacylononane-1,4,7-triacetic acid-conjugated folate (Figure 19), commonly shortened to Al[^{18}F]F-NOTA-folate is herein designated as "[^{18}F]FOL" and others are denoted by longer names to properly differentiate them.

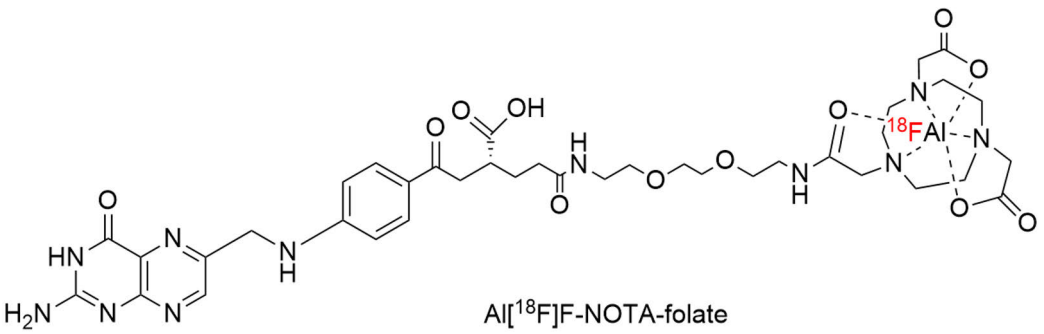

Figure 19. Chemical structure of [^{18}F]FOL.

2.6.5.1 Preclinical ^{18}F-labelled Folate

The specific radiopharmaceutical [^{18}F]FOL has yet to be used extensively to PET image cancer and no studies investigating brain tumours exist. One study, however, has demonstrated efficacy for PET-imaging subcutaneously xenografted KB skin cancer tumours and A549 lung cancer tumours in mice (Chen *et al.*, 2016). One very similar compound to [^{18}F]FOL has been synthesized by the same group, which has an additionally extended polyethylene glycol chain elongating the distance between the NOTA chelator and the folate molecule (Figure 20) (Chen *et al.*, 2017). This Al[^{18}F]F-NOTA-PEG-folate compound has also shown favourable PET imaging characteristics for imaging the same tumours as in their previous work. The PET-imaged tumours in these studies are also shown to have increased FR-α presence which is likely a strongly contributing factor to their increased folate-based radiopharmaceutical uptake.

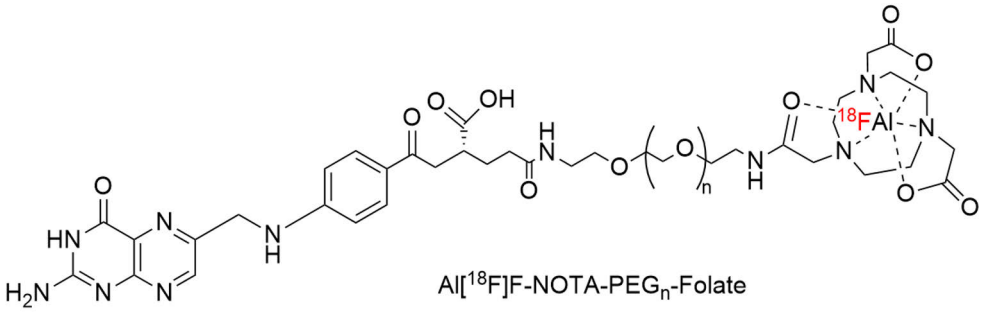

Figure 20. Chemical structure of Al[^{18}F]F-NOTA-PEG$_n$-folate.

2.6.5.2 Clinical ^{18}F-labelled Folate

As of the start of year 2023 there are no published clinical studies or trials that have used any folate analogues to PET image brain tumours nor any that have used the specific [^{18}F]FOL compound in humans. There is, however one ongoing clinical trial evaluating the use of 3'-Aza-2'-[^{18}F]fluorofolic acid ([^{18}F]F-Aza-FOL) (Figure 21) (Clinical trial ID:NCT03242993) which has reported data from six patients with adenocarcinoma of the lung (a type of cancer than can occur in many different organs) (Gnesin *et al.*, 2020). Although the structure is similar to the [^{18}F]FOL discussed and it is based on normal folate, it is still a different compound. The ongoing phase I clinical trial reports the recruitment of 30 more subjects with either ovarian cancer or lung-based cancer. All of the subjects' histology results indicate positive signals for FR-α reporting staining apart from 6 subjects. The trial has not

been concluded yet, though in the 2020 manuscript the authors describe favourable PET imaging characteristics with a low radiation burden to patients. There are no other ^{18}F-labeled folate analogue clinical trials currently ongoing for imaging cancer though one folate analogue, [^{18}F]fluoro-PEG-folate (similar to the Al[^{18}F]F-NOTA-PEG-Folate investigated for tumour imaging on the preclinical side), has seen a first-in-man PET imaging study to investigate rheumatoid arthritis and may see future clinical trials (Verweij *et al.*, 2020).

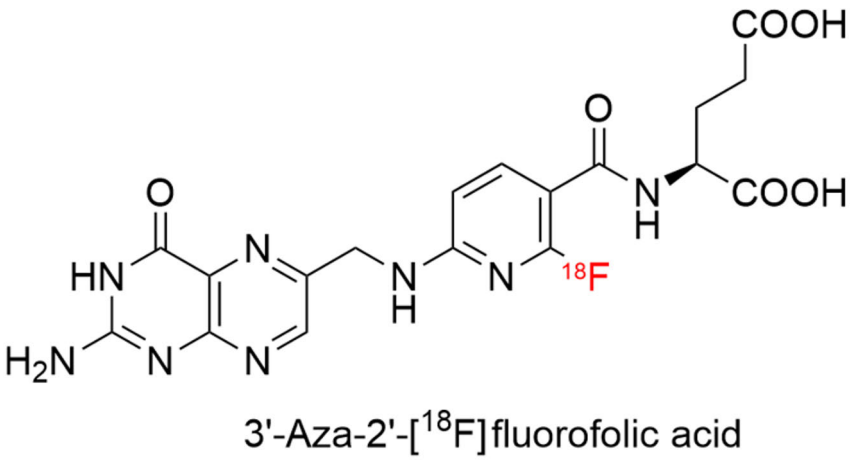

Figure 21. Chemical structure of 3'-Aza-2'-[^{18}F]fluorofolic acid

3 Aims

The purpose of these studies was to synthesize the newly emerging radiopharmaceuticals [^{18}F]FGln and [^{18}F]FOL and examine their efficacy for PET imaging experimental gliomas in animal models. Included were also additional relevant assessments pertaining to the metabolism, pharmacokinetic modelling, MRI imaging to unbiasedly delineate tumour dimensions and *loci*, a comparative analysis between two separate PET/CT imaging systems, and an investigation into clinical translational relevance to predict if human imaging would also be successful. Additionally, comparatively testing these radiopharmaceuticals with the commonly clinically used radiopharmaceuticals [^{18}F]FDG and [^{11}C]Met was also a goal. The specific aims of these studies were:

1. To PET image both animal and human cell-derived gliomas (xeno)grafted orthotopically or subcutaneously into animal models with [^{18}F]FGln and [^{18}F]FDG. (Study I)

2. To evaluate multiple pharmacokinetic models of [^{18}F]FGln for future reference and comparative quantitative analyses. (Study I)

3. To PET image glioma-bearing animal subjects with all three of: [^{18}F]FGln, [^{18}F]FDG, and [^{11}C]Met for direct same-subject comparison of imaging efficacy. (Study II)

4. To PET image glioma-bearing animal subjects with two separate camera systems and evaluate their end-result comparability with respect to *in vivo* imaging. (Study II)

5. To PET image glioma-bearing rat subjects with [^{18}F]FOL and [^{18}F]FDG to contrast *in vivo* imaging capabilities (Study III)

6. To histochemically assay human patient-derived tumour samples for the presence of folate-relevant receptors examining potential clinical translational relevance. (Study III)

4 Materials and Methods

4.1 Radiopharmaceuticals: Syntheses and Quality Assays

Radiolabelling of the emerging radiopharmaceuticals [^{18}F]FGln and [^{18}F]FOL are described and outlined in detail whereas the routinely produced clinical-grade radiopharmaceuticals also used in the studies is not for the sake of simplicity and their well-established production and use. See Study II supplementary data for additional details (Miner *et al.*, 2021).

4.1.1 Radionuclide Production

The fluorine-18 in study I was produced with a MGC 20 cyclotron (Efremov Institute of Electrophysical Apparatus, Leningrad, USSR, presently St. Petersburg, Russia) which has since been decommissioned. For the rest of the studies performed, either the Cyclone 3 (Ion Beam Applications, Ghent, Belgium) or the Compact Cyclotron 18/9 MeV (Efremov Institute of Electrophysical Apparatus, St. Petersburg, Russia) were used for radionuclide production.

In all cases, roughly 0.8 mL of [^{18}O]H_2O was loaded into the respective cyclotron's liquid target chamber and irradiated with a proton beam until the sufficient desired amount of [^{18}F]fluoride was generated via the $^{18}O(p, n)^{18}F$ reaction (see: 2.5 Positron Emission Tomography (PET)). The resulting product was then sent to a lead-shielded fume hood and loaded onto a synthesis-specific cartridge for radiopharmaceutical production. Unless otherwise specified, all water used was purified to 18.2 MΩ via various ultra-pure water filtration systems routinely checked and serviced. The custom built multi-use remotely operated radiosynthesis device made by DM-automation (Nykvarn, Sweden) (Simplified schematic: Figure 22, Actual device: Figure 12) was used to synthesize both [^{18}F]FGln and [^{18}F]FOL.

Quality assessments were performed with high performance liquid chromatography (HPLC) in all cases apart from [^{18}F]FDG quality assessment which is robustly and routinely performed with both HPLC and thin layer chromatography (TLC). Radiochemical yield (RCY) is calculated by assessing the end of synthesis

radioactivity, multiplying by the assayed % purity, and being decay corrected to the start of synthesis. Then, the RCY was obtained by dividing the decay corrected yield by the starting radioactivity and multiplying by 100 %.

All radiation work was carried out under strict compliance with regulations set forth by the Radiation and Nuclear Safety Authority of Finland (STUK)

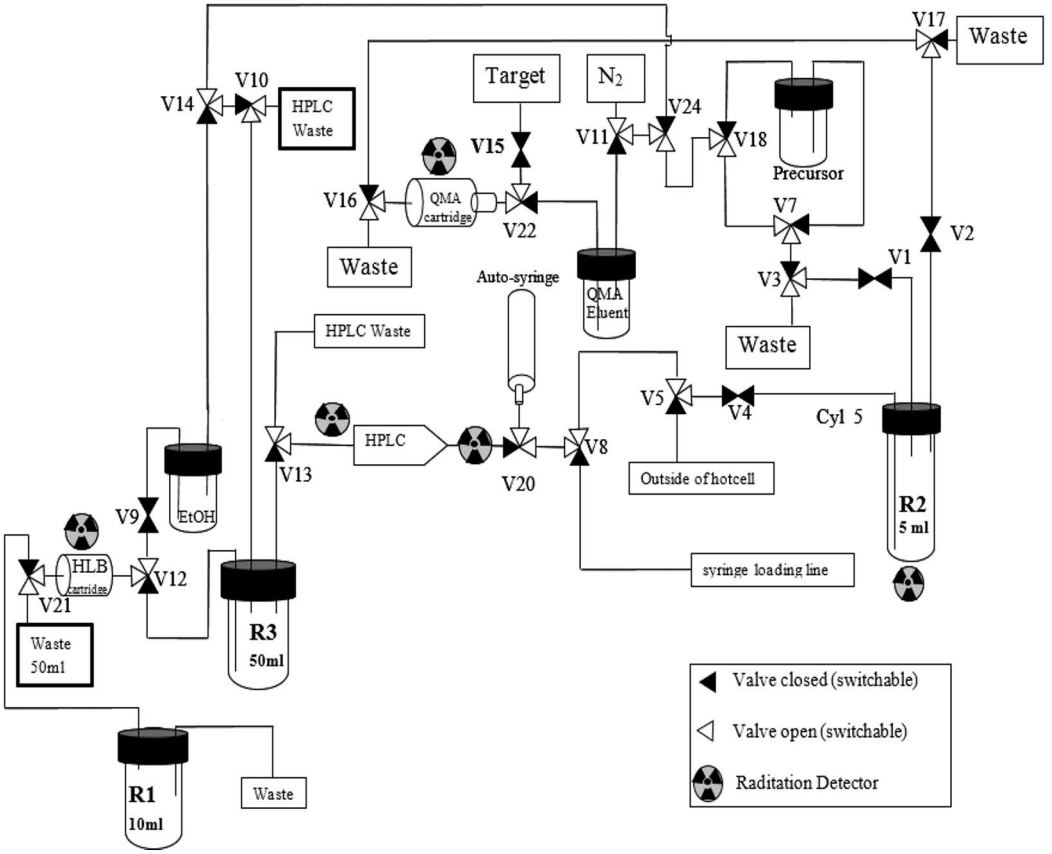

Figure 22. Simplified DM Automation multi-use remote controlled radiosynthesis device connection diagram

4.1.2 [^{18}F]FGln

Precursor

The precursor, (2*S*, 4*S*)-tert-butyl-2-(tert-butoxycarbonylamino)-5-oxo-4-(tosyloxy)-5-(2, 4, 6- trimethoxybenzylamino) pentanoate (Figure 23), for the production of [^{18}F]FGln was initially developed and published by (Qu *et al.*, 2011) from the research group of Prof. Dr. Hank F. Kung at the University of Pennsylvania. The physical samples used for these syntheses were generously provided by Prof. Dr. Jason Lewis and Dr. Ouathek Ouerfelli at the Memorial Sloan Kettering (MSK) Cancer Center Organic Synthesis Core Facility, New York, New York, USA. It must be noted that the precursor compound is exceptionally sensitive to water and moisture and careful handling and processing during synthesis must be taken.

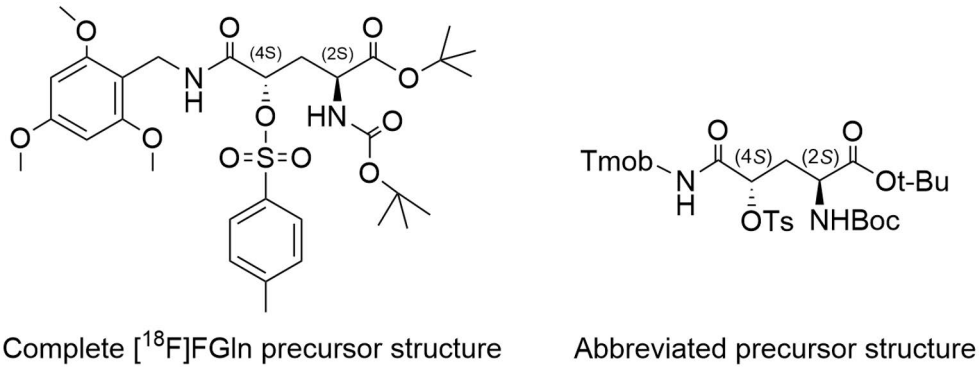

Complete [^{18}F]FGln precursor structure Abbreviated precursor structure

Figure 23. Full (left) and abbreviated (right) chemical structure of the [^{18}F]FGln chemical precursor (2*S,* 4*S*)-tert-butyl-2-(tert-butoxycarbonylamino)-5-oxo-4-(tosyloxy)-5-(2, 4, 6-trimethoxybenzylamino) pentanoate. Tmob = 2,4,6-trimethoxybenzyl, Ts = Tosylate, HBoc = tert-butyloxycarbonyl, t-Bu = tert-butyl.

Radiolabelling

(Refer to Figure 22 for simplified synthesis device diagram)

Approximately 12 GBq of [^{18}F]F^- was received onto a pre-conditioned (10 mL 3% K_2CO_3 in H_2O followed by 20 mL water) Waters Sep-Pak Accell Plus QMA Plus Light cartridge (WAT023525) and was then eluted into R2 with 2000 µL of liquid comprised of 16.5 mg 18-Crown-6 ($C_{12}H_{24}O_6$), 3.0 mg of potassium bicarbonate ($KHCO_3$), 77 µL H_2O, and 1923 µL of acetonitrile (CH_3CN). The vessel was then heated to 115˚C under 70 mL/min flow of nitrogen gas for approximately 25-27 minutes and 2 minutes past any visible moisture in vessel or the outflowing line. After cooling to 55 ˚C, 10 mg of the precursor (Figure 23) dissolved in 500 µL dry acetonitrile was added and the vessel was heated to 70 ˚C for 15 minutes. After

cooling to ˚C, 800 µL of liquid comprised of 500 µL water and 300 µL acetonitrile was added and then the solution was injected into a semi-preparative HPLC system with a Waters X Terra Prep MSC18 10 µm 7.8 × 300 mm column installed. The eluent gradient utilized 0.1 % formic acid in water and 0.1% formic acid in acetonitrile. The gradient started from an equal mix of both eluents changing gradually to 70% of the acetonitrile-based eluent after 20 minutes and the desired fluorine-18 labelled intermediate (Figure 24) eluted at 15 minutes into R3 which was filled with 25 mL of water.

The intermediate product was then loaded onto a preconditioned (3 mL dry ethanol followed by 5 mL water) Waters Oasis® HLB Plus Light Cartridge which was then eluted with 1 mL of dry ethanol into R1. The vessel was heated to 90 ˚C under 100 mL/min nitrogen flow until completely dry (approximately 20-25 minutes) and cooled to 40 ˚C. The final synthesis step, the removal of protecting groups, was accomplished via the addition of 595 µL of trifluoroacetic acid and 5 µL of anisole, heating to 50 ˚C for 3 minutes, and then the liquid was evaporated after a further 2 minutes at 50 ˚C under 60 mL/min nitrogen gas flow (Figure 24). The product was cooled to 40 ˚C and then 2 mL of phosphate-buffered saline (pH 6.5) was added. A small aliquot was then drawn for quality control purposes while bulk of the product sent for the rest of the studies.

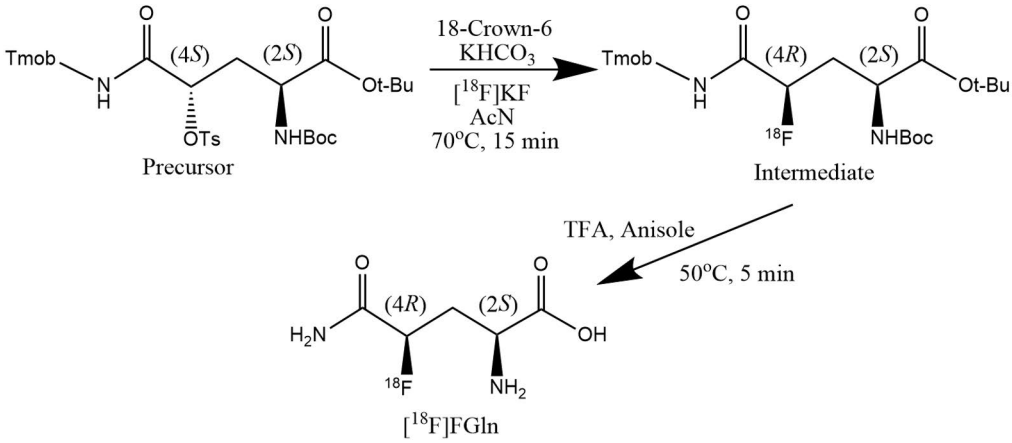

Figure 24. [^{18}F]FGln synthesis overview

Radiochemical Purity and Quality Assay

The aliquot taken for radiochemical purity testing was diluted in 1 mM copper sulphate ($CuSO_4$) solution to a radiochemical concentration of 1 MBq/100 µL and a 100 µL was used for HPLC injection. HPLC assay utilized a Chirex Phenomenex

3126 (D)-Penicillamine 25 cm × 4.6 mm column (CA, USA) chiral column and a Hitachi HPLC system (Merck D-7000 interface, L-7400 UV detector set to 220 nm, L-7100 pump system) with a Bicron flow scintillation counter for radioactivity detection. The mobile phase used was an isocratic flow of 1 mM $CuSO_4$ with the product eluting at approximately 11.6 minutes. Shelf-life and stability analyses were performed by leaving a synthesized batch at full concentration at room temperature and drawing an aliquot for testing every hour for 4 hours. Non-radioactive reference compounds were generously provided by the MSK cancer center along with the radioactive compound precursor and samples of both *D*–glutamine and *L*-glutamine (Sigma Aldrich, MI, USA) were also assayed with the same methods at various combinations of concentrations to ensure chiral separation functionality and expected retention times.

4.1.3 [^{18}F]FOL

Precursor

The [^{18}F]FOL precursor compound, 1,4,7-triazacylononane-1,4,7-triacetic acid-conjugated folate (Figure 25) was generously provided by Prof. Dr. Philip Low's lab from Purdue University (IN, USA) and allows for a very convenient one-step synthesis via heating.

Radiolabelling (Refer to Figure 22 for simplified synthesis device diagram)

Roughly 6 GBq of [^{18}F]F^- was received onto a pre-conditioned (1 mL ethanol, followed by 1 mL water) Chromafix PS-HCO_3-45mg cartridge and was then eluted with 220 µL of physiological saline into R2 which contained 20 µL polypropylene glycol, 40 µL of a 1M acetate-buffered (pH 4) 2 mM aluminium chloride solution, 70 µL of acetonitrile, and 50 µL of a 200 nm solution of precursor in water (Figure 25). The vessel was then sealed and heated to 100 ˚C for 15 minutes before cooling to 40 ˚C (Figure 25), adding 800 µL of 0.1% TFA in water and then injecting into a semi-preparative HPLC column (Phenomenex Jupiter Proteo 250 × 10mm). The HPLC system used 0.1% TFA dissolved in water (A) and the same in acetonitrile (B) running an eluent gradient from 95% A to 70% A after 25 minutes running at 4.0 mL/min. The desired product ([^{18}F]FOL) was eluted after roughly 15 minutes into a R3 containing 20 mL of water, 150 µL 1.0 M Sodium bicarbonate ($NaHCO_3$), and 100 µL of freshly prepared 0.1 M gentisic acid. The product was then slowly loaded onto a preconditioned (10 mL ethanol, followed by 10 mL water) Waters tC18 cartridge (product no.: WAT036805) and eluted with 500 µL of 50% ethanol into a pre-

loaded formulation vial containing 2mL of 9% polypropylene glycol in PBS. A small 5 µL aliquot was drawn from this for further quality control testing with the bulk of the product being sent for planned studies.

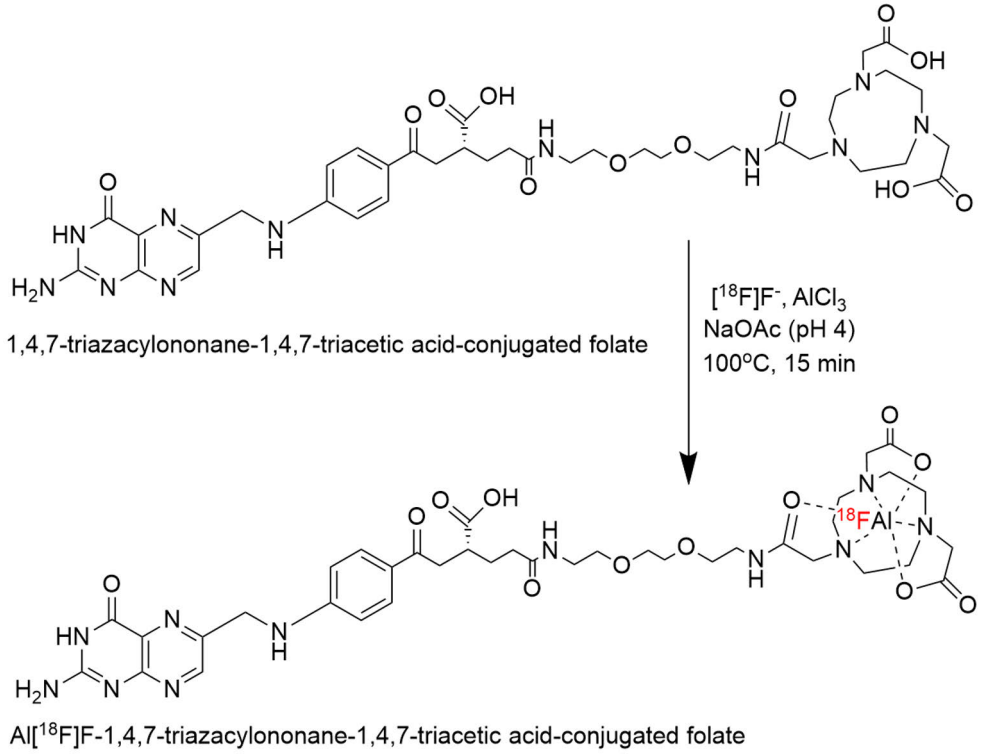

Figure 25. Top: The [^{18}F]FOL precursor, 1,4,7-triazacylononane-1,4,7-triacetic acid-conjugated folate prior to radiolabelling. Bottom: [^{18}F]FOL product, Al[^{18}F]F-1,4,7-triazacylononane-1,4,7-triacetic acid-conjugated folate.

Radiochemical Purity and Quality Assay

The radiochemical purity was assayed via HPLC (system setup described earlier in: 4.1.2, with UV detector instead set to 280 nm) by diluting the drawn sample aliquot in 0.1% TFA water to a radiochemical concentration of approximately 0.7 MBq / 100 µL and injecting it into a Phenomenex Jupiter Proteo 250 × 4.6mm column. The eluents used were (A) 0.1 % TFA in water and (B) 0.1% TFA in acetonitrile which were run at 1.0 mL/min with a linear gradient starting from 89 % A to 75 % A by 15 minutes with the desired product eluting at approximately 10 minutes. Shelf-life and stability analyses were performed by leaving a synthesized batch at full concentration at room temperature and drawing an aliquot for testing every hour for

4 hours. Cold standards of [^{19}F]FOL, which were generously provided by Prof. Dr. Philip S. Low's lab, and unlabelled precursor were assayed with the same methods to ensure agreeance between retention times and precursor purity in the latter sampling case.

4.2 Animal Models and Experimentation

The experimentation on animals was deemed necessary for accomplishing the studies' goals with *in vivo* experiments being required to more accurately test the radiopharmaceuticals in a complex "real" environment. All studies were performed with the utmost respect to the animal subjects and every measure possible to ensure minimal discomfort or pain was observed. Every experiment utilizing animal subjects was approved by an ethics committee from the national project authorization board in Finland (License no.: ESAVI/6805/04.10.07/2011, ESAVI/4161/04.10.07/2015, and ESAVI/12691/04.10.07/2017). All studies were carried out in accordance with European Union legislation (EU Directive 2010/EU/63) regarding protection of animals used for scientific purposes. Animals were given analgesic medication (0.01 mg/kg buprenorphine and 5 mg/kg carprofen) when necessary to ensure no pain was felt during surgeries. Anaesthesia medication was administered during surgeries, imaging and sacrifice. All animals were fed and given water *ad libitum*. Genetically modified immunocompromised mice were utilized to increase the successful chance that human tumour xenografts would be successful while the rats used were immunocompetent with rat tumour still grafts growing successfully. During deep isoflurane anaesthesia, subjects were sacrificed via cervical dislocation after cardiac puncture if end-point blood sampling was being assayed.

4.2.1 Mice Bearing Subcutaneous BT4C Rat Gliomas

In study I, six athymic nude mice (Foxn1$^{nu/nu}$, Envigo, Gannant, France) at 7 weeks of age were injected with roughly 250,000 rat BT4C glioma cells suspended in 50% cell culture medium and 50% Matrigel in 50 μL aliquots into the hind leg and neck region while under isoflurane anaesthesia. BT4C cells were cultured first at 37°C in the presence of 5% CO2 in Dulbecco's modified Eagle medium, 10% foetal calf serum, and a 0.5% mix of penicillin-streptomycin (10,000 units/mL of penicillin and 10,000 μg/mL of streptomycin in a 10 mM citrate buffer). Tumour growth could be visually tracked from the exterior and the mice (averaging 35.6 g ± 2.2 g) were imaged 5 weeks later with all tumours exceeding 1 cm in diameter.

4.2.2 Mice Bearing Orthotopic Human BT3 Gliomas

In study I, an intracranial glioma model was made with three 9-week-old female athymic nude BALB/cOlaHsd-Foxn1^{nu} mice (Institute of Animal Genetics, Edinburgh, UK) which were injected with patient-derived BT3 tumour cells genetically modified to express luciferase (Le Joncour, V. *et al* 2019). Under anaesthesia and analgesia an incision was cut into the scalp and skin peeled back allowing a small hole drilled into the skull in which the tumour cells were injected slowly over the course of five minutes (Ø 0.2 mm, location: bregma: 1 mm anterior, 2 mm to right, 3 mm depth). The skin was sutured back and tumour growth progression was monitored with *in vivo* bioluminescence detection on an IVIS Spectrum system (Perkin Elmer, Hopkinton, MA, USA) with subjects being imaged 12 days later.

4.2.3 BDIX Rats Bearing Orthotopic BT4C Tumours

BDIX-Ifz (herein termed BDIX) rats were used in study II (8-week-old, 9 male and 7 female) and study III (64-week-old, 9 male) were injected via similar surgical methods as section 4.2.2. BT4C cell culturing was performed in the same manner as 4.2.1 and the injection location as follows: 1 mm posterior bregma, 2 mm lateral right, with 2.5mm depth. In study II, the (up to) 4-day long imaging protocol began 21 days post-tumour grafting while in study III, the longitudinal imaging study began after 16 days and finished on day 32.

4.3 *In Vivo* Imaging Studies

In study I, the luciferase-expressing genetically altered glioma strain allowed for an economical way to confirm and monitor a rough approximation of tumour growth progress by monitoring the detectable signal output of the tumour between 530-640 nm light emissions through the brain, skin and skull (see 4.2.2). The PET imaging protocols used varied slightly from project-to-project dependant on well-established literature guidance and previous PET-centre experience (in the case of [^{18}F]FDG) and a lack of excessive existing understanding of (animal-glioma specific, in the case of [^{11}C]Met) the emerging radiopharmaceuticals ([^{18}F]FGln and [^{18}F]FOL) and practical considerations. For example, knowing that the BBB transport of some radiopharmaceuticals is far lower than with [^{18}F]FDG and not wanting to risk wasting a day of imaging with useless results, an increased injection activity (compared with [^{18}F]FDG) was often used. When using and comparing different camera systems (such as in Study II), the maximum radioactivity that can be injected is dictated by camera sensitivity which, if exceeded, would overload the sensors ruining the image acquisition. In all imaging studies, animals were under 2-2.5 %

isoflurane anaesthesia and, if additional studies were forthcoming, allowed to recover under isolation and supervision. If the endpoint of the study was reached, animals were painlessly sacrificed under deep anaesthesia with tissues and blood being collected for further *ex vivo* studies (4.5).

4.3.1 MRI Imaging

In Study II and Study III MRI Dotarem® (Guerbet LLC, Villepinte, France) contrast-enhanced imaging was used on days prior to PET imaging protocols. For Study II, MRI imaging was performed on day 30 before the (up to) 3-day PET imaging protocol would be performed. Study III examined a more longitudinal protocol having MRI imaging of some subjects being performed on days 15, 18, and 31 prior to PET imaging days. The MRI machine used in both studies was the Achieva 3T MRI (Koninklijke Philips N.V., Eindhoven, Netherlands) with a rat brain array coil no. 4 (RAPID Biomedical GmbH, Rimpar, Germany). Imaging protocol utilized both T1 and T2 weighted imaging prior to contrast agent injection with a T1 weighted imaging protocol 5 minutes post Dotarem® injection.

4.3.2 PET/CT Imaging

Static CT imaging was always acquired for attenuation correction of the PET images immediately before the subjects were injected with radiopharmaceutical samples. In the case of delayed injection imaging with a later imaging window, the radiopharmaceuticals were injected earlier and the attenuation correction CT was performed so that it would allow the PET image acquisition to start on planned time (40-45 minutes post injection). The Inveon multimodality small animal PET/CT scanner (Siemens Medical Solutions, Munich, Germany) allowed for imaging two subjects at a time when an even number of subjects were available (all studies) while subjects were imaged one at a time in the smaller Molecubes X-Cube and β-Cube (Molecubes NV, Gent, Belgium) (Study II). Subject details are listed in Table 1 while PET image duration and framing (acquired in list-mode) are listed in.Table 2.

Table 1. List of study subjects, imaging numbers, and injected radioactivity amounts.

	Species	Total subjects	Radiopharmaceutical, subjects PET imaged	Camera, subjects imaged	Injected radioactivity (MBq)
Study I	Mouse	9	[^{18}F]FGln, 9	Inveon, 9	11.2 ± 1.0
Study II	Rat	16	[^{18}F]FGln, 13	Inveon, 9	15.7 ± 1.1
				Molecubes, 4	5.2 ± 0.4
			[^{18}F]FDG, 7	Inveon, 4	10.1 ± 0.6
				Molecubes, 3	5.3 ± 0.3
			[^{11}C]Met, 12	Inveon, 8	50.2 ± 2.8
				Molecubes, 4	10.7 ±1.3
Study III	Rat	9	[^{18}F]FOL, 5	Inveon, 5	39.4 ± 1.4
			[^{18}F]FDG, 4	Inveon, 4	29.6 ± 1.4

Table 2. PET imaging framing.

	Radiopharma-ceutical	Imaging delay time (min)	Framing	Imaging duration (min)
Study I	[^{18}F]FGln	0	6 × 10 s, 4 × 60 s, 5 × 300 s, 3 × 600 s	60
Study II	[^{18}F]FGln	0	6 × 10 s, 4 × 60 s, 5 × 300 s, 3 × 600 s	60
	[^{18}F]FDG	0	6 × 10 s, 4 × 60 s, 5 × 300 s, 3 × 600 s	60
	[^{11}C]Met	0	6 × 10 s, 8 × 30 s, 5 × 60 s, 2 × 300 s	20
Study III	[^{18}F]FOL*	0	6 × 10 s, 4 × 60 s, 5 × 300 s, 9 × 600 s	120
	[^{18}F]FOL	45	1 × 1200 s	20
	[^{18}F]FDG	45	1 × 1200 s	20

*Two-subject subset imaged in pilot project to determine optimal imaging window.

4.3.3 *In Vivo* Image Analyses

All *in vivo* image analyses were performed with Carimas software developed at the Turku PET centre and available for download (http://turkupetcetre.fi/carimas). When available (Study II & Study III) MRI imaging performed before PET imaging was used to unbiasedly delineate tumour boundaries and draw regions of interest (ROIs). The healthy brain area selections were made by selecting the entire brain and subtracting a 2-voxel-radially expanded version of the tumour area (example in Figure 26). In study I where MRI imaging was not performed, the subcutaneous tumours were easily distinguishable from normal tissue due to their protruding

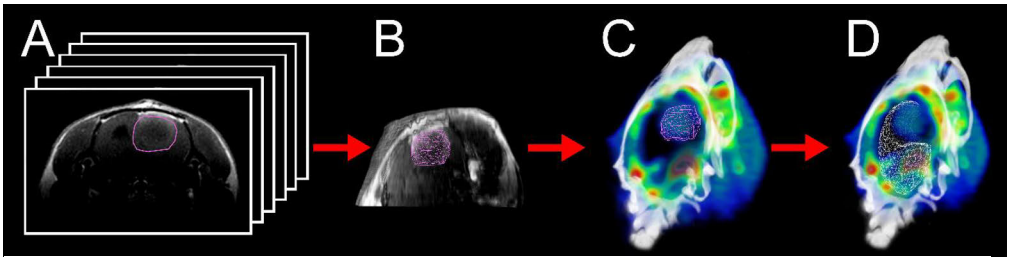

Figure 26. Unbiased MRI-led analysis workflow from. **A** Drawing 2-dimensional ROIs on MRI slices **B** converted 2-D ROIs into a 3-dimensional tumour region **C** Tumour ROI overlain on PET/CT image **D** Brain region formed with tumour region subtracted overlain on PET/CT image.

bulbous nature from the body CT images. For the orthotopic tumours in Study I, the hole in the skull that was still visible in the CT images was used as a reference point upon which immediately under the tumour region limits were estimated by clearly increased radiopharmaceutical uptake. The underlying data in the PET image ROIs was converted into standardized uptake value (SUV) which accounts for differences in subject weight as well as total injected dose. In static images (20 minutes, single frame), the tumour-to-brain uptake ratios (TBR) were determined by dividing the average tumour region radioactivity by the average brain ($Tumour\text{-}SUV_{mean}$/$brain\text{-}SUV_{mean}$). For dynamically acquired PET images (60-120 minutes, complex framing) the maximum occurring TBR (after 5 minutes where image noise can be high) is reported as TBR_{max} from the average SUV values occurring at that time point for that subject. Histograms and framing ranges were performed as time-weighted-means and values set specifically to each subject, radiopharmaceutical, and camera with the intention of displaying the highest level of contrast between tumours and adjacent tissue. Visual representations shown in sample figures were all set to tri-cubic interpolation methods to incorporate the most amount of three-dimensional voxel data into a visually understandable two-dimensional pixel image.

4.4 *In vivo* Stability Analyses

In all studies, *ex vivo* collection included end-time point blood samples which were separated into blood cell and plasma fractions and estimate the end time point *in vivo* radiopharmaceutical data at a single time point. In Study I and Study II, more detailed [^{18}F]FGln *in vivo* stability analyses were performed with multiple sampling time points. This required the use of additional subjects, often injected with additional radioactivity to ensure a large enough remained for more detailed assay via HPLC methods. Using three separate analyses on the sampled blood, the red blood cell uptake, plasma protein incorporation and parent-radiopharmaceutical purity data were all divulged to estimate the total bioavailable fraction of parent-radiopharmaceutical at each time point. A curve was then fit to the average time

points which could be applied to blood radioactivity levels in the PET image data (Heart left ventricle ROI) which could be used to correct input functions for pharmacokinetic modelling. Blood sampling time points were generally at 5 min, 15 min, 30 min, 45 min, and 60 min. A single blood sample was taken from each mouse subject while two 150-200 µL samples were drawn from rat subjects due to total blood volume constraints and impact on the subject. Study I utilized 12 healthy male mice (6 c47BL/J6 and 6 Foxn1$^{nu/nu}$) which were injected with 9-14 MBq of [^{18}F]FGln. Study II used 10 (5 male, 5 female) healthy BDIX rats injected with 40 MBq of [^{18}F]FGln. Subjects were all sacrificed during the final blood sample draw via cardiac puncture under deep isoflurane anaesthesia. The description of the three assays that describe the fraction of parent-tracer bioavailability (and then could be multiplied together for each time point) are elaborated upon in the following sections.

4.4.1 Red Blood Cell Uptake Assay

How much radiopharmaceutical is trapped in the red blood cells unable to go into target tissues?

Whole blood samples transported on ice in pre-weighed heparin-coated vials were weighed and then measured for radioactivity with a 3″ Hidex NAL well counter. Samples were gently inverted several times to mix, then centrifuged at 700 × *g* at 4 ˚C for 5 minutes. The plasma supernatant was then separated into a new pre-weighed vial and both fractions were weighed and measured for radioactivity levels. The plasma fraction and whole blood levels were used to calculate the plasma radioactivity fraction in a way to avoid inevitable leftover plasma contamination of the RBC fraction. The RBC measurement was kept as a backup reference to ensure divided radioactivity fractions added up to roughly whole blood level. The following Equation 1 Was therefore used:

$$Plasma\ Radioctivity\ Fraction\,(t) = \frac{C_p}{C_{RBC} + C_p} = \frac{\rho_p C_p (HCT)}{\rho_b C_b - \rho_p C_p (1-HCT) + \rho_p C_p (HCT)}$$

Equation 1. Plasma radioactivity fraction calculation without using red blood cell activity inputs. Where: C = radioactivity level, ρ = density, and HCT = hematocrit. Subscripts denote: p = plasma, RBC = red blood cell, and b = whole blood.

4.4.2 Plasma Protein Binding Assay

How much radiopharmaceutical is not stuck to a larger protein unable to go into target tissue?

An 80 µL aliquot from the plasma samples in 4.4.1 were mixed with 200 µL of methanol and were vortexed vigorously for 1 minute causing the proteins to precipitate. The mixture was then centrifuged at 11,000 × *g* at room temperature for 10 minutes. The supernatant was then separated from the precipitated protein pellet, and both were assayed for radioactivity. The results were converted into a fraction to represent the relative amount of the unbound radiopharmaceutical, or alternatively "plasma free-fraction", are in the plasma (Equation 2).

$$Unbound\ Plasma\ Protein\ Radioctivity\ Fraction\ (t) = \frac{C_{sup}}{C_{sup} + C_{pel}}$$

Equation 2. Calculation used to approximate the unbound plasma protein fraction where C = radioactivity level and Subscripts denote sup = supernatant and pel = pellet

4.4.3 Parent-radiopharmaceutical Plasma Purity

How much of the plasma free-fraction radioactivity is the parent radiopharmaceutical?

The plasma supernatants obtained from 4.4.2 were then assayed via HPLC to divulge the fraction of the radioactivity that was the parent [^{18}F]FGln radiopharmaceutical via established methods (Zhou *et al.*, 2017). Briefly, the HPLC system utilized an Astec® CHIROBIOTIC® T Chiral HPLC column 5 µm, 250 mm × 4.6 mm (Sigma-Aldrich) running 80 % methanol with water at a rate of 1 mL/min as the mobile phase. A flow scintillation detector which provided a constant stream of output data. Cold fluorine-19 standard as well as freshly synthesized [^{18}F]FGln were used to compare retention times with the plasma-derived samples and identify which peak corresponded to the [^{18}F]FGln. The other peak identifications were based off of the findings of Zhou, R., *et al* 2017. The relative amount of [^{18}F]FGln in percent based on HPLC results was then adjusted based on the purity of the injected radionuclide

$$Relaive\ Plasma\ Purity\ (t)\ = \frac{P_{detected}}{P_{injected}}$$

Equation 3. Relative plasma purity calculation where P = HPLC purity in percent and subscripts denote the detected purity from the sample versus the original injected activity purity.

using the sample Equation 3 to equalize differences of synthesized batches on different study days.

4.4.4 Bioavailable Parent Plasma Free-fraction

How much of the total blood radioactivity is the parent radiopharmaceutical freely floating in the plasma and therefore able to travel in to target tissue at a given time?

All the fractions from the preceding sections were combined by multiplying them for each time point and then converted into percent if not already done so in their calculations. The results were plotted with an additional manufactured point at t = 0.1 minutes and given a value of 100%. A natural logarithmic curve was fitted to these points to approximate the bioavailable fraction (in percent) of the whole blood radioactivity at a given time point which would not be unavailable for target tissue uptake due to RBC uptake (4.4.1), Plasma protein binding (4.4.2), or no longer existing as the in-tact parent [^{18}F]FGln radiopharmaceutical (4.4.3).

4.4.5 Pharmacokinetics and Modelling

To adequately describe the modelling in sufficient detail would require a thesis of its own and thus it is (relatively) merely a brief mention in this dissertation. A wealth of modelling knowledge is freely available from the Turku PET centre daughter website: http://turkupetcentre.net. Modelling scripts used in Study I are available in their respective "scripts for modelling sections" whose batch files are hosted and freely available on Gitlab (https://gitlab.utu.fi/vesoik). Modelling scripts used in Study II were based upon previous scripts used in Study I with a few minor custom updates to suit the project's data structure.

Briefly, both raw inputs from [^{18}F]FGln blood data (heart left ventricle ROIs in PET images) as well as corrected blood inputs for bioavailable fraction (see 4.4.4) were used for each model in both Study I and Study II. Multiple models were applied to the underlying PET data with either based upon assumptions of reversible (Logan and Yokoi), irreversible (Patlak), or compartment-type models (single and multi) binding of [^{18}F]FGln. Tissues ROIs from PET images used in Study I include: Tumour regions (both orthotopic and both subcutaneous locations individually), tumour regions' respective relative healthy tissue (brain and flank muscle), and bone (from the femoral condyle). In study II, additional tissue ROIs input into models include tumours and healthy brain regions.

4.5 *Ex Vivo Studies*

Significant care towards the well-being of the animals used was always undertaken towards ensuring that pain felt was as minimal as possible- especially during animal sacrifice. The fewest number of subjects while still ensuring study significance were also used and as much data as possible was always collected and processed from each subject where practically feasible.

4.5.1 Biodistribution

In all studies performed with [^{18}F]FGln and [^{18}F]FOL a subset of subjects were dissected after sacrifice so that the organs could be weighed and analysed for their amount of radionuclide uptake with a 3″ Nal Triathler well counter system (Hidex Oy, Turku Finland). Organs such as: the whole brain (with tumours) muscle (flank), heart, lung, spleen, liver, pancreas, kidney, small intestine (empty), adrenal glands, salivary glands, thymus, blood, plasma, epididymis (Study I), and urine were collected and processed in this manner. The results were converted into either SUV or percent of the total injected dose of that subject per gram of tissue (%ID/g). Some organs of specific additional interest, such as brains containing tumours, subcutaneous tumours were collected for later cryosectioning and further study.

4.5.2 Cryosectioning

Organs of particular interest, namely the brains with gliomas and subcutaneous gliomas were placed on ice after biodistribution assays and then frozen in liquid nitrogen. Cryosectioning of the tissue into alternating 8 µm for immunohistochemical and immunofluorescence studies and 20 µm slices for clearer autoradiography and haematoxylin and eosin (H&E) staining was performed with a Leica CM3050S cryotome and paced onto Menzel Superfrost Plus slides (Thermo Fischer). The slides were then immediately assayed with methods described subsequently in 4.5.3 Autoradiography.

4.5.3 Autoradiography

The still radioactive cryosectioned tissues on the slides were exposed to radiation sensitive Fuji BAS-TR2025 imaging plates for 3-4 hours (at least two half-lives) and the plates were then developed on a Fujifilm BAS-5000 scanner. The slides were then stored at -70 ˚C for future histology studies. The autoradiographs were analysed with a combination of TINAA software and Carimas software mentioned previously in (4.3.3 *In Vivo* Image Analyses) using light micrographs from the following section 4.5.4 Histology.

4.5.4 Histology

Histological analyses generally involved H&E staining of 20 µm slides via particularly well-established methods used in many fields of science. The slides were scanned with a Panoramic 250 Flash II slide scanner (3DHistec, Budapest, Hungary) and the 3DHistec Case Viewer software was used to examine them. These light microscopy images were then imported into Carimas software and aligned with their respective autoradiographs. Through this, the accurate delineation of tissue boundaries via the light micrograph were applied to the autoradiographs and ROIs drawn.

4.5.4.1 Immunofluorescence

In study III immunofluorescence staining was done for both glioma-bearing rat brain cryosections as well as paraffin-embedded human glioma samples obtained during surgery. Staining of both was done with similar methods with changes to account for the differences in section preparation. Frozen sections were thawed slowly on ice and fixed with a 4% paraformaldehyde solution before being washed with PBS. They were then incubated in bovine serum albumin (10%, 1 hour), washed with PBS and incubated with diluted primary tumour antibody (1:100 for FR-α PA5-101588, Invitrogen, Waltham, MA, USA, 1:200 for CD68 MCA341GA, Bio-Rad, Hercules, CA, USA, and 1:50 FR-β biotinylated m909, generously provided by Prof. Dr. Lowe) at 4 ˚C for 12 hours. Slides were then washed with PBS and incubated with diluted secondary fluorescent antibody (respectively, 1:500 anti-rabbit AlexaFluor 597, A11012, Invitrogen, 1:500 anti-mouse AlexaFluor 488, Invitrogen, or 1:50 Streptavidin DyLight 597 SA-5649, Vector Laboratories, Burlingame, CA, USA). Slides were then washed again in PBS before being incubated in 4’,6-diamindino-2phenylindole (DAPI) (1:10,000 D9542, Sigma-Aldrich) for 10 minutes.

Human glioma paraffin-embedded sections (n = 3) obtained during patient surgery (Turku University Hospital, Auria Biobank, Turku Finland) and healthy brain sections (n = 2) obtained post-mortem) were stained similarly as to above though with key preparation changes due to the differences in storage method. Instead of thawing, the samples underwent a xylene-ethanol series of washes to remove paraffin followed by a citrate buffer (100 mM, pH 6.0) antigen revival for 2 hours in a pressure cooker before being washed with PBS.

4.5.4.2 Immunohistochemical

Immunohistochemical FR-α staining was performed in Study III on both glioma-bearing rat brain cryosections and the human glioma paraffin-embedded sections.

The general thawing (frozen rat glioma samples) and paraffin dissolving (human samples) procedures were performed as previously described in 4.5.4.1. Then, endogenous peroxidases were blocked with Bloxall (SP-6000, Vector Laboratories) for 10 minutes before being washed with PBS. Endogenous protein and avidin were blocked by a 20-minute incubation of 5% normal goat serum (PK-6101, Vector Laboratories) and avidin blocker (SP-2001, Vector Laboratories) before being washed with PBS. Slides were then incubated for 30 minutes with diluted primary tumour antibody (1:100 FR-α PA5-101588, Invitrogen) and endogenous biotin blocker (SP-2001, Vector Laboratories) before being washed with PBS. The sections were then incubated for 30 minutes with diluted anti-rabbit biotinylated secondary antibody (1:200, PK-6101, Vector Laboratories) before being washed with PBS and incubated for 30minutes with an avidin-biotin enzyme complex (PK-6101, Vector Laboratories). Finally, the slides were stained with diaminobenzidine (SK-4100, Vector Laboratories) and incubated for 10 minutes with hematoxylin.

4.5.5 *In Vitro* Binding and Blocking

In Study III, some slides containing 20 μm sectioned tissues were assayed for [^{18}F]FOL binding and blocking via folate-glucosamine addition. The slides were first thawed slowly on ice for 20 minutes and then brought to room temperature over 5 minutes. The slides were then placed in room temperature PBS for 15 minutes, drained, and then a PBS solution containing 0.04 MBq/mL of [^{18}F]FOL was added. For the blocking studies, a 100-fold molar excess of folate-glucosamine was added to the [^{18}F]FOL solution. The slides were then left to incubate at room temperature for 45 minutes upon which both were independently rinsed with a PBS solution chilled to 4 ˚C with two separate fresh baths for 2 minutes each and were finally rinsed with 4 ˚C water. The slides were drip-dried on a tilted rack and excess water on the edge was absorbed with a carefully applied paper towel. The slides were then exposed and scanned with similar methods mentioned in 4.5.3 Autoradiography.

5 Results

5.1 Radiopharmaceutical Synthesis and Characterization

5.1.1 [^{18}F]FGln

The synthesis of [^{18}F]FGln was carried out over the course of 2 hours and yielded 478 ± 78 MBq (n = 8) (decay corrected to 998 MBq ± 105) which, when starting with 12 GBq of [^{18}F]F, corresponds to a decay-corrected radiochemical yield of 8.3% ± 1.0 starting from the end of bombardment. When tested for radiochemical and radiochemical-enantiomeric purity via the previously described methods in 4.1.2, the samples showed a high level of purity (Figure 27). Enantiomeric purity was found to be 97.4% ± 0.7 the desired "2*S* 4*R*" enantiomer while the overall product radiochemical purity was 94.3% ± 1.0.

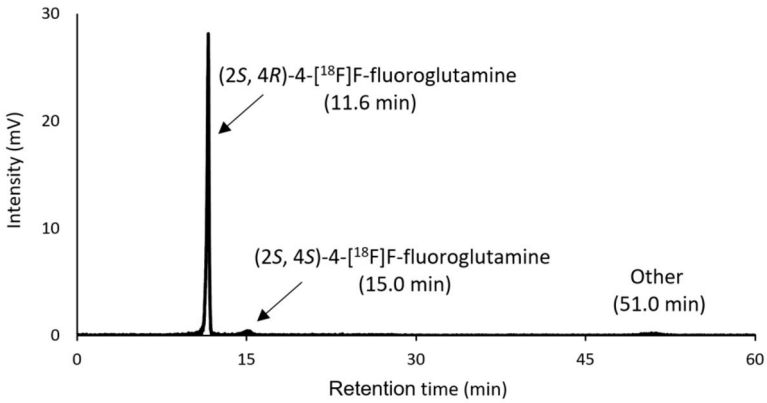

Figure 27. Sample [^{18}F]FGln end-product quality control HPLC flow scintillation chromatogram demonstrating 93.8% (2S, 4R)-4-[^{18}F]fluoroglutamine, 1.4% (2S, 4S)-4-[^{18}F]fluoroglutamine, and 4.8% other.

No appreciable decay in [^{18}F]FGln product purity was found when leaving a 500 MBq sample in a PBS solution (pH 6.5) at room temperature for 4 hours. When leaving a similarly prepared sample in a PBS solution instead at pH 8.0, roughly 15% of the product had degraded.

5.1.2 [^{18}F]FOL

The synthesis of [^{18}F]FOL was carried out over the course of 50 minutes and yielded on average (n = 5) 799 MBq ± 84 (decay corrected to 1095 MBq ± 115) starting from approximately 5 GBq. The decay-corrected radiochemical yield was calculated to be 21.9% ± 2.3 and the radiochemical purity was 97.5% ± 1.6 (Figure 28)

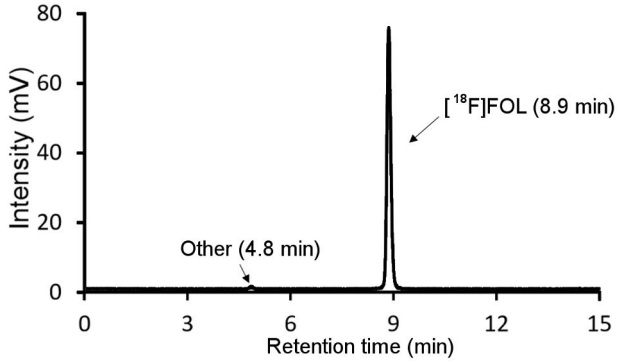

Figure 28. Sample quality control HPLC flow scintillation chromatogram demonstrating 99.0 % [^{18}F]FOL purity with a retention time of 8.9 minutes and 1 % other with a retention time of 4.8 minutes.

No appreciable decay was detected when the end product (diluted to a maximum of 400 MBq/mL) was left at room temperature for four hours.

5.2 [^{18}F]FGln in Mice

5.2.1 PET Imaging

Dynamic 60-minute PET imaging of Foxn1$^{nu/nu}$ mice bearing subcutaneous rat-derived BT4C gliomas and BALB/cOlaHsd-Foxn1^{nu} mice bearing orthotopic BT3 human-derived gliomas demonstrated remarkable successful visualization of the tumours in both cases. For the subcutaneous model (Figure 29), after the [^{18}F]FGln uptake in flank and neck tumours plateaued after 12.5 minutes, on average (n = 6) there was 1.8 ± 0.6 and 2.0 ± 0.8–fold higher accumulation of radiopharmaceutical in the tumours than in the control muscle tissue (Figure 30).

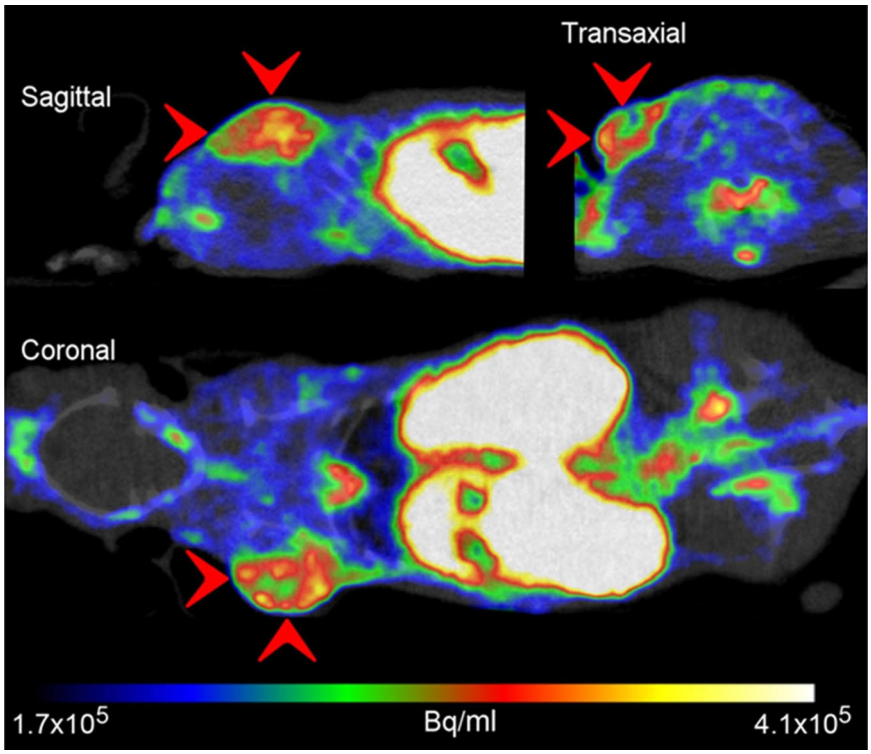

Figure 29. Sample [^{18}F]FGln *in vivo* PET image of a Foxn1$^{nu/nu}$ mouse bearing a subcutaneous BT4C glioma. From a time-weighted mean of frames 1-40 minutes post-injection with tri-cubic interpolation.

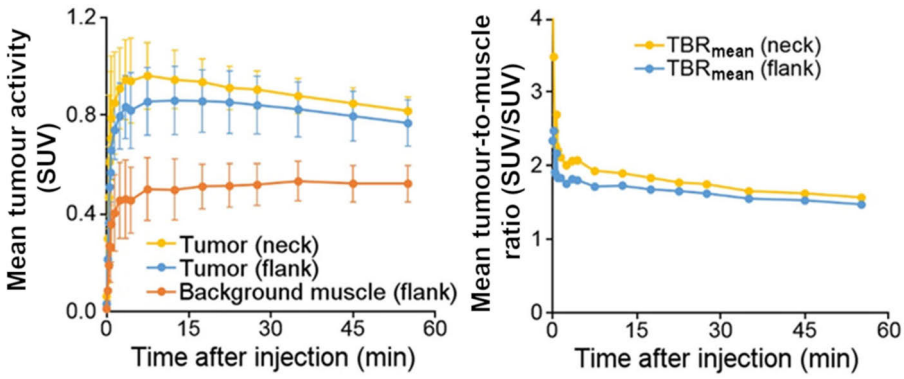

Figure 30. Left: Average (n = 6) PET time-activity curves for subcutaneous BT4C tumour xenografts. Right: Mean tumour-to-muscle ratio for the data displayed on left.

The presence of successful tumour growth in the orthotopic tumour model was detected with bioluminescence imaging which senses the light produced by the luciferase protein (Figure 31, A). In PET images (Figure 31, B), the model displayed high [^{18}F]FGln uptake in the glioma tissue when compared to the adjacent brain tissue divulging TBR values of 4.8 (Figure 32) and 3.6 (data not shown) for subjects 1 and 2 while the PET data from subject 3 was lost due to camera malfunction .

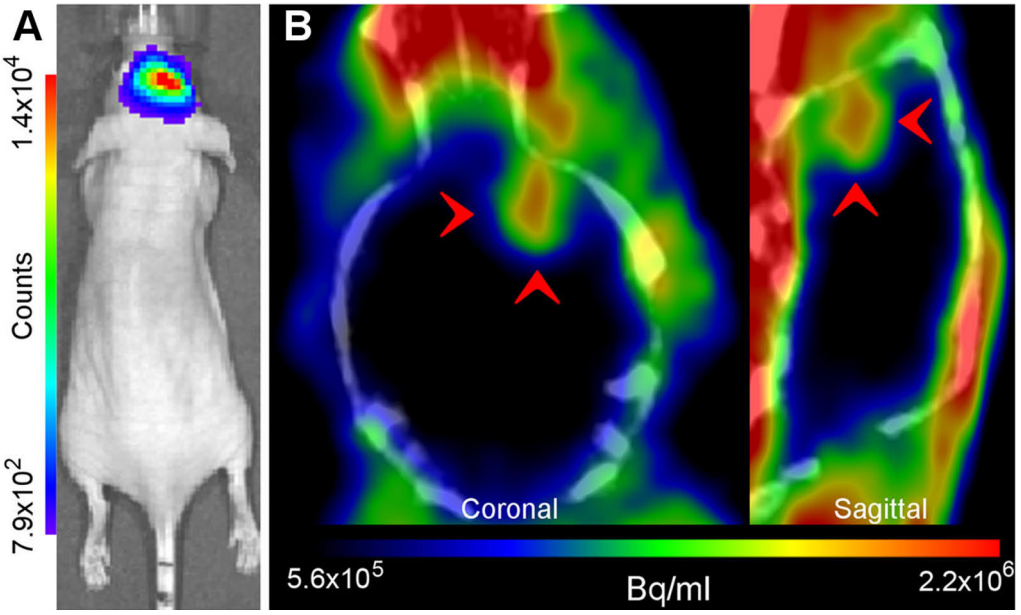

Figure 31. Sample *in vivo* imaging array of BT3 glioma bearing mouse. **A** bioluminescence image. **B** [^{18}F]FGln PET/CT of the head region with glioma pointed out with red chevron arrows.

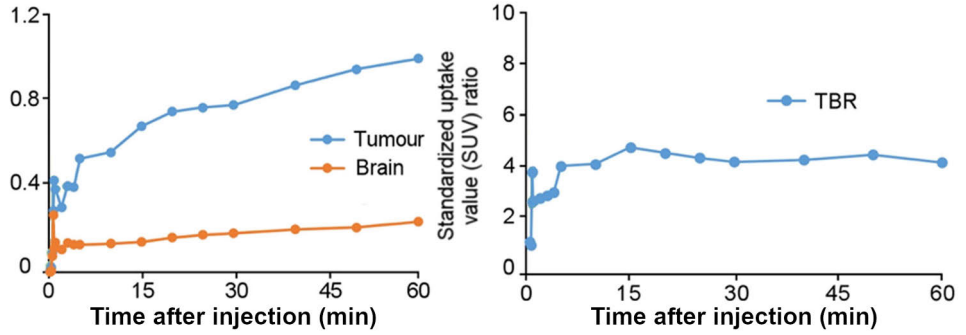

Figure 32. Left: Sample PET image time-activity curve for a BT3 glioma bearing mouse. Right: Tumour-to-brain ratio for the data displayed on the left

5.2.2 [^{18}F]FGln Stability in Mice

The total bioavailable fraction of [^{18}F]FGln in mouse whole blood was calculated for multiple time points via the three separate portions described in section 4.4 and plotted in Figure 33. The graph shows that after 60 minutes post injection, the average bioavailable fraction of [^{18}F]FGln is 42-46% of the total blood radioactivity levels. The curves of best-fit are described by Equation 4 and Equation 5 for average male and female populations respectively which, when multiplied by the injected radiochemical purity, yield the approximate bioavailable fraction of [^{18}F]FGln for a given time in minutes.

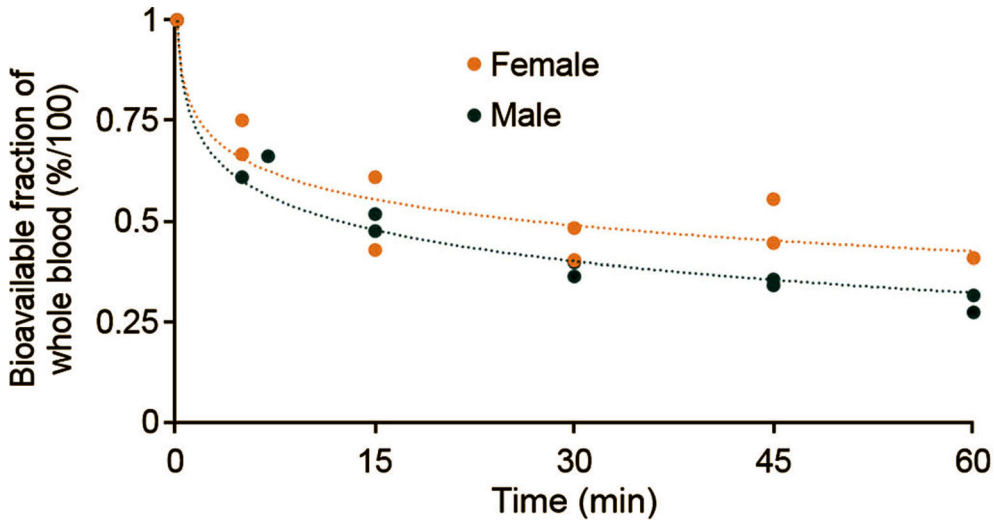

Figure 33. Total bioavailable [^{18}F]FGln fraction of whole blood over time in 1-year-old c57BL/6J male and 3-month-old Foxn1$^{nu/nu}$ female mice.

$$\text{Male Bioavailable Fraction } (t) = (-0.112)\ln(t) + 0.7819 \qquad R^2 = 0.962$$

Equation 4. Bioavailable fraction of [^{18}F]FGln of whole blood radioactivity where t = post injection time in minutes

$$\text{Female Bioavailable Fraction } (t) = (-0.093)\ln(t) + 0.806 \qquad R^2 = 0.8572$$

Equation 5. Bioavailable fraction of [^{18}F]FGln of whole blood radioactivity where t = post injection time in minutes

5.2.3 Modelling in Mice

Multiple pharmacokinetic models were applied to the mouse PET image data with both total blood radioactivity as well as bioavailable fraction of the blood corrected fractions as inputs. Reversible uptake models such as 2-compartment models, Yokoi and Logan (sample in Figure 34) plots revealed a 2 order of magnitude higher value for uptake kinetics versus an irreversible Patlak model suggesting that reversible uptake plays a much more dominant role in the [^{18}F]FGln pharmacokinetics in soft tissues assayed for both corrected and uncorrected inputs. When examining the osseous tissue uptake (femoral condyle) with the models, the reverse is true suggesting that irreversible uptake plays a more dominant role. Significant differences ($p < 0.05$) in model results with respect to corrected and uncorrected blood inputs were found demonstrating a clear difference in result output for each method.

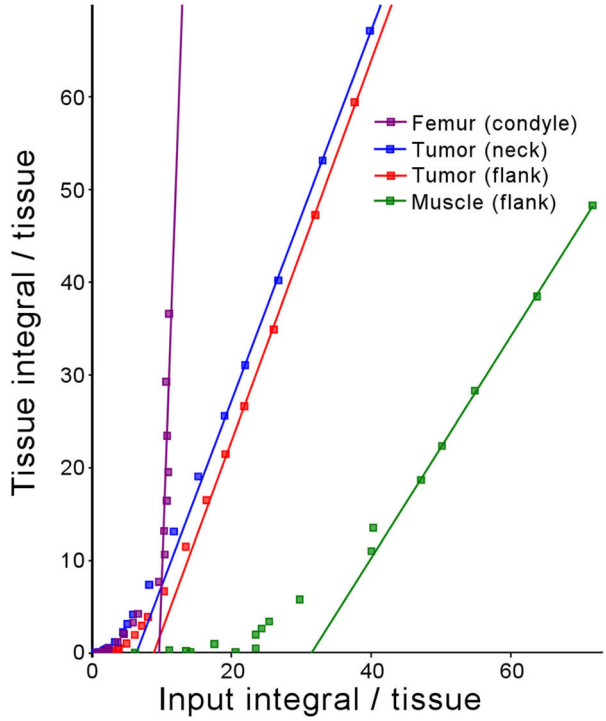

Figure 34. Sample Logan plot from a PET imaged subcutaneous tumour-bearing subject analysed with bioavailable fraction-corrected arterial blood as the input.

Table 3. Logan plot modelling result summary.

Region of interest (n = 6)	Distribution volume (AB)	Distribution volume (CB)
Flank tumour	1.13 ± 0.09	1.96 ± 0.15
Flank muscle	0.77 ± 0.13	1.38 ± 0.23
Neck tumour	1.21 ± 0.08	2.08 ± 0.13
Bone (femoral condyle)	5.11 ± 2.19	13.47 ± 7.70

Acronyms denote AB = Arterial blood radioactivity used as input, CB = "corrected blood" - population-based bioavailable blood fraction used as input.

5.2.4 Ex Vivo

The *ex vivo* results confirmed the presence of large tumour masses in the intracranial tumour model brains (Figure 35, A) while subcutaneous tumours were clearly visible visually from the exterior of subjects. Autoradiography of the intracranial tumours (sample: Figure 35, B) showed average (n = 12 slices per subject) TBR values of 9.5 and 9.9, which is 2 to 3-fold higher than what was observed in PET imaging.

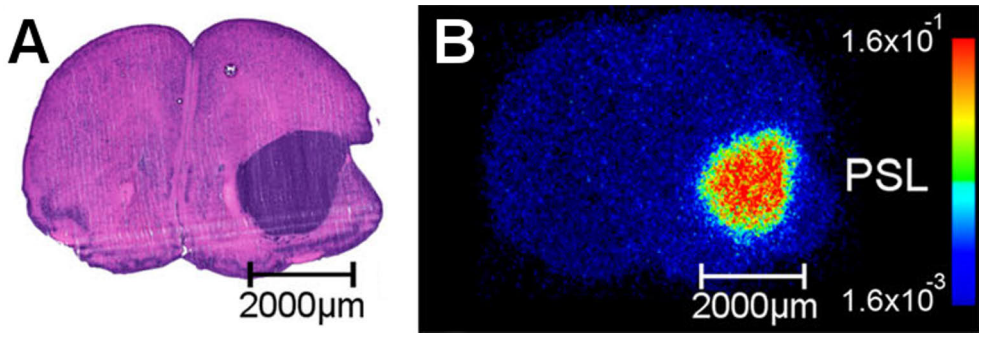

Figure 35. Intracranial BT3 tumour bearing mouse brain 20 µm thick cryosection. **A** Light microscopy image of H&E stained section. **B** [^{18}F]FOL autoradiography image of adjacent slice to the H&E section.

Biodistribution results (example of subcutaneous distribution in Figure 36) showed a high accumulation of [^{18}F]FGln in digestion-related organs such as the pancreas and small intestine along with considerable bone accumulation. Histology demonstrated relatively uniform tumour consistency and a lack of central necrosis in all cases in both models (higher magnification zoom sample image example in Figure 37).

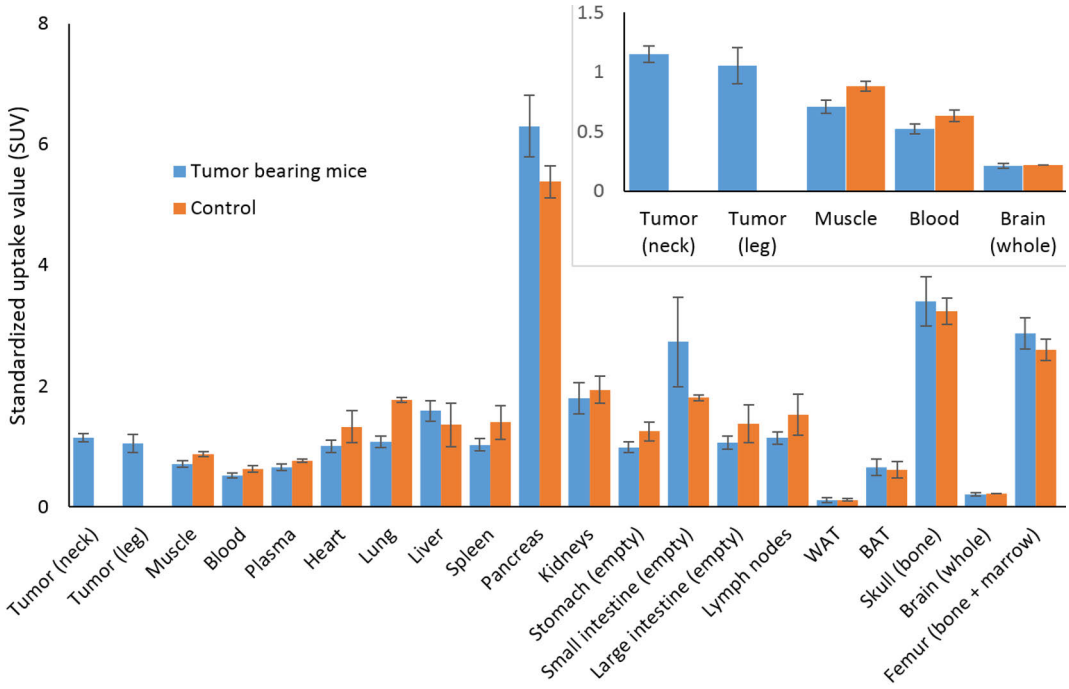

Figure 36. Subcutaneous BT4C tumor bearing Foxn1$^{nu/nu}$ mouse and control C57BL/6Jrj *ex vivo* [^{18}F]FGln biodistribution results 63 minutes post intravenous injection.

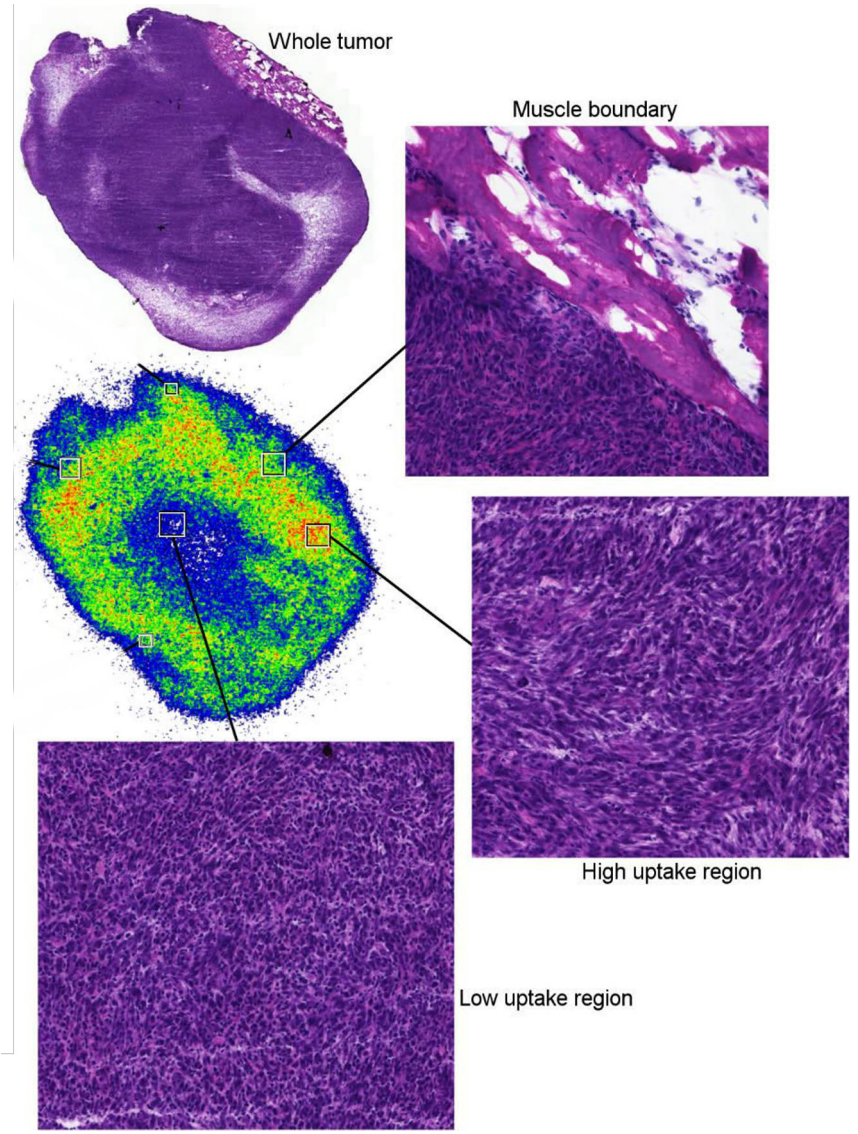

Figure 37. Subcutaneous tumour *ex vivo* histology. Center left: autoradiography, Surrounding areas: An adjacent slice of the same H&E stained tumour and zoomed in areas of different sections.

5.3 [^{18}F]FGln in Rats

5.3.1 PET Imaging

The use of [^{18}F]FGln to image orthotopic BT4C gliomas in rats was shown to be a safe and effective method to detect and delineate the gliomas (example Figure 38, B). When compared directly with the commonly clinically used radiopharmaceuticals [^{11}C]Met and [^{18}F]FDG, [^{18}F]FGln displayed higher contrast between tumour and brain tissue with 2-fold and 1.4-fold higher TBR values respectively. The TBR values observed on average for each radiopharmaceutical reached up to 1.99 ± 0.19 for [^{18}F]FGln (n = 13), 1.08 ± 0.08 for [^{11}C]Met (n = 12), and 1.41 ± 0.11 for [^{18}F]FDG (n = 7). Time-activity curves of the radiopharmaceuticals (Figure 39) showed a much faster blood clearance rate for amino acid-based radiopharmaceuticals (A and B) than that of [^{18}F]FDG.

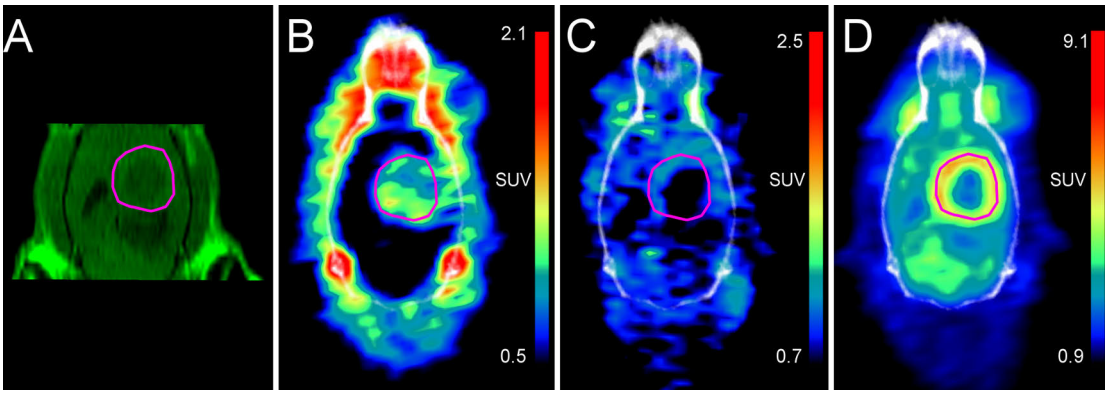

Figure 38. Array of *in vivo* images acquired on four consecutive days of a single BDIX subject bearing a BT4C glioma (outlined in magenta) with tri-cubic visual interpolation. **A** contrast enhanced T1 MRI image used to delineate tumour boundaries. **B** [^{18}F]FGln PET/CT, 15.8 MBq injection, time-weighted mean frames from 15-60 minutes. **C** [^{11}C]Met PET/CT, 50.4 MBq injection, time-weighted mean frames from 9-20 minutes. **D** [^{18}F]FDG PET/CT, 24.0 MBq injection, time-weighted mean frames from 35-60 minutes.

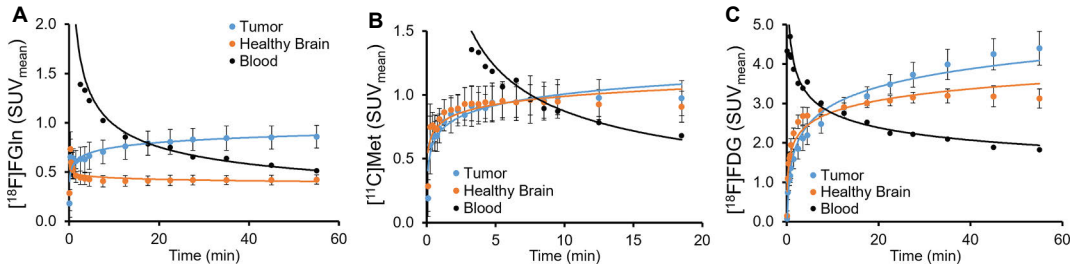

Figure 39. Average PET image time-activity curves for BDIX rats bearing BT4C gliomas. **A** [^{18}F]FGln (n = 13). **B** [^{11}C]Met (n = 12). **C** [^{18}F]FDG (n = 7). Blood standard deviation bars omitted for clarity.

Examining the salivary gland region of [^{11}C]Met in PET images (Figure 40) confirmed high salivary gland uptake in the PET images and that the radiopharmaceutical was functioning similarly to native methionine (Buus *et al.*, 2004).

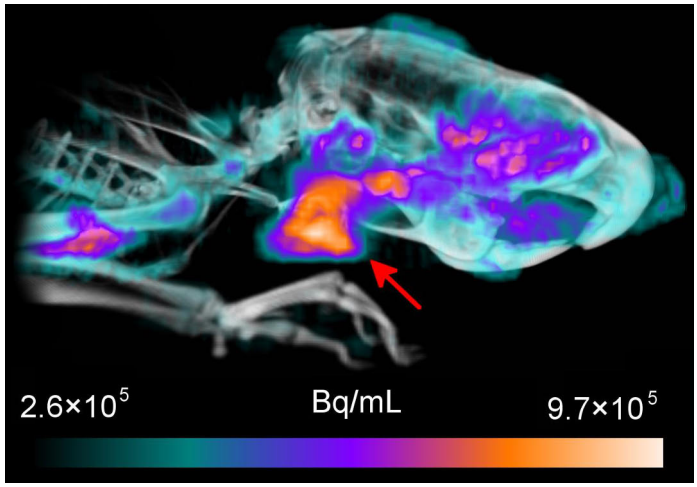

Figure 40. *In vivo* [^{11}C]Met PET/CT 3D-fusion image maximum intensity lateral view of BDIX rat head and neck region (time-weighted mean PET from 5-20 minutes) with high uptake in the salivary gland region pointed out by red arrow.

5.3.2 Camera Comparisons

The BDIX subjects bearing BT4C gliomas imaged with separate camera systems displayed remarkably similar TBR values despite potential intra-subject variability (Figure 41, left). The only noticeable difference in TBR_{peak} between camera systems was with [^{18}F]FGln, though the difference was found to not be statistically significant ($p > 0.25$) when assessed with an unpaired Student's t-test. Overall standard deviation of TBR_{peak} values was consistently lower for the Molecubes' camera system versus that of the Inveon. When data from both camera systems was pooled together, time-activity curve TBR values (Figure 41, right) had low deviation for all radiopharmaceuticals, which is especially visible in the [^{18}F]FDG data.

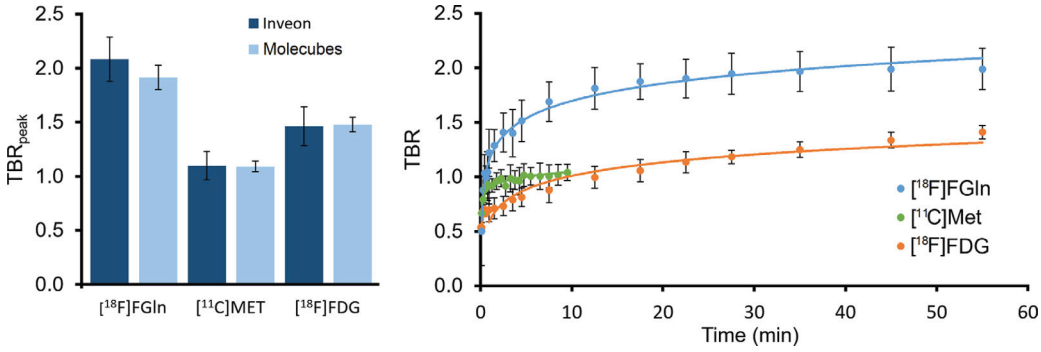

Figure 41. Left: TBR_{peak} comparisons of BT4C gliomas in BDIX rats between camera systems and multiple radiopharmaceuticals. Right: average TBRs curves over time.

Visual comparisons in camera capabilities were also exported to examine the qualitative differences in system capabilities. The tri-cubic visual interpolations (Figure 42, A and B) are remarkably similar when the colour scale is adequately adjusted relative to the histogram despite large differences in output image voxel size (Inveon: 0.78 . 0.78 . 0.80 mm, Molecubes: 0.4 . 0.4 . 0.4 mm), which are visible in nearest-neighbour visual interpolations (Figure 42, C and D).

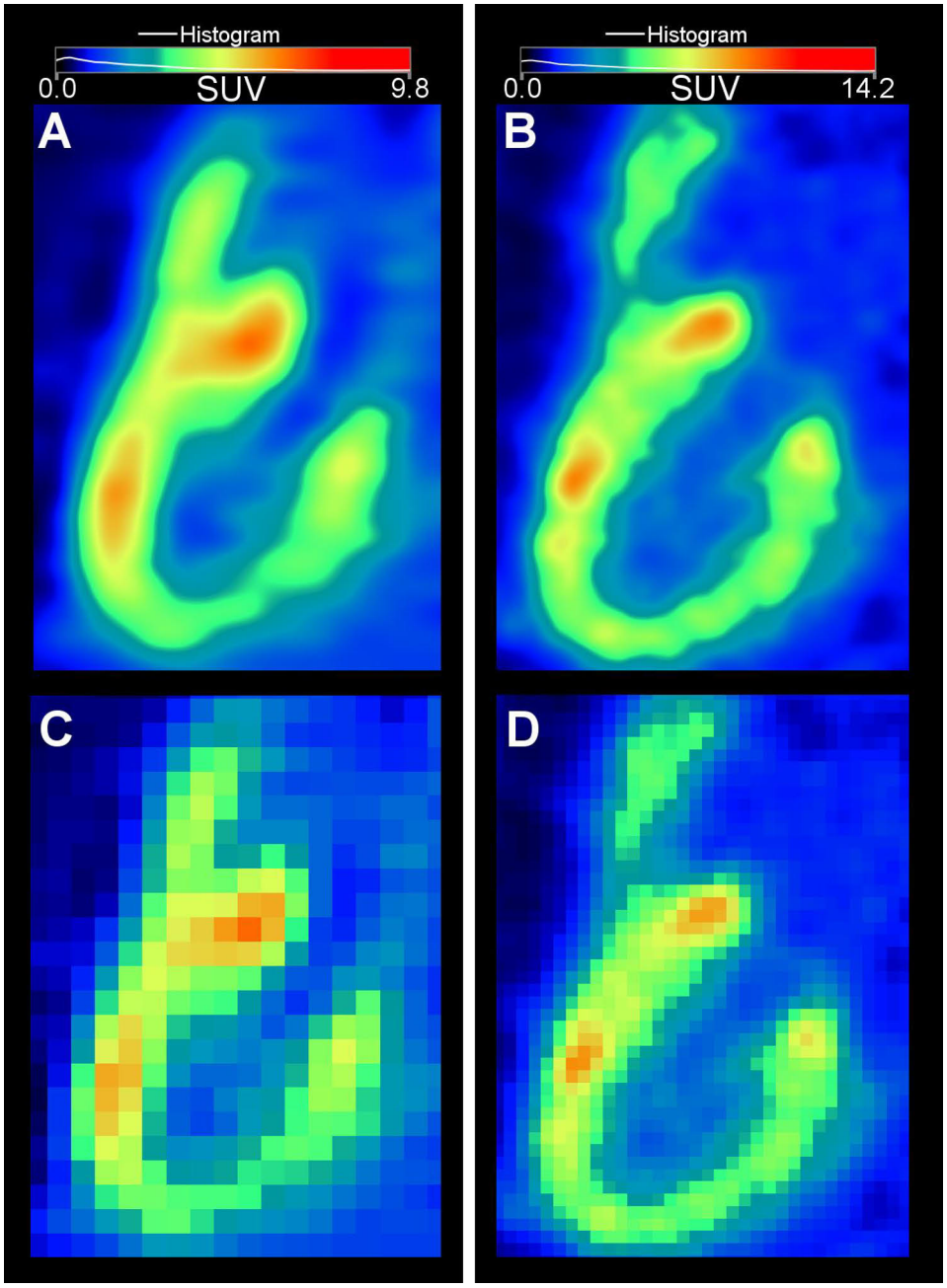

Figure 42. Sample comparison coronal slice of a coronal [^{18}F]FDG PET imaged BDIX rat heart of time-weighted means from 20-60 min post radiopharmaceutical injection. Left, **A** and **C**: Inveon small animal PET/CT system, subject injected with 23.7 MBq. Right, **B** and **D**: Molecubes β-cube PET system, subject injected with 7.8 MBq. Interpolations, **A** and **B**: tri-cubic. **C** and **D**: nearest neighbour.

5.3.3 [^{18}F]FGln Stability in Rats

In vivo stability studies of [^{18}F]FGln in rats combined multiple bioavailable fraction assays to produce an overall bioavailable fraction of total blood radioactivity plot (Figure 43). No significant differences were found between male and female populations so the data was pooled and approximated with the well-fitting curve in Equation 6 which, when multiplied by the injected radiopharmaceutical purity, outputs the overall bioavailable fraction of [^{18}F]FGln for an input time in minutes. After 60 minutes post radiopharmaceutical injection, the bioavailable [^{18}F]FGln fraction had dropped to 28.1% ± 2.7 of the whole blood radioactivity.

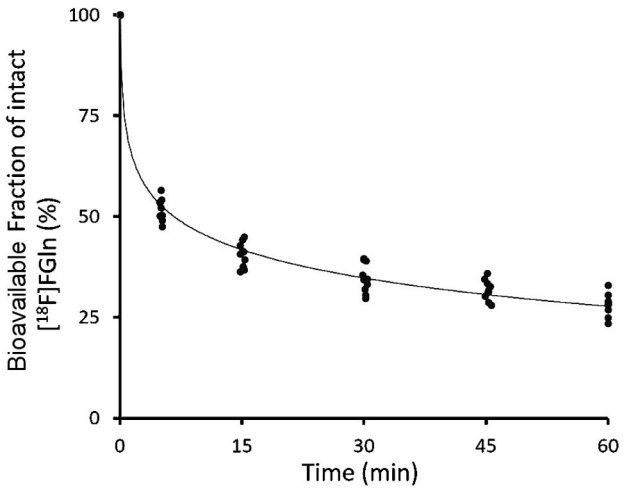

Figure 43. Bioavailable fraction of intact [^{18}F]FGln of whole blood radioactivity with respect to time in healthy 3-month-old BDIX male (n = 5) and female (n = 5) rats.

$$[^{18}F]FGln\ Intact\ Fraction\ (t) = (-0.101)\ln(t) + 0.692 \qquad R^2 = 0.9887$$

Equation 6. Bioavailable fraction of [^{18}F]FGln of whole blood radioactivity where t = post injection time in minutes.

5.3.4 Modelling in Rats

The multiple pharmacokinetic models that were applied to the mouse PET image data (5.2.3) were also applied to rat data (uncorrected and corrected blood inputs also used via Equation 6). The Logan plot data (sample in Figure 44) with corrected blood inputs revealed average (n = 13) distribution volumes of 4.00 ± 1.96 and 1.72 ± 0.66

for glioma and healthy ROIs respectively. When comparing reversible (*e.g.* Logan) and reversible uptake models (*e.g.* Patlak, summary of data in Table 4) only a (relatively) small discrepancy of 0.4 to 8-fold difference (depending on input data) was observed suggesting that while reversible uptake is the main mode of transport, that irreversible uptake still plays a significant role in [^{18}F]FGln uptake in tumour tissue.

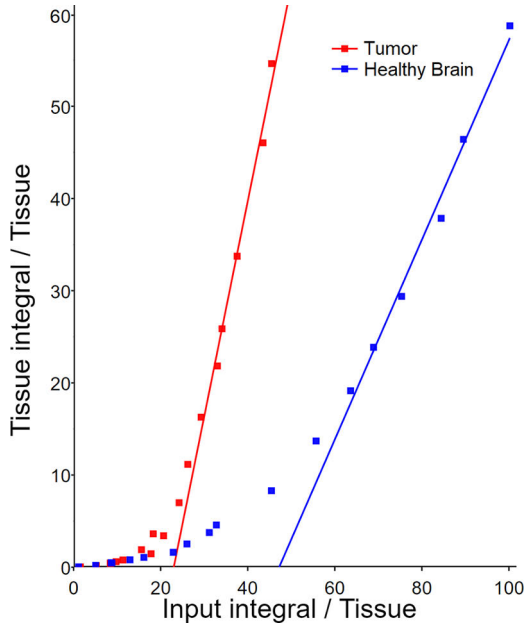

Figure 44. Sample Logan plot dervied from [^{18}F]FGln PET imaging tissue uptake with population-based bioavailable fraction of whole blood radioactivity used as an input.

Table 4. Patlak plot (irreversible uptake model) [^{18}F]FGln result summary for arterial blood, and bioavailable plasma fraction of arterial blood used as inputs.

Region of interest	K_i (AB)	Ic (AB)	r (AB)	K_i (FP)	Ic (FP)	r (FP)
Tumour (n = 13)	0.011 ± 0.004	0.676 ± 0.221	0.962 ± 0.066	0.023 ± 0.006	0.823 ± 0.376	0.993 ± 0.009
Healthy brain (n = 13)	0.005 ± 0.003	0.376 ± 0.114	0.949 ± 0.093	0.011 ± 0.004	0.495 ± 0.195	0.990 ± 0.018

AB; arterial blood radioactivity used as input, *FP*; unbound plasma radioactivity assayed for parent tracer purity (free parent) used as input. K_i = net influx rate (min^{-1}), *Ic* = y intercept.

5.3.5 *Ex Vivo*

Biodistribution results (Figure 45) displayed high uptake in the kidneys as well as in digestion-related organs such as the pancreas and liver. Considerable bone uptake was also noted in both the skull and femur (bone + marrow).

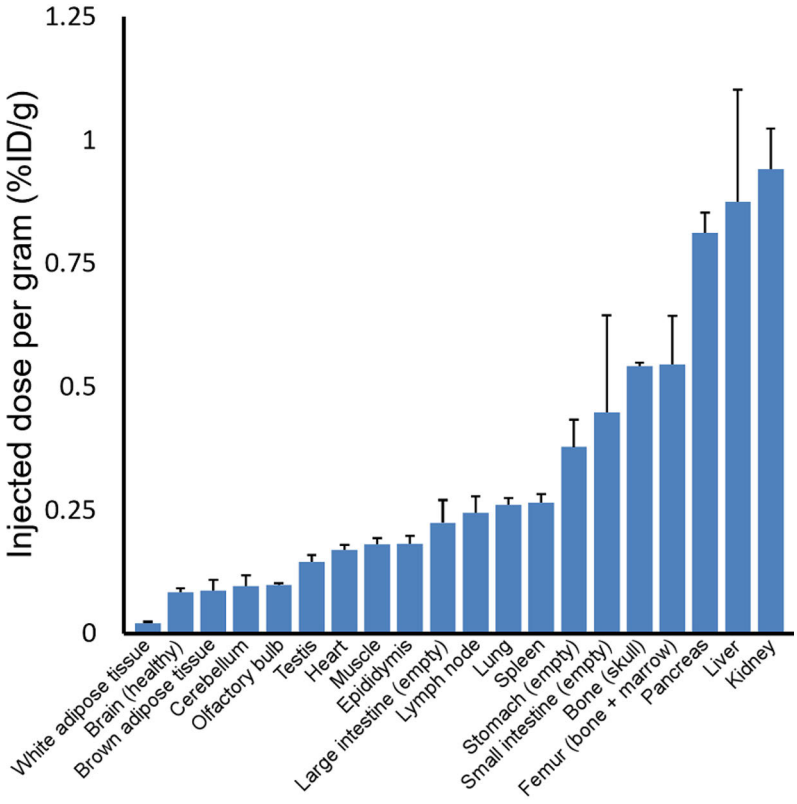

Figure 45. *Ex vivo* average (n = 5) [^{18}F]FGln tissue biodistribution in BDIX rats injected with 24.5 MBq ± 8.7.

Histology (example in Figure 46, top) demonstrated a lack of central tumour necrosis in all 190 sections analysed despite lost [^{18}F]FDG slides. The autoradiography also confirmed PET image results for all radiopharmaceuticals; good tumour delineation for [^{18}F]FGln, a lack of tumour uptake for [^{11}C]Met and a shell-like uptake distribution in [^{18}F]FDG (Figure 38, D). The TBR values for each radiopharmaceutical's set of slides is summarized on Table 5 and show a 33% increase in TBR for [^{18}F]FGln when compared to [^{18}F]FDG.

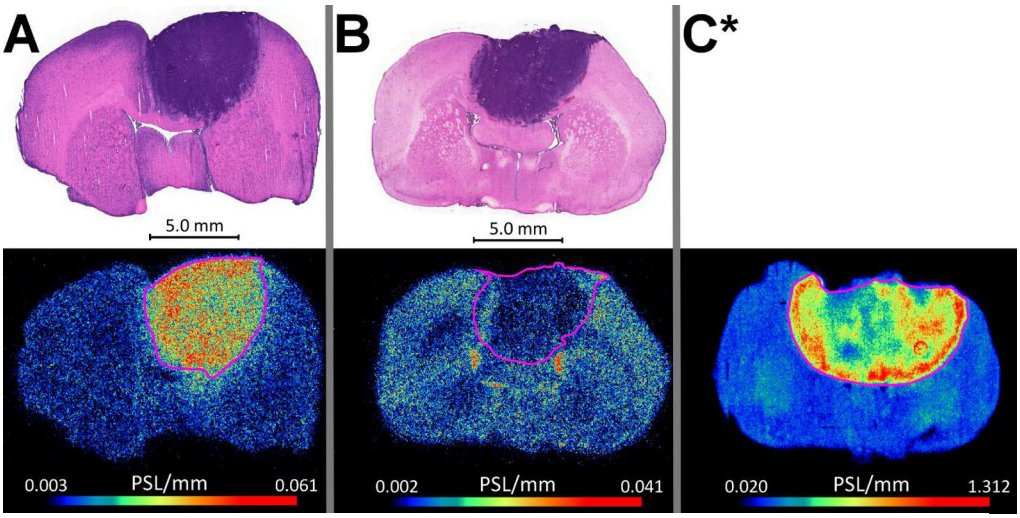

Figure 46. Image array of 20 µm thick e*x vivo* cryosections for histological comparison. Upper row containing H&E stained sections and bottom row containing autoradiographs of the same sections exposed for 2-3 times the corresponding radionuclide's physical half-life. **A** [^{18}F]FGln. **B** [^{11}C]Met. **C** [^{18}F]FDG.

*Unfortunately, the corresponding sections were lost after scanning the autoradiographs.

Table 5. Autoradiography analysis result summary.

Radiopharmaceutical	Tumour-to-healthy brain uptake ratio	n (slices)
[^{18}F]FGln	4.07 ± 0.49	143
[^{11}C]Met	1.14 ± 0.41	47
[^{18}F]FDG	2.93 ± 0.57	30

5.4 [^{18}F]FOL Studies

5.4.1 PET Imaging

Tumour regions delineated via contrast-enhanced T1-weighted MRI (encircled in magenta, Figure 47, top) demonstrated clear uptake in PET images (Figure 47, bottom) with [^{18}F]FOL having improved contrast between tumour and brain tissue over [^{18}F]FDG ((Figure 47, A versus B respectively). When examining the TBR values for both radiopharmaceutical groups over the duration of the study (Figure 48, A) the TBR for [^{18}F]FOL imaged subjects increased over the duration of the study reaching 5.7 ± 1.0 (n = 5, day 32) versus the TBR for [^{18}F]FDG imaged subjects that remained consistent at 1.6 ± 0.1 (n = 9, all time points). Sample 16-day time point dynamic 120-minutes image of [^{18}F]FOL (Figure 48, B) indicated that the optimal imaging window with respect to increased contrast between tumour and brain regions was between 30 and 70 minutes post radiopharmaceutical injection.

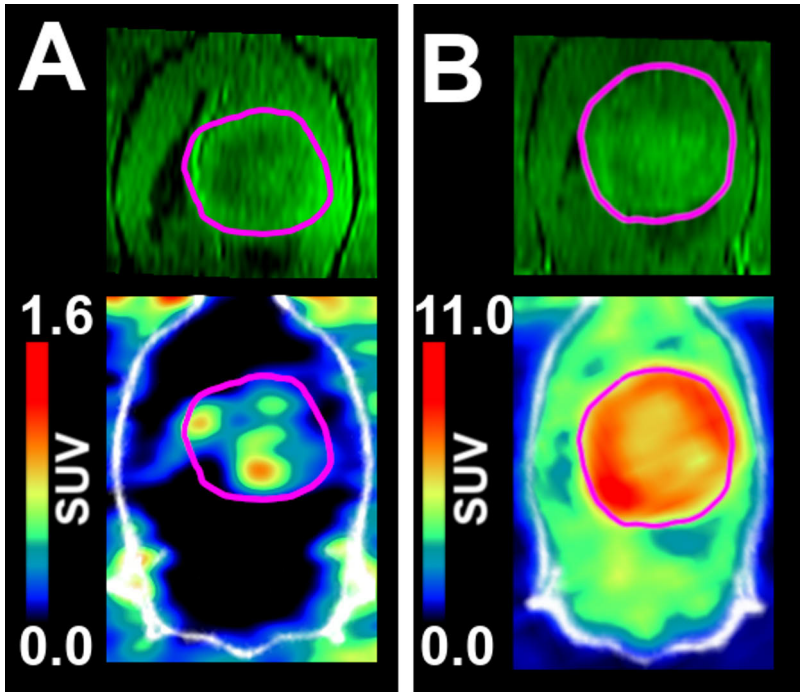

Figure 47. Sample multimodal *in vivo* coronal plane image array of two BDIX rat subject's skull and brain region 32 days after grafting BT4C glioma cells (outlined in magenta). Top: Contrast-enhanced T1-weighted MRI, Bottom: PET/CT. **A** time-weighted mean of frames from 45-65 minutes post injection of 40.2 MBq [^{18}F]FGln, **B** time-weighted mean of frames from 45-65 minutes post injection of 30.7 MBq [^{18}F]FDG.

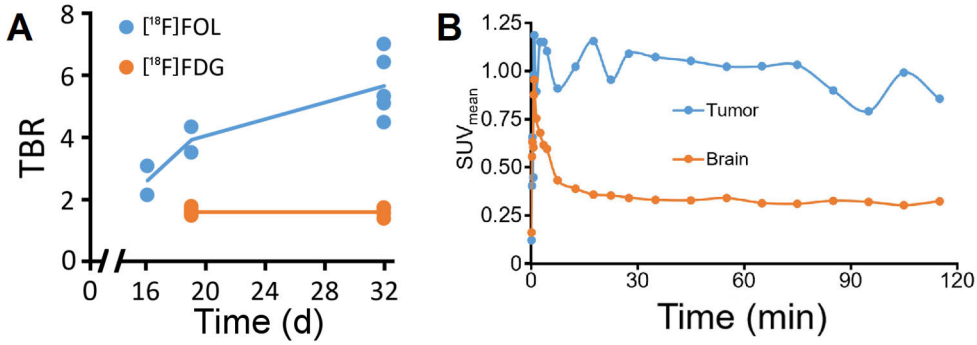

Figure 48. **A** PET image TBR at multiple time points over the course of the 32 day study. **B** Demonstrative time-activity curve for a 120-minute dynamic [^{18}F]FOL PET imaged subject at 16 days post tumor cells grafting.

5.4.2 *Ex Vivo* Studies

The *ex vivo* biodistribution of [^{18}F]FOL in BDIX rats after 70 minutes post radiopharmaceutical injection (Figure 49) demonstrated the highest uptake in the kidneys and lymph nodes and the rest of the overall biodistribution agrees with literature understanding of native folate. Examining the overall lower values in nearly all categories for [^{18}F]FOL versus [^{18}F]FDG suggests a lower relative amount of radiopharmaceutical retention is occurring with [^{18}F]FOL.

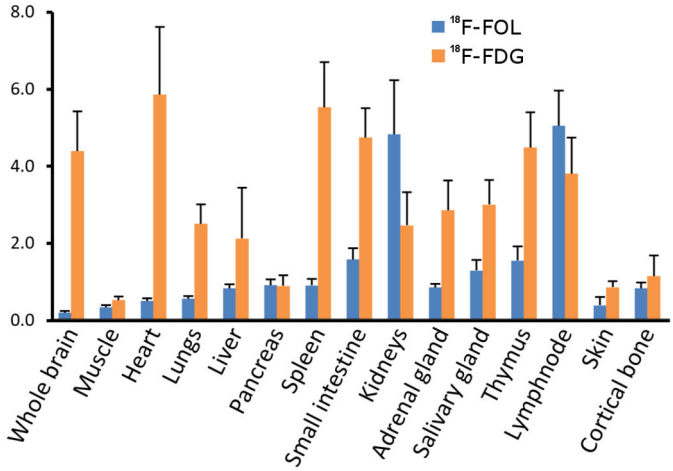

Figure 49. Average BDIX rat bearing BT4C gliomas grafted 32 days prior *ex vivo* biodistribution 70 minutes post radiopharmaceutical injection of 39.8 MBq ± 0.6 (n = 5) [^{18}F]FGln and 30.1 MBq ± 0.3 (n = 4) [^{18}F]FDG.

Autoradiography of cryosections of the dissected tumour-bearing brains immediately after PET (Figure 50) demonstrated extremely high contrast between tumour and brain tissue for [^{18}F]FOL. Average TBR values for the [^{18}F]FOL sections was 116.1 ± 26.9 (n = 4 subjects, 36 sections) while [^{18}F]FDG was 2.9 ± 0.6 (n = 3 subjects, 27 sections).

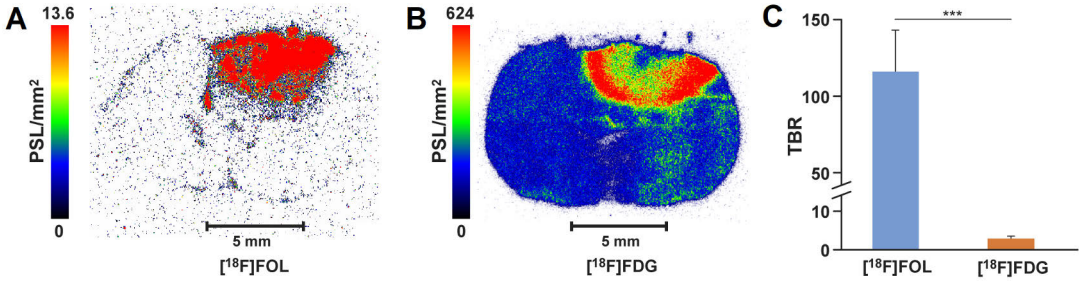

Figure 50. Autoradiographs of BDIX rat brains bearing BT4C gliomas, which were sacrificed 70 minutes after radiopharmaceutical injection of 39.8 MBq of [^{18}F]FOL and 26.5 MBq [^{18}F]FDG and exposed for 3 hours. Average TBR for [^{18}F]FOL (n = 4 subjects, 36 sections) was 116.1 ± 26.9 while [^{18}F]FDG (n = 3 subjects, 27 sections) was 2.9 ± 0.6. *** p value < 0.005.

5.4.3 *In Vitro* Binding and Blocking

The *in vitro* binding studies for [^{18}F]FOL in BDIX rat brain cryosections bearing BT4C gliomas were successful and blocking with a co-incubation of 100-fold molar excess of folate-glucosamine showed very low [^{18}F]FOL binding in tissue (Figure 51).

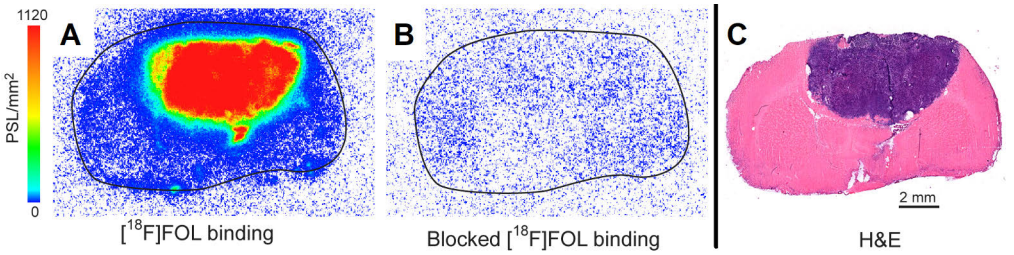

Figure 51. Representative [^{18}F]FOL binding and blocking assay cryosections. **A** [^{18}F]FOL binding. **B** blocking with 100-fold molar excess folate glucosamine. **C** H&E stained adjacent slice to the other preceding slices.

5.4.4 Histology

Consecutive cryosections of BDIX rat brains bearing BT4C gliomas were stained and incubated with a multiple receptor-specific immunofluorescence and immunohistochemical stains revealing increased FR-α signal in tumour tissue with present but much lower signal in the rest of the brain (Figure 52, A). Signal from the CD68 immunofluorescence specific to activated macrophages/microglia also showed a similar trend. The increase. Immunohistochemical FR-α staining confirmed these findings with similar uptake distribution (Figure 52, B). A third immunofluorescence staining sensitive to FR-β on activated macrophages produced a signal increase on the interior tumour periphery (Figure 52, C)

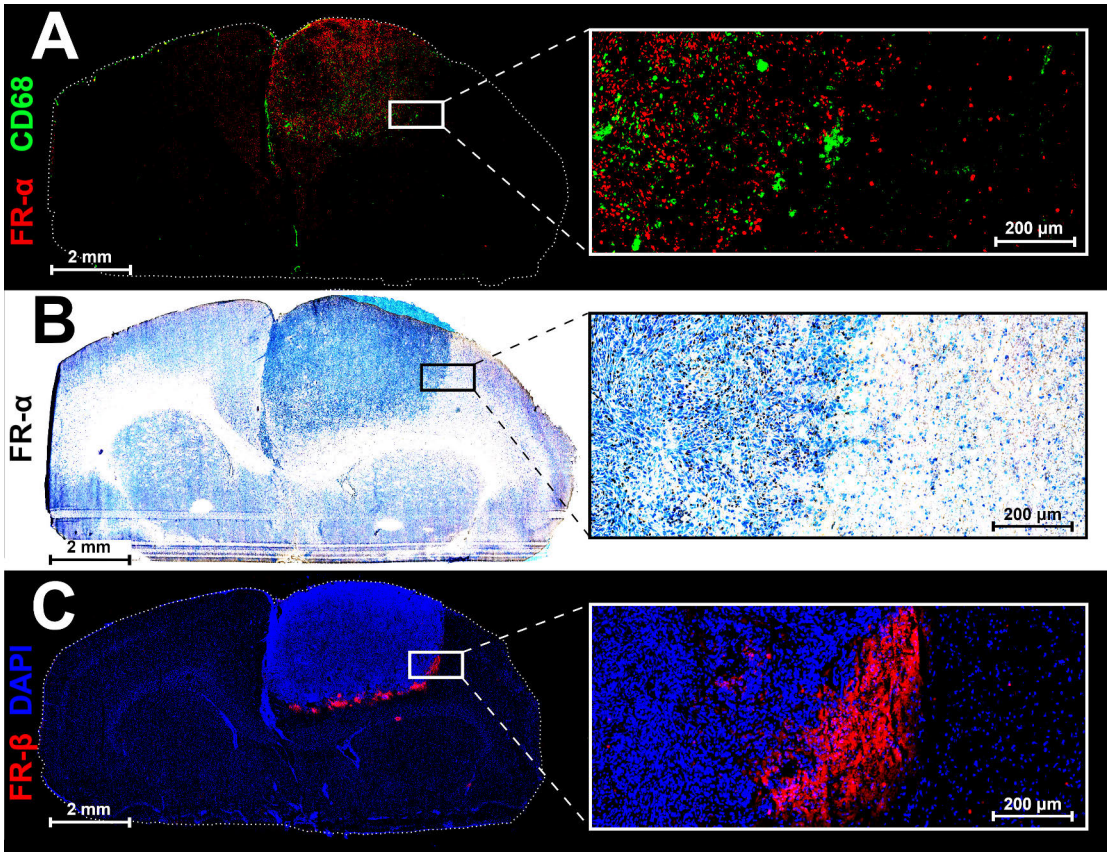

Figure 52. Representative immunostaining of consecutive 8 µm cryosections of a BDIX rat brain bearing a BT4C glioma and zoomed in highlighted regions. **A** Double immunofluorescence staining for FR-α and CD68. **B** Immunohistochemical staining for FR-α. **C** Immunofluorescence staining for FR-β including DAPI nuclei stain for positional orientation.

Histology results from human patient derived gliomas revealed similar findings to rat brain cryosections though with a considerably higher degree of signal heterogeneity (Figure 53, A). Areas assayed for FR-β ranged from being completely absent, variable as a gradient, to expressing very high signal. Activated macrophages/microglia relate to signals with CD68 staining and followed a similar trend. Signals from FR-α detection were mostly very high in tumour tissue but varied in signal intensity. Healthy brain sections (Figure 53, B) were absent for FR-β and showed extremely low FR-α and CD68 signal.

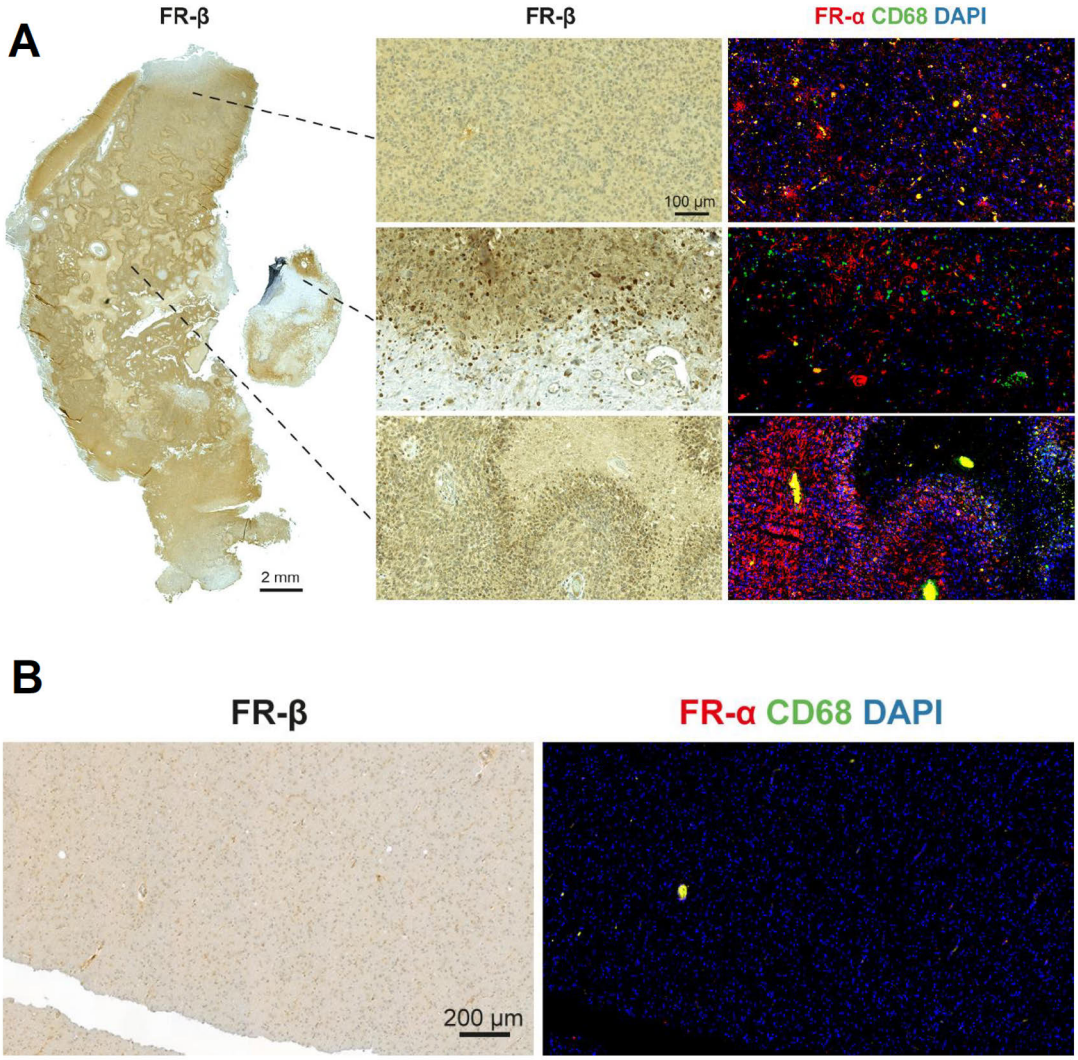

Figure 53. Example human immunostaining of formalin-fixed paraffin-embedded samples. **A** Patient glioma sample obtained during surgery. **B** Healthy brain cortex sample obtained post-mortem.

6 Discussion

6.1 General

Glioma development in the brain is particularly devastating due to a combination of the potential aggressiveness of the tumours and the delicate nature of the brain. For gliomas that are derived from the cells, which make up part of the nutrient transfer network of the brain, such as astrocytomas, all the potential building material to sustain rapid proliferation are reachable with ease. As glioblastoma hold many genetic and pathological similarities to astrocytomas as they often have the same access and genes required to also take advantage of this network. Other types of gliomas, while less common, are not necessarily comparatively insignificant either. When growth rates of any glioma become increased in an already dense zone of soft tissue, the rapid expansion of new cells can tear the dense interconnected microvasculature leaking blood and, most importantly, more nutrients to sustain proliferation. This leaking is the primary method of how MRI contrast-enhancing agents aid in imaging gliomas, though they only grant a snapshot of what the current boundaries may be. Without a method to characterize and quantify the biological or biochemical properties of the glioma, the treatment planning for the patient may be missing key important data.

To complicate things further, the infiltrative nature of glioblastoma in humans is very often significantly present with estimates ranging as high as 80-100% from surgically sampled regions displaying localized oedema and no MRI contrast enhancement (Matsuo *et al.*, 2012). These infiltrative regions are not always highlighted in contrast-enhanced T1-MRI and due to their extensive infiltrative nature, form an ambiguous tumour boundary. Because of this, GBI is often classified as a whole-brain disease (Agarwal *et al.*, 2011).

> *I.e., where does the glioblastoma boundary truly end when it often extends its insidious tendrils outwards in a thin root-like network of cells?*

The realization of this factor brings forwards a critique of this work:

Of what significance do the "relatively" non-invasive singular-mass BT3 and BT4C glioblastoma models have to the human disease?

The BT3 cell line was derived from human patient cells and despite being xenografted into a mouse model, are inherently relevant to human tumours being human cells. The BT4C cell line was derived from rats and exhibits many similar biochemical characteristics to gliomas in humans. They are classified as having an infiltrative nature while still forming a well-defined non-diffuse mass (Wirth et al 2012). The total rat brain volume is, after all, quite small and the tumour growth window is only a few weeks before the final imaging due to subject health concerns. Utilizing an animal model with a larger brain the size allowing for a longer tumour growth duration may have improved the relevance, though for practical reasons murine models were employed.

With the small size of the tumours (roughly 2 and 5 mm maximally in diameter for the mice and rat models respectively) they are already so near the preclinical PET camera spatial resolution limits (~1 mm) that a highly invasive model would not be nearly as conclusive to quantify in terms of radiopharmaceutical uptake. Furthermore, the inconsistent nature of a more diffuse model without a defined mass that can extend seemingly randomly in nearly any direction is practically far less consistent in the way it develops. With these micro-invasive disease characteristics in mind, the necessity of a low background signal to detect small increases in radiopharmaceutical uptake becomes even more apparent. Simply put, the development of non-glucose-based radiopharmaceuticals is an important pathway towards improving glioma detection and PET imaging.

When considering the already low survival rate of patients who develop gliomas, the importance of improving patient outcomes is obvious. Although treatment needs to be also developed alongside non-invasive *in vivo* detection and biological characterization, the latter is a very important first step. Treatment planning cannot effectively move forward without accurate imaging and missing information such as a newly developing small lesion can be catastrophic. The ability of PET imaging systems to detect, delineate, and characterize tumour biochemical properties is inherently tied to the radiopharmaceutical utilized. Developing and rigorously testing the new and emerging radiopharmaceuticals is a crucial step towards quantifying their imaging abilities. This development and testing requires a wide variety of assays beyond just PET imaging to divulge additional insight into the biodistribution, pharmacokinetics and breakdown of the compounds, and to confirm uptake via a more direct measurement of the dissected tissue. For all of this, animal studies have been used along with human glioma tissue testing when a compound looks promising enough to test for specific radiopharmaceutical-related receptors during an absence of clinically supporting data. Although there are some study

limitations in the works presented, they represent an overall positive outlook on the capabilities of both [^{18}F]FGln and [^{18}F]FOL for *in vivo* PET imaging gliomas.

6.2 [^{18}]FGln Studies

Study I and Study II demonstrated a relatively reliable reproduction of the [^{18}F]FGln synthesis assuming great care was taken to prevent additional moisture or water from degrading the precursor and causing the synthesis to fail. The [^{18}F]FGln compound was synthesized in a large enough amount to allow for imaging multiple animal subjects (together in series and simultaneously in parallel), which would be also enough for future human patient imaging when examining the injected radioactivity levels in ongoing clinical trials (Trial ID: NCT01697930). The safe and effective use of the imaging radiopharmaceutical [^{18}F]FGln for PET imaging gliomas in both mice and rat models was also demonstrated. The intracranial orthotopic tumours were particularly imaged effectively when comparing to the parallel studies with [^{18}F]FDG and [^{11}C]Met in rats. The ability to differentiate between tumour and brain tissue can be effectively measured in each subject as a ratio in the form of TBR, which was 1.4-fold higher for [^{18}F]FGln than [^{18}F]FDG and 2-fold higher than [^{11}C]Met.

Qualitatively, the subcutaneous PET images demonstrate reasonable tumour uptake in contrast with the contralateral muscle tissue, but the most significant PET image quality is found with the intracranial models. Here, with the low basal brain uptake, tumour tissue is very easily distinguished from brain tissue. The overall low [^{18}F]FGln brain uptake can be confusing upon initial image analysis inspection, especially if more familiar with a high brain-uptake compound such as [^{18}F]FDG. When compressing the visual colour range to suit the range of the tumour and brain region specifically, the tumour practically leaps out of screen. For a tumour lesion in a small animal model that is so near the spatial resolution of the camera system this is quite a feat and the *ex vivo* autoradiography supported this even more so. Autoradiography results confirmed this high contrast difference between tumour and brain tissue to an average TBR of approximately 4 exceeding [^{18}F]FDG and [^{11}C]Met by 1.3 and 3.8-fold respectively.

Admittedly, the lack of [^{11}C]Met uptake in glioma tissue presented a bit of a setback due to it having widespread use in European PET imaging of human patients with gliomas. It is uncertain as to exactly why this model was not successful in mimicking the success observed in humans and most theories proposed here would be purely speculative. It is interesting to note that there are not any published studies in mice or rats, which have successfully used [^{11}C]Met to image intracranial gliomas so it is possible that this specific model or species isn't compatible with this radiopharmaceutical.

The *ex vivo* biodistribution of [^{18}F]FGln was found to be as expected for an amino-acid-based radiopharmaceutical; high uptake in digestion-related tissues such as the pancreas and intestines, kidney and liver uptake common to excretion of compounds not accumulating in target tissue common to intravenously-injected compounds, and overall low brain uptake. Notable uptake is found also in the bone tissue, which is classically indicative of free[^{18}F]F^{-} which, in this case would be released from defluorination of the radiopharmaceutical (Czernin, Satyamurthy and Schiepers, 2010; Broos *et al.*, 2018). Here lies the clear shortcoming with this radiopharmaceutical, which likely stems from its structural resemblance to native glutamine. Due to the importance of glutamine processing, whether into cellular energy, into another amino acid or even into a protein chain, nearly countless different biological systems are in place to interact with it and consequently the [^{18}F]FGln radiopharmaceutical. This allows the free travel of [^{18}F]FGln along similar import proteins and potentially along the same chemical gradients, which is the mechanism behind its cellular accumulation in gliomas, but also includes the unfortunate aspect of metabolism. This pathway responsible for defluorination has been characterized and it occurs as an unintended side reaction. A γ-elimination of the [^{18}F] occurs as (2*S*, 4*R*)-4[^{18}F]fluoroglutamate is deaminated into α-ketoglutarate (making alanine in the process) releasing the free fluoride, which is quickly absorbed by osseous tissue (Cooper *et al.*, 2012).

This unfortunate coincidence, that the alanine aminotransferase protein just happens to interact with [^{18}F]FGln in a manner that causes the cleavage of the fluorine bond, has likely set back its widespread adoption for detecting gliomas in clinic. There has been some developments into altering the structure of [^{18}F]FGln with the goal to prevent this defluorination by incorporating it into a short protein chain (Zha *et al.*, 2018), adding an alkyl chain extension to move the fluorine-18 farther from the active site (Wu *et al.*, 2014), adding a boron-trifluoride next to the terminal amine (Li *et al.*, 2018), but all of these modifications have thus far partially impeded the cellular transport. Carbon-11-labelled glutamine has also been synthesized and used to detect different subcutaneous tumours in mice though the authors cite that the fluorine-18 analogues may be more practically convenient (Qu *et al.*, 2012) and few investigations have been published since.

Despite these metabolic shortcomings, [^{18}F]FGln may still see use in clinics as clinical trials head further towards completion. In terms of practical considerations, the radiopharmaceutical can be produced relatively cheaply and in large enough radioactivity quantities to image multiple subjects with one batch. The overall dosimetry reported by Dunphy *et al* in 2018 demonstrate comparable radiation burden for patients with existing clinical radiopharmaceuticals for cancer imaging and there are no reported toxic side effects of the compound. In terms of end-result

image quality, there are many positive and convenient factors regarding high tumour to brain uptake ratio that may end up overshadowing the metabolic drawbacks.

6.2.1 *In Vivo* Imaging Camera Comparisons

In Study II, imaging was performed in parallel with two separate camera systems, the Inveon Multimodality small animal PET/CT and the Molecubes X-cube and β-cube. This parallel setup made it possible to reduce the number of total imaging days and therefore synthesized batches of radiopharmaceutical while also making it possible to compare the results from both systems. Although this type of comparison is usually done with an imaging phantom (a multi-chambered fillable vessel inside which you can put a known amount of radioactivity to reduce intra-subject variability) and a true *in vivo* comparison of the systems would be most accurate by imaging the same subject in both systems, the resulting data was still quite reassuring. The two cameras have been compared in a phantom study previously and demonstrated some appreciable differences in parameters such as recovery coefficients and spillover amounts (Liang *et al.*, 2020; Teuho *et al.*, 2020b). Study II, however, is the first study to compare the two cameras in an *in vivo* investigation and, rather than examining the more technical parameters, focused on the end-result imaging data.

The BT4C tumour model used was both successful and consistent in its development of tumours in the BDIX rats and the results do show some remarkable consistency. There were some differences in camera performance that can barely be teased out of the noise in the data; perhaps most obviously, the reduction in standard deviation variability in the TBRs (Figure 41, left). It is unclear what the reasoning would be, though it is possible to speculate that it is a reduction of noise stemming from the more sensitive photomultipliers and detection system of the Molecubes, which forces the user to lower the injected radioactivity. Interestingly, the average TBR (despite being different subjects) is remarkably similar for both [^{11}C]Met and [^{18}F]FDG yet very slightly (statistically insignificantly) different for [^{18}F]FGln. The [^{18}F]FGln group contained the greatest number of subjects which, if anything, should have supported a better averaging towards the same value for both cameras but did not. On its own, this discrepancy is quite insignificant and can be easily chalked up to any number of numerous variables, but additional interesting observations in PET image versus autoradiography discrepancies were made (see later 6.3.1). Overall, it was concluded that there was no statistically significant difference in the end-result between the two camera systems which suggests that utilizing both in parallel for future studies may be a feasible way to improve the workflow throughput on a single imaging day. For particularly difficult to synthesize radiopharmaceuticals which

may have a low yield, running multiple different cameras could be a way to get the most data out of the experiment.

6.3 [^{18}F]FOL Studies

In Study III, [^{18}F]FOL was synthesized at a remarkably high radiochemical purity and this study was the first to test a fluorine-18-labelled folate of any type to image a brain tumour. This previously unexplored PET imaging niche demonstrated a very high level of contrast between tumour and brain tissue. Even with the low overall brain uptake (roughly 25-fold less than [^{18}F]FDG), [^{18}F]FOL PET image TBR levels reached up to 8.5 (roughly 3.5-fold higher than [^{18}F]FDG). Although folate is required in the brain for normal function at all stages of life, its low consumption (relative to glucose) in the developed brain lacks the requirement for a strong increase in BBB transport protein production. While it is likely that the entry of chelator-conjugated folate into the brain mostly by BBB leaking, the spatial distribution of [^{18}F]FOL did not perfectly match the Dotarem® MRI contrast-enhanced images. Unfortunately, the lower resolution of the PET camera system does not allow for a concrete conclusion with such a small imaging target. If the ring-like (or shell-like distribution in 3-dimensions) signal in the MRI demonstrates the primary entry method of [^{18}F]FOL, the later PET image frames and autoradiography may support the notion that the radiopharmaceutical is transported to tumour tissue not adjacent to the tumour periphery. The ring shape distribution was, perhaps surprisingly, seen in the [^{18}F]FDG PET images (and confirmed in autoradiography) which is odd considering the ease at which glucose is passed through the BBB in non-disrupted zones. It was originally suspected that central tumour necrosis was the cause, though this was not observed in any subject's brain histology. It is possible that these regions were hypoxic due to a lack of blood flow, which is a common occurrence, and that the lack of hypoxia did not cross the threshold into necrosis. When critiquing the comparatively lower ability of [^{18}F]FOL to pass into the brain via other means than BBB disruption, it is remarkable that its distribution within tumour tissue does not resemble this expected ring-like shape. With this in mind, it is possible to conclude that the reversible nature of [^{18}F]FOL may be what allows for the dispersal of the radiopharmaceutical to tissue not adjacent to the BBB disrupted zone.

The autoradiography presented a very interesting result with respect to how much higher the TBRs were for [^{18}F]FOL than what was detected in the PET images. The TBR values reported here were over 10-fold higher than the average PET image and in one outlying case nearly exceeded 20-fold. These discrepancies, also observed to a lesser degree in [^{18}F]FGln imaging, are discussed together in the following subsection 6.3.1.

The *ex vivo* biodistribution of [^{18}F]FOL was found to be in line with general scientific consensus of folate metabolism and excretion of intravenously administered folate. Similar uptake in the kidneys and lymph nodes as [^{18}F]FDG, though with noticeably lower uptake in the rest of the organs assayed. As expected from PET image data, there was considerably low overall brain uptake. The bone uptake was also low indicating that defluorination is not playing a significant role in the radiopharmaceutical's metabolism *in vivo*.

The *in vitro* binding and blocking studies demonstrated that folate-glucosamine, a known competitor for the folate receptors, was interfering with [^{18}F]FOL uptake. This grants some insight into whether or not binding of [^{18}F]FOL is via the same receptors as a native folate, though with fixed tissues the process is more superficial and the folate cannot be internalized via endocytosis. This competitive blocking using excess folate glucosamine provides one more additional piece of evidence towards the suspicion that, despite chemical additions to the basic folate structure, [^{18}F]FOL is still transported through the same pathways as other folates. The lack of examining the *in vivo* (or live tumour cell culture) blocking by intravenously injecting folate-glucosamine before [^{18}F]FOL is a limitation of this work and could have likely shed additional insight into the true competitive blocking value. It has been shown previously, however that the binding of [^{18}F]FOL to atherosclerotic plaques is blocked *in vivo* via this method (Silvola *et al.*, 2018).

Immunostaining of the rat brain cryosections revealed direct evidence that FR-α is present in much higher levels in tumour tissue than in the rest of the brain. Although folate can be transported through multiple pathways and receptors, this identifies FR-α as potentially being a large contributor to the heightened uptake in tumour tissue. Although folate can be imported and exported from cells, a very large increase in folate-specific transporters in tumour tissue would both increase the net transport into tumours while simultaneously releasing some to other tissues. The released folate would then still be more likely to go back to another tumour cell due to this increased receptor expression allowing for [^{18}F]FOL tumour distribution to exceed BBB leaking-based entry zones. In the immunostaining it is also possible to see much more CD68 signal, which binds specifically to activated monocytes such as microglia and macrophages. The FR-β signal, however, is specific only to activated macrophages and was seen on the tumour periphery possibly indicating a regional disruption of the BBB allowing them to migrate into the brain.

The human glioblastoma immunostaining demonstrated perhaps one of the most exciting results of the study showing a similar large increase in FR-α in tumour tissue that was not observed in healthy brain tissues sections. Although the FR-α signal was highly regionally variable, it generally ranged from somewhat high to very high compared to a very low background level in the healthy sections. This evidence provides some interesting potentially clinically relevant insight into the feasibility of

folate-based radiopharmaceuticals for future PET imaging gliomas. It must be kept in mind, however, that glioma morphology is highly heterogenetic both inter and intra-genetically and one major limitation to this study is the low number of patient-derived samples. These results imply that at least some gliomas may be detected and PET imaged accurately with a folate-based radiopharmaceutical. Furthermore, more development and testing into changes which render the compound more permeable through the BBB may prove to be extremely beneficial to improve PET imaging capabilities. Being able to non-invasively detected whether a tumour expresses additional FRs may also discern whether folate-targeting chemotherapy will be beneficial to a specific patient and that no time is wasted with a non-working generalized approach to treatment. The era of personalized medicine continues to creep forward.

6.3.1 PET and Autoradiography Discrepancies

When examining the autoradiography TBRs, the [^{18}F]FDG and [^{11}C]Met values reflect quite accurately what is seen on the PET images, yet the TBR values for [^{18}F]FGln were found to be generally 2-fold higher than what is seen on the PET images. This discrepancy was then later amplified in Study III where the absolute highest TBR in any [^{18}F]FOL PET image subject reached a value of 8, yet in the autoradiography the average [^{18}F]FOL TBR was often over 100. Since the autoradiography is the more direct measurement- the brain is removed, sliced into thin sections, which are then exposed to radiation-sensitive imaging plates after all, it can usually be assumed to be much more accurate. If this is true, and there is over 100-fold more radiopharmaceutical in the tumour tissue versus the other brain tissue, *why wouldn't it show up more accurately on a PET image?* The phenomenon was replicated and observed in custom made anatomically-based 3D-printed phantoms and suggest that it may be a spatial distribution phenomenon inherent to many PET imaging systems (Thus far *unpublished* observations). This misinterpretation occurs when imaging such small regions in already such small subjects when surrounded by a shell of radioactivity distribution. Interestingly, the slight discrepancy in TBR observed between the two PET imaging systems in Study II has also been replicated in this developing phantom model. Though both systems fail wildly to accurately interpret a small very specific spatial distribution geometry related to intracranial gliomas, one just happens to be consistently a few percent less-worse.

6.4 *In Vivo* Stability Assays

Pharmacokinetics: *The study of the fate of a drug in a living organism over time*

To say that the inherent complexities of a living subject with respect to drug metabolism are numerous is quite the understatement. Often, and especially so for naturally occurring metabolic compounds and their analogues, there exist multiple pathways to degradation *in vivo.* In contrast with a closed-system simple chemical reaction, *i.e.,* where compound A splits equally into compounds B and C, extrapolating the speed at which the conversion occurs is often much more multifaceted. In a complex living system there are frequently multiple products that have their own rate of conversion, *i.e.,* A splits into B and C, but also potentially D and E instead or gets converted into A_2, *etc*. If we assume these products may also break down into additional parts, or have molecules added to them, the fractal expanding distribution of different compounds begins to become exponentially complex.

Often, sweeping simplifications (inaccurate assumptions) of a complex *in vivo* system must be made to apply mathematical models to them. While at first, this seems catastrophically erroneous (*and of course, it partly is*), applying the same simplifications to different systems or compounds still allows for some amount of comparison between them if other variables are kept constant.

Knowing something can be better than knowing nothing…

To better understand the use and approach to PET radiopharmaceutical pharmacokinetics studies, one must consider what the data will be used for. For a simple investigation into drug stability *in vivo*, the primary concern revolves around the disappearance of the parent radiopharmaceutical (*i.e.* the originally synthesized) compound from blood circulation.

i.e.: How long does the parent radiopharmaceutical stay circulating in the blood so that it can go to the target tissue?

When investigating more complex pharmacokinetic models in PET images, the data is being applied to rate of radioactivity accumulation/disappearance in some target tissue(s). This becomes quite problematic if, for example a hypothetical radiopharmaceutical [^{18}F]-A breaks down into [^{18}F]-B and both are able to accumulate into the same tissue! It is impossible to tell them apart in a PET image since the fluorine-18-decay signals are the same. You could, however, assume that in earlier imaging time points after radiopharmaceutical injection you are still mostly

(or entirely) parent-compound, but it is characteristically compound-specific and why there is a need to examine radiopharmaceutical stability in the first place. In later time points it might be necessary to assume that [^{18}F]-B is not able to accumulate in target tissue and remove it from your model if you are not able to isolate/synthesize that specific compound for a second parallel metabolic study.

The pharmacokinetic properties are of great interest to the development of novel radiopharmaceuticals since what is initially injected into a subject will very likely change over time. If such a break down happens in minutes, is the new compound the actual compound with promising imaging capabilities? Or is it a metabolite product that is accumulating in the target tissue? If it is the latter, more detailed studies on the safety and utilization of this metabolic compound are necessary.

6.4.1 Practical Approaches

Knowing every detail about the pharmacokinetics of a radiopharmaceutical is always preferred, but time and resources for preclinical studies do not always afford testing everything. Gathering as much information as possible is always the next best thing. For instance, if the identification of multiple metabolic products is not possible, then the simplifying assumption the relatively low amount of metabolites are inert must be made. The most useful and practical perspective for PET-related pharmacokinetic studies may be to simplify the data into components or fractions that make the radiopharmaceutical not bioavailable. Then, at any given time the approximate value for how much of the total blood radioactivity is the parent radiopharmaceutical of interest and how much is not trapped by various means unable to go into the target tissue can be divulged.

The three main components to assay are:

1. Red blood cell (RBC) uptake – These porous cells will readily uptake many small compounds (radiopharmaceuticals included) as they flow through the circulatory system. They also release the compounds and then take them in again reaching an equilibrium. At any given time, the radiopharmaceutical fraction that is inside of red blood cells is not able to cross from the blood into the target tissue directly and thus does not contribute effectively to the equilibrium going from the blood into the target tissue. Measuring the rate of radiopharmaceutical accumulation in red blood cells allows for the deduction of the bioavailable radiopharmaceutical fraction in the plasma.

2. Plasma protein binding – If the radiopharmaceutical becomes stuck to or incorporated into a protein it may still be circulating in the blood but unable to

cross into the target tissue. By precipitating, filtering, or otherwise separating the proteins out of the plasma, it is possible to separate and measure the fractions to discern how much of the plasma radioactivity remains unbound. When the parent radiopharmaceutical is freely floating in the plasma, it is possible for it to cross into the target tissue.

3. Metabolic breakdown and parent-radiopharmaceutical amount – As the metabolic breakdown of the radiopharmaceutical occurs, these radiometabolites may still circulate in the blood. If we assume that they are now in a form that cannot be taken up by the target tissue, or uptake is at some magnitude lower than our parent compound, they can be simplified. In an ideal scenario, the metabolic products are inert and therefore everything that is not the parent radiopharmaceutical can be classified as a non-available fraction. In reality the situation is much more complex as metabolite products may be taken up by the target (or other tissue) or get converted into a more lipophilic form which can then cross the BBB. Metabolism can also happen within the target tissue further complicating what fate the radiopharmaceutical will meet.

Combining all three fractions gives a reasonable estimation of how much of the total circulating whole-blood radioactivity (at a specific time) can be attributed to the parent compound in its "bioavailable" form. If multiple time points are assayed, for example at 5-, 15-, 30-, 45-, and 60-minutes post injection, it is then possible to estimate a curve for the available fraction. This curve can be applied to correct modelling blood input functions (see: 4.4.4 Bioavailable Parent Plasma Free-fraction). For a dynamic 60-minute PET image of the subject, the total blood radioactivity over time can be extracted by selecting voxels within the heart left ventricle cavity. Since 100% of this radioactivity in the blood is not available due to red blood cell uptake, protein binding, and metabolism, by not correcting for these unavailable fractions, the rate at which the parent radiopharmaceutical is accumulating into the target tissue can be severely underreported as present in modelling results in Study II.

6.4.2 [^{18}F]FGln Stability and Modelling

With the sweeping assumptions previously described in 6.4- namely the fact that [^{18}F]FGln breaks down into its fluorinated glutamate analogue and goes through further metabolic break down, the point of divulging mathematical constants to describe the pharmacokinetics seems initially moot. The fluorine-18-labelled glutamate will also go into tissue at its own rate along with its metabolic fragments and free fluorine-18 ions in an already established significantly occurring digestion

process. The relevance of applying these mathematical models lies within the comparability of data that makes the same simplifying assumptions. With this in mind, we felt it prudent to release a large volume of data related to modelling in both Study I and Study II to allow for future comparative analyses ensuring that multiple modelling approaches will have something to compare to. For example, a new change to the chemical structure tested in the same (or similar) animal subjects will have discrete values to compare kinetics to and more definitively say whether they have a quantifiable improvement in uptake rate. The same reasoning can be applied to different variables such as other disease models. Herein lies one of the most useful aspects of PET imaging- its non-invasive quantifiable nature of a complex living system.

7 Summary

The primary goal of this work was to synthesize and test emerging radiopharmaceuticals to *in vivo* PET image gliomas and reinforce or refute their imaging capabilities. Furthermore, it was set out to characterize their pharmacokinetic properties. Lastly, when clinical evidence was absent, it was imperative to seek potential clinically translational relevance to improve the scientific consensus towards the potential radiopharmaceutical use in humans.

The summary of findings in each study are:

Study I [^{18}F]FGln was successfully synthesized and tested for the first time at the Turku PET Centre at a high radiochemical purity and tested in two separate glioma-bearing mouse models finding favourable PET imaging characteristics for detecting and delineating gliomas. Multiple pharmacokinetic modelling assessments provided specific kinetic constants for future quantitative comparative analyses in mice.

Study II [^{18}F]FGln was shown to be an effective radiopharmaceutical for *in vivo* PET imaging gliomas in an orthotopic rat glioma model with at least a 30% increase in TBR when compared with [^{18}F]FDG or [^{11}C]Met. The two PET imaging systems, Inveon small animal PET/CT and the Molecubes (X-cube and β-cube) provided no statistically significant differences with respect to the end-result *in vivo* PET imaging data and thus could be potentially used in parallel together without data issues. Lastly, multiple pharmacokinetic modelling provided additional kinetic constants for quantitative *in vivo* PET studies in rats.

Study III This is the first study to demonstrate that [^{18}F]FOL has good PET imaging characteristics for imaging orthotopic gliomas in rats with a very high TBR. Human glioma samples obtained post-surgery were shown to have a similarly high expression of FR-α as with the rat glioma model. This demonstrates that the FR-α maybe a present and viable target for folate-based therapy and supports the likelihood that gliomas can be detected and characterized by using [^{18}F]FOL or a folate-based radiopharmaceutical.

8 Conclusions

Study I [^{18}F]FGln can be used to safely and effectively PET image human patient-derived gliomas intracranially orthotopically xenografted into mouse brains as well as subcutaneously xenografted gliomas in rats. The primary uptake method of [^{18}F]FGln in soft tissue is via reversible pathways while defluorination is the likely culprit causing irreversible fluorine-18 uptake in osseus tissue.

Study II [^{18}F]FGln can be used to safely and effectively PET image rat tumours orthotopically grafted into rat brains with a higher TBRs than commonly used clinical radiopharmaceuticals [^{18}F]FDG and [^{11}C]Met. The primary uptake method of [^{18}F]FGln in soft tissue was confirmed to be mostly via reversible pathways. The two PET imaging camera systems Inveon small animal PET/CT and the Molecubes (X-cube and β-cube) provided similar end-result data and could be used in parallel.

Study III [^{18}F]FOL was demonstrated for the first time to be a potentially useful PET imaging agent for detecting orthotopic gliomas in rats. The remarkably high TBR values suggest that there is untapped potential in folate-based radiopharmaceuticals for PET imaging gliomas. Examining human patient-derived tissue sample sections showed similar staining profiles with respect to folate receptor expression showing that the same PET imaging ability may be present for human subjects.

Acknowledgements

The nature of PET-related studies in the preclinical (as well as clinical) area are so multi-disciplinary that they are impossible to carry out alone. The amount of help and collaboration I have had to complete all of this work is gargantuan and cannot be adequately expressed in this short text. It has not been solely my co-authors, whom are listed on each article whom contributed to this. Many more have contributed their time an energy both directly and indirectly. Each facility we have used for our research projects often have had their own expert staff, equipment technicians, animal caretakers, custodial staff, software developers, managing directors, and more who are all absolutely needed to accomplish this type of complex intertwined feats of research. My sincerest apologies if you are overlooked in this text. Do know that I appreciate and respect you all greatly. Thank you for all of your help and dedication to the advancement of science!

This work was primarily financially supported by the grants from the State Research Funding of Turku University Hospital, the Finnish Cultural Foundation, the University of Turku Drug Research Doctoral Programme (DRDP), the Jane and Aatos Erkko foundation, and the InFlames Research Flagship. Without all of this financial support, it would have been impossible to dedicate time to carrying out these tasks in an efficient manner and pursue additional projects, so thank you for your support!

My thanks to Dr. Kim Bergström (PhD) and Dr. Kirsi Timonen (MD, PhD) for their thorough review and guidance which undoubtedly made the manuscript better and much more concise. These two are highly respected and established in the field, so, taking time from their undoubtedly busy schedules to review this document has been greatly appreciated. Thank you!

All of the projects that make up this work would have been impossible to carry out without the huge amount of help from Heidi Liljenbäck and Jenni Virta. Heidi, you have committed countless hours towards these projects with respect to developing and creating the nearly all of the animal models tested and Jenni has been nearly just an involved with the process and other animal related handling. It has been, and continues to be, great to know both of you- learning from your skilled abilities and extremely strong work ethic. I have always tried to organize projects to

the best of my abilities though have made some scheduling and planning errors. Instead of being upset, you have always worked with me to ensure things still get done effectively and I have gotten (somewhat) better at organizing things! Included in this line would also be Aaake Honakaniemi who has been instrumental in planning/scheduling camera time along with camera operation and data organizing. My thanks to you all for making up for my early-career organizational shortcomings! To the rest of my manuscript co-authors and collaborators; Drs. Joni Merisaari, Vesa Oikonen, Jukka Westermarck, Semi Helin, Olli Eskola, Petri Elo, Jarmo Teuho, Kerttu Seppälä, Guagli Yang, Andrea Kindler-Röhrborn, Heikki Minn, Salli Kärnä, Riikka Viitanen, Maria Gardberg, Piritta Saipa, Johan Rajander, Hasan Mansour A Mansour, Nathan A. Cleveland, and Prof. Philip S. Low, my thanks for your time and valuable scientific contributions to the process! Thank you also to Jason Lewis at the Memorial Sloan Kettering Cancer Center who we collaborated with in the [^{18}F]FGln projects as well as Dr. Mark Dunphy (DO) who diligently responded to my personal inquiries into his own work on [^{18}F]FGln.

Of course, there are some huge thanks required for my direct co-supervisor and supervisor respectively, Asst. Prof. Xiang-Guo Li (PhD) and Prof. Anne Roivainen (PhD). You have helped so much in helping me both grow my skills and guide me in the scientific field. Xiang, you have been a great co-supervisor sharing and teaching so many practical skills in the lab with patience and understanding. It has been a joy to work and learn from you in the field of radiochemistry. Anne, you have helped guide me with so many big-picture research planning and have been exceptionally patient with explaining aspects of the field I am less familiar with. Your availability during exceptional office hours to ensure that important grant, review, and submission deadlines are met is remarkable. The speed and efficiency at which you process and review documents is also remarkable and whenever possible I always try to mimic the type of work ethic you put forward.

A special thanks to Ollio Moisio who, despite not (yet) sharing a publication with me, has worked with me on contracted projects. While sharing a cubicle for the large portion of my time here in Turku, You have been a great friend and mentor over a wide variety of personal and academic things. My thanks also to the rest of the research group members in both the Li and Roivainen groups who have also been great to interact with on a daily basis. For the newer members it has been great to share some of the things I have learned with you and hone my skills as a teacher and for the older ones it was great to learn from you. I enjoy the ongoing collaboration projects with you all so thank you Erika, Imran, Andriana, Senthil, Pyry, Jesse, and Jonne.

An exceptional thanks to the Turku PET Centre staff who really make this place an amazing place to conduct research. Thank you Juhani Knuuti for helping bring together so many talented people into a productive space for science development

and for having an always open welcoming demeanour and also for the rest of the talented staff. The Carimas developers and IT staff here at the Turku PET centre are also sincerely thanked. Particularly Sauli and Timo who make great image analysis software and still smile when I constantly bother them about custom additions, versions or weird bugs. Rami, also you have been instrumental in helping us get legacy-software compatible stations for connecting with old equipment and devices. Thank you!

My thanks to my dissertation opponent Prof. Klaus Kopka (PhD) who, despite being a figurative giant in the field of radiochemistry and the director of prestigious radiopharmaceutical research institution in Germany, has agreed to take the time out of his undoubtedly fully-booked schedule to challenge this work. It is an absolute honour and an unusual occurrence to have such a respected and big name in the field agree to be an opponent for a defence which is quite terrifying to say the least. I hope this work is up to your standards and I can answer your critiques to at least some satisfaction!

I would also like to thank my family- both back in Canada ja nyt myös Suomessa who have supported me in numerous untold ways over the years. Speaking of family, I look forward to the birth of my first child some time in November and the accompanying big life changes with my partner Hanna who is also always supportive! To my climbing friends near and far, especially the Teknopojat, whom I share a very special bond through a rope, on the rock, on ice, and through deep shared experiences, thanks for keeping me sane and fit all of these years! Lastly, thank you, dear reader, for taking the time to read through this work and make it this far (assuming you did not skip ahead!).

Thank you all for your time, the most precious thing of all,

Max

References

Agarwal, S. *et al.* (2011) 'Delivery of molecularly targeted therapy to malignant glioma, a disease of the whole brain', *Expert Reviews in Molecular Medicine*, 13, p. e17. Available at: https://doi.org/10.1017/S1462399411001888.

Allott, L. and Aboagye, E.O. (2020) 'Chemistry Considerations for the Clinical Translation of Oncology PET Radiopharmaceuticals', *Molecular Pharmaceutics*, 17(7), pp. 2245–2259. Available at: https://doi.org/10.1021/acs.molpharmaceut.0c00328.

Alzial, G. *et al.* (2022) 'Wild-type isocitrate dehydrogenase under the spotlight in glioblastoma', *Oncogene*, 41(5), pp. 613–621. Available at: https://doi.org/10.1038/s41388-021-02056-1.

Assaraf, Y.G., Leamon, C.P. and Reddy, J.A. (2014) 'The folate receptor as a rational therapeutic target for personalized cancer treatment', *Drug Resistance Updates*, 17(4–6), pp. 89–95. Available at: https://doi.org/10.1016/j.drup.2014.10.002.

Bagley, S.J. *et al.* (2018) 'CAR T-cell therapy for glioblastoma: recent clinical advances and future challenges', *Neuro-Oncology*, 20(11), pp. 1429–1438. Available at: https://doi.org/10.1093/neuonc/noy032.

Bailey, L.B. and Gregory, J.F. (1999) 'Folate Metabolism and Requirements ', *The Journal of Nutrition*, 129(4), pp. 779–782. Available at: https://doi.org/10.1093/jn/129.4.779.

Barca, C. *et al.* (2021) 'Expanding Theranostic Radiopharmaceuticals for Tumor Diagnosis and Therapy', *Pharmaceuticals*, 15(1), p. 13. Available at: https://doi.org/10.3390/ph15010013.

Bashir, A. *et al.* (2019) 'Recurrent glioblastoma versus late posttreatment changes: diagnostic accuracy of O-(2-[18F]fluoroethyl)-L-tyrosine positron emission tomography (18F-FET PET)', *Neuro-Oncology*, 21(12), pp. 1595–1606. Available at: https://doi.org/10.1093/neuonc/noz166.

Basu, S. *et al.* (2011) 'Fundamentals of PET and PET/CT imaging', *Annals of the New York Academy of Sciences*, 1228(1), pp. 1–18. Available at: https://doi.org/10.1111/j.1749-6632.2011.06077.x.

Bera, S. *et al.* (2016) 'Robust regulation of hepatic pericentral amination by glutamate dehydrogenase kinetics', *Integrative Biology*, 8(11), pp. 1126–1132. Available at: https://doi.org/10.1039/C6IB00158K.

Bernard, W.S. and Christopher, P.W. (2014) *World Cancer Report 2014*. 1st edn.

Bode, B.P. (2001) 'Recent Molecular Advances in Mammalian Glutamine Transport', *The Journal of Nutrition*, 131(9), pp. 2475S-2485S. Available at: https://doi.org/10.1093/jn/131.9.2475S.

Boss, S.D. and Ametamey, S.M. (2020) 'Development of Folate Receptor−Targeted PET Radiopharmaceuticals for Tumor Imaging—A Bench-to-Bedside Journey', *Cancers*, 12(6), p. 1508. Available at: https://doi.org/10.3390/cancers12061508.

Boza, J.J. *et al.* (2000) 'Role of glutamine on the de novo purine nucleotide synthesis in Caco-2 cells', *European Journal of Nutrition*, 39(1), pp. 38–46. Available at: https://doi.org/10.1007/s003940050074.

Broos, W.A.M. *et al.* (2018) 'Accuracy of 18F-NaF PET/CT in bone metastasis detection and its effect on patient management in patients with breast carcinoma', *Nuclear Medicine Communications*, 39(4), pp. 325–333. Available at: https://doi.org/10.1097/MNM.0000000000000807.

Bunse, L. *et al.* (2018) 'Suppression of antitumor T cell immunity by the oncometabolite (R)-2-hydroxyglutarate', *Nature Medicine*, 24(8), pp. 1192–1203. Available at: https://doi.org/10.1038/s41591-018-0095-6.

Burchenal, J.H. *et al.* (1954) 'CLINICAL STUDIES ON 6-MERCAPTOPURINE', *Annals of the New York Academy of Sciences*, 60(2), pp. 359–368. Available at: https://doi.org/10.1111/j.1749-6632.1954.tb40024.x.

Burt, B.M. *et al.* (2001) 'Using Positron Emission Tomography with [18F]FDG to Predict Tumor Behavior in Experimental Colorectal Cancer', *Neoplasia*, 3(3), pp. 189–195. Available at: https://doi.org/10.1038/sj.neo.7900147.

Buus, S. *et al.* (2004) '11C-methionine PET, a novel method for measuring regional salivary gland function after radiotherapy of head and neck cancer', *Radiotherapy and Oncology*, 73(3), pp. 289–296. Available at: https://doi.org/10.1016/j.radonc.2004.09.009.

Calvert, A.E. *et al.* (2017) 'Cancer-Associated IDH1 Promotes Growth and Resistance to Targeted Therapies in the Absence of Mutation', *Cell Reports*, 19(9), pp. 1858–1873. Available at: https://doi.org/10.1016/j.celrep.2017.05.014.

Cao, Y. *et al.* (2017) 'Glutamic Pyruvate Transaminase GPT2 Promotes Tumorigenesis of Breast Cancer Cells by Activating Sonic Hedgehog Signaling', *Theranostics*, 7(12), pp. 3021–3033. Available at: https://doi.org/10.7150/thno.18992.

Chan, E.S.L. and Cronstein, B.N. (2010) 'Methotrexate—how does it really work?', *Nature Reviews Rheumatology*, 6(3), pp. 175–178. Available at: https://doi.org/10.1038/nrrheum.2010.5.

Chan, F.P.H. *et al.* (1995) 'Chromosomal localization of the reduced folate transporter gene (SLC19A1) in Chinese hamster ovary cells', *Cytogenetic and Genome Research*, 71(2), pp. 148–150. Available at: https://doi.org/10.1159/000134095.

Chen, J.-Q. and Russo, J. (2012) 'Dysregulation of glucose transport, glycolysis, TCA cycle and glutaminolysis by oncogenes and tumor suppressors in cancer cells', *Biochimica et Biophysica Acta (BBA) - Reviews on Cancer*, 1826(2), pp. 370–384. Available at: https://doi.org/10.1016/j.bbcan.2012.06.004.

Chen, Q. *et al.* (2016) 'Synthesis and Preclinical Evaluation of Folate-NOTA-Al ^{18}F for PET Imaging of Folate-Receptor-Positive Tumors', *Molecular Pharmaceutics*, 13(5), pp. 1520–1527. Available at: https://doi.org/10.1021/acs.molpharmaceut.5b00989.

Chen, Q. *et al.* (2017) 'Folate-PEG-NOTA-Al ^{18}F: A New Folate Based Radiotracer for PET Imaging of Folate Receptor-Positive Tumors', *Molecular Pharmaceutics*, 14(12), pp. 4353–4361. Available at: https://doi.org/10.1021/acs.molpharmaceut.7b00415.

Chen, S.-H. and Giblett, E.R. (1971) 'Polymorphism of Soluble Glutamic-Pyruvic Transaminase: A New Genetic Marker in Man', *Science*, 173(3992), pp. 148–149. Available at: https://doi.org/10.1126/science.173.3992.148.

Cheung, A. *et al.* (2016) 'Targeting folate receptor alpha for cancer treatment', *Oncotarget*, 7(32), pp. 52553–52574. Available at: https://doi.org/10.18632/oncotarget.9651.

Christensen, K.E. and MacKenzie, R.E. (2008) 'Chapter 14 Mitochondrial Methylenetetrahydrofolate Dehydrogenase, Methenyltetrahydrofolate Cyclohydrolase, and Formyltetrahydrofolate Synthetases', in, pp. 393–410. Available at: https://doi.org/10.1016/S0083-6729(08)00414-7.

Claes, A., Idema, A.J. and Wesseling, P. (2007) 'Diffuse glioma growth: a guerilla war', *Acta Neuropathologica*, 114(5), pp. 443–458. Available at: https://doi.org/10.1007/s00401-007-0293-7.

Clark, J.C. and Silvester, D.J. (1966) 'A cyclotron method for the production of fluorine-18', *The International Journal of Applied Radiation and Isotopes*, 17(3), pp. 151–154. Available at: https://doi.org/10.1016/0020-708X(66)90039-1.

Conti, M. and Eriksson, L. (2016) 'Physics of pure and non-pure positron emitters for PET: a review and a discussion', *EJNMMI Physics*, 3(1), p. 8. Available at: https://doi.org/10.1186/s40658-016-0144-5.

Cooper, A.J.L. *et al.* (2012) 'Comparative enzymology of (2S,4R)4-fluoroglutamine and (2S,4R)4-fluoroglutamate', *Comparative Biochemistry and Physiology Part B: Biochemistry and Molecular Biology*, 163(1), pp. 108–120. Available at: https://doi.org/10.1016/j.cbpb.2012.05.010.

Cormerais, Y. *et al.* (2016) 'Genetic Disruption of the Multifunctional CD98/LAT1 Complex Demonstrates the Key Role of Essential Amino Acid Transport in the Control of mTORC1 and Tumor Growth', *Cancer Research*, 76(15), pp. 4481–4492. Available at: https://doi.org/10.1158/0008-5472.CAN-15-3376.

Crider, K.S. *et al.* (2022) 'Folic Acid and the Prevention of Birth Defects: 30 Years of Opportunity and Controversies', *Annual Review of Nutrition*, 42(1), pp. 423–452. Available at: https://doi.org/10.1146/annurev-nutr-043020-091647.

Cronk, J.C. and Kipnis, J. (2013) 'Microglia – the brain's busy bees', *F1000Prime Reports*, 5. Available at: https://doi.org/10.12703/P5-53.

Czernin, J., Satyamurthy, N. and Schiepers, C. (2010) 'Molecular Mechanisms of Bone ^{18} F-NaF Deposition', *Journal of Nuclear Medicine*, 51(12), pp. 1826–1829. Available at: https://doi.org/10.2967/jnumed.110.077933.

van Dam, G.M. *et al.* (2011) 'Intraoperative tumor-specific fluorescence imaging in ovarian cancer by folate receptor-α targeting: first in-human results', *Nature Medicine*, 17(10), pp. 1315–1319. Available at: https://doi.org/10.1038/nm.2472.

Dang, L. *et al.* (2009) 'Cancer-associated IDH1 mutations produce 2-hydroxyglutarate', *Nature*, 462(7274), pp. 739–744. Available at: https://doi.org/10.1038/nature08617.

Davis, M. (2016) 'Glioblastoma: Overview of Disease and Treatment', *Clinical Journal of Oncology Nursing*, 20(5), pp. S2–S8. Available at: https://doi.org/10.1188/16.CJON.S1.2-8.

Davis, R.E. and Nicol, D.J. (1988) 'Folic acid', *International Journal of Biochemistry*, 20(2), pp. 133–139. Available at: https://doi.org/10.1016/0020-711X(88)90476-4.

Dinnes, J. *et al.* (2002) 'A rapid and systematic review of the effectiveness of temozolomide for the treatment of recurrent malignant glioma', *British Journal of Cancer*, 86(4), pp. 501–505. Available at: https://doi.org/10.1038/sj.bjc.6600135.

Du, X. and Hu, H. (2021) 'The Roles of 2-Hydroxyglutarate', *Frontiers in Cell and Developmental Biology*, 9. Available at: https://doi.org/10.3389/fcell.2021.651317.

Dunphy, M.P.S. *et al.* (2018) 'In Vivo PET Assay of Tumor Glutamine Flux and Metabolism: In-Human Trial of ^{18} F-(2 *S* ,4 *R*)-4-Fluoroglutamine', *Radiology*, 287(2), pp. 667–675. Available at: https://doi.org/10.1148/radiol.2017162610.

Durán, R.V. *et al.* (2012) 'Glutaminolysis Activates Rag-mTORC1 Signaling', *Molecular Cell*, 47(3), pp. 349–358. Available at: https://doi.org/10.1016/j.molcel.2012.05.043.

Ebert, A. *et al.* (2006) 'Histone modification and the control of heterochromatic gene silencing in Drosophila', *Chromosome Research*, 14(4), pp. 377–392. Available at: https://doi.org/10.1007/s10577-006-1066-1.

Edlow, B.L. *et al.* (2019) '7 Tesla MRI of the ex vivo human brain at 100 micron resolution', *Scientific Data*, 6(1), p. 244. Available at: https://doi.org/10.1038/s41597-019-0254-8.

Emery, J.F. *et al.* (1972) 'Half-Lives of Radionuclides—IV', *Nuclear Science and Engineering*, 48(3), pp. 319–323. Available at: https://doi.org/10.13182/NSE72-A22489.

Fan, X., Salford, L.G. and Widegren, B. (2007) 'Glioma stem cells: Evidence and limitation', *Seminars in Cancer Biology*, 17(3), pp. 214–218. Available at: https://doi.org/10.1016/j.semcancer.2006.04.002.

Fani, M., Peitl, P. and Velikyan, I. (2017) 'Current Status of Radiopharmaceuticals for the Theranostics of Neuroendocrine Neoplasms', *Pharmaceuticals*, 10(4), p. 30. Available at: https://doi.org/10.3390/ph10010030.

Farin, A. *et al.* (2006) 'Transplanted glioma cells migrate and proliferate on host brain vasculature: A dynamic analysis', *Glia*, 53(8), pp. 799–808. Available at: https://doi.org/10.1002/glia.20334.

Fu, R. *et al.* (2018) 'Antibody Fragment and Affibody ImmunoPET Imaging Agents: Radiolabelling Strategies and Applications', *ChemMedChem*, 13(23), pp. 2466–2478. Available at: https://doi.org/10.1002/cmdc.201800624.

Fu, Z. *et al.* (2023) 'Custom-built automated radiosynthesis platform for Al[18F]F radiochemistry and its application for clinical production', *Chemical Engineering Journal*, 456, p. 141080. Available at: https://doi.org/10.1016/J.CEJ.2022.141080.

Fuchs, S.A. *et al.* (2005) 'd-Amino acids in the central nervous system in health and disease', *Molecular Genetics and Metabolism*, 85(3), pp. 168–180. Available at: https://doi.org/10.1016/j.ymgme.2005.03.003.

Galldiks, N. *et al.* (2021) 'Contribution of PET imaging to radiotherapy planning and monitoring in glioma patients - a report of the PET/RANO group', *Neuro-Oncology*, 23(6), pp. 881–893. Available at: https://doi.org/10.1093/neuonc/noab013.

Garcia, B.A. *et al.* (2016) 'Folate deficiency affects histone methylation', *Medical Hypotheses*, 88, pp. 63–67. Available at: https://doi.org/10.1016/j.mehy.2015.12.027.

Georgescu, M.-M. (2021) 'Multi-Platform Classification of IDH-Wild-Type Glioblastoma Based on ERK/MAPK Pathway: Diagnostic, Prognostic and Therapeutic Implications', *Cancers*, 13(18), p. 4532. Available at: https://doi.org/10.3390/cancers13184532.

Ginter, P.S. *et al.* (2017) 'Folate Receptor Alpha Expression Is Associated With Increased Risk of Recurrence in Triple-negative Breast Cancer', *Clinical Breast Cancer*, 17(7), pp. 544–549. Available at: https://doi.org/10.1016/j.clbc.2017.03.007.

Glaudemans, A.W.J.M. *et al.* (2013) 'Value of 11C-methionine PET in imaging brain tumours and metastases', *European Journal of Nuclear Medicine and Molecular Imaging*, 40(4), pp. 615–635. Available at: https://doi.org/10.1007/s00259-012-2295-5.

Gnesin, S. *et al.* (2020) 'Radiation dosimetry of 18F-AzaFol: A first in-human use of a folate receptor PET tracer', *EJNMMI Research*, 10(1), p. 32. Available at: https://doi.org/10.1186/s13550-020-00624-2.

Grkovski, M. *et al.* (2020) 'Pharmacokinetic Assessment of ^{18} F-(2 *S,* 4 *R*)-4-Fluoroglutamine in Patients with Cancer', *Journal of Nuclear Medicine*, 61(3), pp. 357–366. Available at: https://doi.org/10.2967/jnumed.119.229740.

Hamoudeh, M. *et al.* (2008) 'Radionuclides delivery systems for nuclear imaging and radiotherapy of cancer', *Advanced Drug Delivery Reviews*, 60(12), pp. 1329–1346. Available at: https://doi.org/10.1016/j.addr.2008.04.013.

Hart, M.G. *et al.* (2019) 'Biopsy versus resection for high-grade glioma', *Cochrane Database of Systematic Reviews*, 2019(6). Available at: https://doi.org/10.1002/14651858.CD002034.pub2.

Hashimoto, H., Vertino, P.M. and Cheng, X. (2010) 'Molecular coupling of DNA methylation and histone methylation', *Epigenomics*, 2(5), pp. 657–669. Available at: https://doi.org/10.2217/epi.10.44.

Hasselbalch, S.G. *et al.* (1996) 'Transport of D-Glucose and 2-Fluorodeoxyglucose across the Blood-Brain Barrier in Humans', *Journal of Cerebral Blood Flow & Metabolism*, 16(4), pp. 659–666. Available at: https://doi.org/10.1097/00004647-199607000-00017.

Hawkins, R.A. *et al.* (2006) 'Structure of the Blood–Brain Barrier and Its Role in the Transport of Amino Acids', *The Journal of Nutrition*, 136(1), pp. S218–S226. Available at: https://doi.org/10.1093/jn/136.1.218S.

Herreño, A.M. *et al.* (2018) 'Primary lung cancer cell culture from transthoracic needle biopsy samples', *Cogent Medicine*, 5(1), p. 1503071. Available at: https://doi.org/10.1080/2331205X.2018.1503071.

Herschman, H.R. (2003) 'Micro-PET imaging and small animal models of disease', *Current Opinion in Immunology*, 15(4), pp. 378–384. Available at: https://doi.org/10.1016/S0952-7915(03)00066-9.

von Hevesy, G. (1913) 'XL. *The valency of the radioelements*', *The London, Edinburgh, and Dublin Philosophical Magazine and Journal of Science*, 25(147), pp. 390–414. Available at: https://doi.org/10.1080/14786440308634175.

Hicks, J.W. *et al.* (2010) 'Radiolabeled Small Molecule Protein Kinase Inhibitors for Imaging with PET or SPECT', *Molecules*, 15(11), pp. 8260–8278. Available at: https://doi.org/10.3390/molecules15118260.

Hou, Z. and Matherly, L.H. (2014) 'Biology of the Major Facilitative Folate Transporters SLC19A1 and SLC46A1', in, pp. 175–204. Available at: https://doi.org/10.1016/B978-0-12-800223-0.00004-9.

Hu, Z. *et al.* (2014) 'Quantitative Liver-Specific Protein Fingerprint in Blood: A Signature for Hepatotoxicity', *Theranostics*, 4(2), pp. 215–228. Available at: https://doi.org/10.7150/thno.7868.

Hutterer, M. *et al.* (2013) '[18F]-fluoro-ethyl-l-tyrosine PET: a valuable diagnostic tool in neuro-oncology, but not all that glitters is glioma', *Neuro-Oncology*, 15(3), pp. 341–351. Available at: https://doi.org/10.1093/neuonc/nos300.

Inubushi, M. *et al.* (2018) 'European research trends in nuclear medicine', *Annals of Nuclear Medicine*, 32(9), pp. 579–582. Available at: https://doi.org/10.1007/s12149-018-1303-7.

Jäkel, S. and Dimou, L. (2017) 'Glial Cells and Their Function in the Adult Brain: A Journey through the History of Their Ablation', *Frontiers in Cellular Neuroscience*, 11. Available at: https://doi.org/10.3389/fncel.2017.00024.

Jessen, K.R. (2004) 'Glial cells', *The International Journal of Biochemistry & Cell Biology*, 36(10), pp. 1861–1867. Available at: https://doi.org/10.1016/j.biocel.2004.02.023.

Jiang, B. *et al.* (2017) 'Biopsy versus resection for the management of low-grade gliomas', *Cochrane Database of Systematic Reviews*, 2020(6). Available at: https://doi.org/10.1002/14651858.CD009319.pub3.

Johnson, G.A. *et al.* (2023) 'Merged magnetic resonance and light sheet microscopy of the whole mouse brain', *Proceedings of the National Academy of Sciences*, 120(17). Available at: https://doi.org/10.1073/pnas.2218617120.

Kawamura, Y. *et al.* (2018) 'New aspects of glioblastoma multiforme revealed by similarities between neural and glioblastoma stem cells', *Cell Biology and Toxicology*, 34(6), pp. 425–440. Available at: https://doi.org/10.1007/s10565-017-9420-y.

Ke, C. (2004) 'Folate-receptor-targeted radionuclide imaging agents', *Advanced Drug Delivery Reviews*, 56(8), pp. 1143–1160. Available at: https://doi.org/10.1016/j.addr.2004.01.004.

Kelloff, G.J. *et al.* (2005) 'Progress and Promise of FDG-PET Imaging for Cancer Patient Management and Oncologic Drug Development', *Clinical Cancer Research*, 11(8), pp. 2785–2808. Available at: https://doi.org/10.1158/1078-0432.CCR-04-2626.

Kim, G.G. *et al.* (2020) 'Tumor Targeting Effect of Triphenylphosphonium Cations and Folic Acid Coated with Zr-89-Labeled Silica Nanoparticles', *Molecules*, 25(12), p. 2922. Available at: https://doi.org/10.3390/molecules25122922.

Kolodkin-Gal, I. *et al.* (2010) '<scp>d</scp> -Amino Acids Trigger Biofilm Disassembly', *Science*, 328(5978), pp. 627–629. Available at: https://doi.org/10.1126/science.1188628.

Kręcisz, P. *et al.* (2021) 'Radiolabeled Peptides and Antibodies in Medicine', *Bioconjugate Chemistry*, 32(1), pp. 25–42. Available at: https://doi.org/10.1021/acs.bioconjchem.0c00617.

Kunos, C.A. *et al.* (2021) 'Radiopharmaceutical Validation for Clinical Use', *Frontiers in Oncology*, 11. Available at: https://doi.org/10.3389/fonc.2021.630827.

Kusi, M. *et al.* (2022) '2-Hydroxyglutarate destabilizes chromatin regulatory landscape and lineage fidelity to promote cellular heterogeneity', *Cell Reports*, 38(2), p. 110220. Available at: https://doi.org/10.1016/j.celrep.2021.110220.

LaPorte, D.C., Thorsness, P.E. and Koshland, D.E. (1985) 'Compensatory phosphorylation of isocitrate dehydrogenase. A mechanism for adaptation to the intracellular environment.', *Journal of Biological Chemistry*, 260(19), pp. 10563–10568. Available at: https://doi.org/10.1016/S0021-9258(19)85122-0.

Lee, S.Y. (2016) 'Temozolomide resistance in glioblastoma multiforme', *Genes & Diseases*, 3(3), pp. 198–210. Available at: https://doi.org/10.1016/j.gendis.2016.04.007.

Li, C. *et al.* (2018) 'Preclinical study of an 18F-labeled glutamine derivative for cancer imaging', *Nuclear Medicine and Biology*, 64–65, pp. 34–40. Available at: https://doi.org/10.1016/j.nucmedbio.2018.06.007.

Li, Y. *et al.* (2021) 'Characterization of a new human astrocytoma cell line SHG140: cell proliferation, cell phenotype, karyotype, STR markers and tumorigenicity analysis', *Journal of Cancer*, 12(2), pp. 371–378. Available at: https://doi.org/10.7150/jca.40802.

Liang, X. *et al.* (2020) 'NEMA-2008 and In-Vivo Animal and Plant Imaging Performance of the Large FOV Preclinical Digital PET/CT System Discoverist 180', *IEEE Transactions on Radiation and*

Plasma Medical Sciences, 4(5), pp. 622–629. Available at: https://doi.org/10.1109/TRPMS.2020.2983221.

Lieberman, B.P. *et al.* (2011) 'PET Imaging of Glutaminolysis in Tumors by ^{18}F-(*2S,4R*)4-Fluoroglutamine', *Journal of Nuclear Medicine*, 52(12), pp. 1947–1955. Available at: https://doi.org/10.2967/jnumed.111.093815.

Liu, D. *et al.* (2022) 'Radiolabeling of functional oligonucleotides for molecular imaging', *Frontiers in Bioengineering and Biotechnology*, 10. Available at: https://doi.org/10.3389/fbioe.2022.986412.

Liu, F. *et al.* (2018) 'PET Imaging of ^{18}F-(2*S*,4*R*)4-Fluoroglutamine Accumulation in Breast Cancer: From Xenografts to Patients', *Molecular Pharmaceutics*, 15(8), pp. 3448–3455. Available at: https://doi.org/10.1021/acs.molpharmaceut.8b00430.

Liu, H.-Y., Liu, S.-M. and Zhang, Y.-Z. (2020) 'Maternal Folic Acid Supplementation Mediates Offspring Health via DNA Methylation', *Reproductive Sciences*, 27(4), pp. 963–976. Available at: https://doi.org/10.1007/s43032-020-00161-2.

Liu, Y., Liu, G. and Hnatowich, D. (2010) 'A Brief Review of Chelators for Radiolabeling Oligomers', *Materials*, 3(5), pp. 3204–3217. Available at: https://doi.org/10.3390/ma3053204.

Lodge, M.A. *et al.* (2018) 'Measuring PET Spatial Resolution Using a Cylinder Phantom Positioned at an Oblique Angle', *Journal of Nuclear Medicine*, 59(11), pp. 1768–1775. Available at: https://doi.org/10.2967/jnumed.118.209593.

Louis, D.N. *et al.* (2021) 'The 2021 WHO classification of tumors of the central nervous system: A summary', *Neuro-Oncology*, 23(8). Available at: https://doi.org/10.1093/neuonc/noab106.

Low, P.S. and Kularatne, S.A. (2009) 'Folate-targeted therapeutic and imaging agents for cancer', *Current Opinion in Chemical Biology*, 13(3), pp. 256–262. Available at: https://doi.org/10.1016/j.cbpa.2009.03.022.

Lu, V.M. *et al.* (2018) 'The Survival Effect of Repeat Surgery at Glioblastoma Recurrence and its Trend: A Systematic Review and Meta-Analysis', *World Neurosurgery*, 115, pp. 453-459.e3. Available at: https://doi.org/10.1016/j.wneu.2018.04.016.

Macheda, M.L., Rogers, S. and Best, J.D. (2005) 'Molecular and cellular regulation of glucose transporter (GLUT) proteins in cancer', *Journal of Cellular Physiology*, 202(3), pp. 654–662. Available at: https://doi.org/10.1002/jcp.20166.

Martikainen, M. and Essand, M. (2019) 'Virus-Based Immunotherapy of Glioblastoma', *Cancers*, 11(2), p. 186. Available at: https://doi.org/10.3390/cancers11020186.

Mastorodemos, V. *et al.* (2009) 'Human *GLUD1* and *GLUD2* glutamate dehydrogenase localize to mitochondria and endoplasmic reticulum', *Biochemistry and Cell Biology*, 87(3), pp. 505–516. Available at: https://doi.org/10.1139/O09-008.

Matés, J.M. *et al.* (2002) 'Glutamine and its relationship with intracellular redox status, oxidative stress and cell proliferation/death', *The International Journal of Biochemistry & Cell Biology*, 34(5), pp. 439–458. Available at: https://doi.org/10.1016/S1357-2725(01)00143-1.

Matherly, L.H., Hou, Z. and Deng, Y. (2007) 'Human reduced folate carrier: translation of basic biology to cancer etiology and therapy', *Cancer and Metastasis Reviews*, 26(1), pp. 111–128. Available at: https://doi.org/10.1007/s10555-007-9046-2.

Matsuo, M. *et al.* (2012) 'Impact of [11C]Methionine Positron Emission Tomography for Target Definition of Glioblastoma Multiforme in Radiation Therapy Planning', *International Journal of Radiation Oncology*Biology*Physics*, 82(1), pp. 83–89. Available at: https://doi.org/10.1016/j.ijrobp.2010.09.020.

McCord, E. *et al.* (2021) 'Folate Receptors' Expression in Gliomas May Possess Potential Nanoparticle-Based Drug Delivery Opportunities', *ACS Omega*, 6(6), pp. 4111–4118. Available at: https://doi.org/10.1021/acsomega.0c05500.

Meister, A. (1974) '23. Glutamine Synthetase of Mammals', in, pp. 699–754. Available at: https://doi.org/10.1016/S1874-6047(08)60155-9.

Miner, M.W.G. *et al.* (2021) 'Comparison of: (2S,4R)-4-[18F]Fluoroglutamine, [11C]Methionine, and 2-Deoxy-2-[18F]Fluoro-D-Glucose and Two Small-Animal PET/CT Systems Imaging Rat Gliomas', *Frontiers in Oncology*, 11. Available at: https://doi.org/10.3389/fonc.2021.730358.

Missailidis, S. and Perkins, A. (2007) '*Update:* Aptamers as Novel Radiopharmaceuticals: Their Applications and Future Prospects in Diagnosis and Therapy', *Cancer Biotherapy and Radiopharmaceuticals*, 22(4), pp. 453–468. Available at: https://doi.org/10.1089/cbr.2007.357.

Mitchell, J.B.O. and Smith, J. (2003) 'D-amino acid residues in peptides and proteins', *Proteins: Structure, Function, and Bioinformatics*, 50(4), pp. 563–571. Available at: https://doi.org/10.1002/prot.10320.

Müller, C. (2013) 'Folate-Based Radiotracers for PET Imaging—Update and Perspectives', *Molecules*, 18(5), pp. 5005–5031. Available at: https://doi.org/10.3390/molecules18055005.

Naqa, I. El (2014) 'The role of quantitative PET in predicting cancer treatment outcomes', *Clinical and Translational Imaging*, 2(4), pp. 305–320. Available at: https://doi.org/10.1007/s40336-014-0063-1.

Nicholson, J.G. and Fine, H.A. (2021) 'Diffuse Glioma Heterogeneity and Its Therapeutic Implications', *Cancer Discovery*, 11(3), pp. 575–590. Available at: https://doi.org/10.1158/2159-8290.CD-20-1474.

Nicholson, R.I., Gee, J.M.W. and Harper, M.E. (2001) 'EGFR and cancer prognosis', *European Journal of Cancer*, 37, pp. 9–15. Available at: https://doi.org/10.1016/S0959-8049(01)00231-3.

Nurse, P. and Wiemken, A. (1974) 'Amino Acid Pools and Metabolism During the Cell Division Cycle of Arginine-Grown *Candida utilis*', *Journal of Bacteriology*, 117(3), pp. 1108–1116. Available at: https://doi.org/10.1128/jb.117.3.1108-1116.1974.

Oberheim Bush, N.A. and Chang, S. (2016) 'Treatment Strategies for Low-Grade Glioma in Adults', *Journal of Oncology Practice*, 12(12), pp. 1235–1241. Available at: https://doi.org/10.1200/JOP.2016.018622.

Ohba, S. and HIROSE, Y. (2016) 'Biological Significance of Mutant Isocitrate Dehydrogenase 1 and 2 in Gliomagenesis', *Neurologia medico-chirurgica*, 56(4), pp. 170–179. Available at: https://doi.org/10.2176/nmc.ra.2015-0322.

Ostrom, Q.T. *et al.* (2018) 'Adult Glioma Incidence and Survival by Race or Ethnicity in the United States From 2000 to 2014', *JAMA Oncology*, 4(9), p. 1254. Available at: https://doi.org/10.1001/jamaoncol.2018.1789.

Palmer, B.F. and Clegg, D.J. (2021) 'Starvation Ketosis and the Kidney', *American Journal of Nephrology*, 52(6), pp. 467–478. Available at: https://doi.org/10.1159/000517305.

Pan, Y. *et al.* (2014) 'Quantitative proteomics reveals the kinetics of trypsin-catalyzed protein digestion', *Analytical and Bioanalytical Chemistry*, 406(25), pp. 6247–6256. Available at: https://doi.org/10.1007/s00216-014-8071-6.

Parsons, D.W. *et al.* (2008) 'An Integrated Genomic Analysis of Human Glioblastoma Multiforme', *Science*, 321(5897), pp. 1807–1812. Available at: https://doi.org/10.1126/science.1164382.

Pascali, G. *et al.* (2014) 'Hardware and software modifications on the Advion NanoTek microfluidic platform to extend flexibility for radiochemical synthesis', *Applied Radiation and Isotopes*, 84, pp. 40–47. Available at: https://doi.org/10.1016/j.apradiso.2013.10.020.

Perrin, S.L. *et al.* (2019) 'Glioblastoma heterogeneity and the tumour microenvironment: implications for preclinical research and development of new treatments', *Biochemical Society Transactions*, 47(2), pp. 625–638. Available at: https://doi.org/10.1042/BST20180444.

Phelps, M.E. *et al.* (1975) 'Application of annihilation coincidence detection to transaxial reconstruction tomography.', *Journal of nuclear medicine : official publication, Society of Nuclear Medicine*, 16(3), pp. 210–24.

Pike, V.W. (2009) 'PET radiotracers: crossing the blood–brain barrier and surviving metabolism', *Trends in Pharmacological Sciences*, 30(8), pp. 431–440. Available at: https://doi.org/10.1016/j.tips.2009.05.005.

Pineau, I. *et al.* (2010) 'Astrocytes initiate inflammation in the injured mouse spinal cord by promoting the entry of neutrophils and inflammatory monocytes in an IL-1 receptor/MyD88-dependent

fashion', *Brain, Behavior, and Immunity*, 24(4), pp. 540–553. Available at: https://doi.org/10.1016/j.bbi.2009.11.007.

Prasetyanti, P.R. and Medema, J.P. (2017) 'Intra-tumor heterogeneity from a cancer stem cell perspective', *Molecular Cancer*, 16(1), p. 41. Available at: https://doi.org/10.1186/s12943-017-0600-4.

Qu, W. *et al.* (2011) 'Synthesis of Optically Pure 4-Fluoro-Glutamines as Potential Metabolic Imaging Agents for Tumors', *Journal of the American Chemical Society*, 133(4), pp. 1122–1133. Available at: https://doi.org/10.1021/ja109203d.

Qu, W. *et al.* (2012) 'Preparation and Characterization of l-[5- ^{11} C]-Glutamine for Metabolic Imaging of Tumors', *Journal of Nuclear Medicine*, 53(1), pp. 98–105. Available at: https://doi.org/10.2967/jnumed.111.093831.

Radchenko, V., Baimukhanova, A. and Filosofov, D. (2021) 'Radiochemical aspects in modern radiopharmaceutical trends: a practical guide', *Solvent Extraction and Ion Exchange*, 39(7), pp. 714–744. Available at: https://doi.org/10.1080/07366299.2021.1874099.

Rangger, C. and Haubner, R. (2020) 'Radiolabelled Peptides for Positron Emission Tomography and Endoradiotherapy in Oncology', *Pharmaceuticals*, 13(2), p. 22. Available at: https://doi.org/10.3390/ph13020022.

Reivich, M. *et al.* (1979) 'The [18F]fluorodeoxyglucose method for the measurement of local cerebral glucose utilization in man.', *Circulation Research*, 44(1), pp. 127–137. Available at: https://doi.org/10.1161/01.RES.44.1.127.

Robert H. Whitehead *et al.* (1985) 'A Colon Cancer Cell Line (LIM1215) Derived From a Patient With Inherited Nonpolyposis Colorectal Cancer<xref ref-type="fn" rid="FN1">2</xref>', *JNCI: Journal of the National Cancer Institute* [Preprint]. Available at: https://doi.org/10.1093/jnci/74.4.759.

Rozen, R. (2010) 'Biochemistry and genetics of folate metabolism', *Cerebrospinal Fluid Research*, 7(S1), p. S4. Available at: https://doi.org/10.1186/1743-8454-7-S1-S4.

Sabharanjak, S. (2004) 'Folate receptor endocytosis and trafficking', *Advanced Drug Delivery Reviews*, 56(8), pp. 1099–1109. Available at: https://doi.org/10.1016/j.addr.2004.01.010.

Saha, S.K. *et al.* (2014) 'Mutant IDH inhibits HNF-4α to block hepatocyte differentiation and promote biliary cancer', *Nature*, 513(7516), pp. 110–114. Available at: https://doi.org/10.1038/nature13441.

Sasongko, L. *et al.* (2005) 'Imaging P-glycoprotein transport activity at the human blood-brain barrier with positron emission tomography', *Clinical Pharmacology & Therapeutics*, 77(6), pp. 503–514. Available at: https://doi.org/10.1016/j.clpt.2005.01.022.

Scaglione, F. and Panzavolta, G. (2014) 'Folate, folic acid and 5-methyltetrahydrofolate are not the same thing', *Xenobiotica*, 44(5), pp. 480–488. Available at: https://doi.org/10.3109/00498254.2013.845705.

Scaranti, M. *et al.* (2020) 'Exploiting the folate receptor α in oncology', *Nature Reviews Clinical Oncology*, 17(6), pp. 349–359. Available at: https://doi.org/10.1038/s41571-020-0339-5.

Schaber, E.N. *et al.* (2021) 'Initial Stages of Spontaneous Binding of Folate-Based Vectors to Folate Receptor-α Observed by Unbiased Molecular Dynamics', *The Journal of Physical Chemistry B*, 125(28), pp. 7598–7612. Available at: https://doi.org/10.1021/acs.jpcb.1c00488.

Serefidou, M., Venkatasubramani, A.V. and Imhof, A. (2019) 'The Impact of One Carbon Metabolism on Histone Methylation', *Frontiers in Genetics*, 10. Available at: https://doi.org/10.3389/fgene.2019.00764.

Shashidharan, P. and Plaitakis, A. (2014) 'The Discovery of Human of GLUD2 Glutamate Dehydrogenase and Its Implications for Cell Function in Health and Disease', *Neurochemical Research*, 39(3), pp. 460–470. Available at: https://doi.org/10.1007/s11064-013-1227-5.

Shen, J. *et al.* (2018) 'Assessment of folate receptor alpha and beta expression in selection of lung and pancreatic cancer patients for receptor targeted therapies', *Oncotarget*, 9(4), pp. 4485–4495. Available at: https://doi.org/10.18632/oncotarget.23321.

Sigismund, S., Avanzato, D. and Lanzetti, L. (2018) 'Emerging functions of the <scp>EGFR</scp> in cancer', *Molecular Oncology*, 12(1), pp. 3–20. Available at: https://doi.org/10.1002/1878-0261.12155.

Silvola, J.M.U. *et al.* (2018) 'Aluminum fluoride-18 labeled folate enables in vivo detection of atherosclerotic plaque inflammation by positron emission tomography', *Scientific Reports*, 8(1), p. 9720. Available at: https://doi.org/10.1038/s41598-018-27618-4.

SongTao, Q. *et al.* (2012) 'IDH mutations predict longer survival and response to temozolomide in secondary glioblastoma', *Cancer Science*, 103(2), pp. 269–273. Available at: https://doi.org/10.1111/j.1349-7006.2011.02134.x.

Southworth, R. *et al.* (2003) 'Tissue-specific differences in 2-fluoro-2-deoxyglucose metabolism beyond FDG-6-P: a19F NMR spectroscopy study in the rat', *NMR in Biomedicine*, 16(8), pp. 494–502. Available at: https://doi.org/10.1002/nbm.856.

Spanaki, C. *et al.* (2010) 'Human GLUD2 Glutamate Dehydrogenase Is Expressed in Neural and Testicular Supporting Cells', *Journal of Biological Chemistry*, 285(22), pp. 16748–16756. Available at: https://doi.org/10.1074/jbc.M109.092999.

Srivastava, S. *et al.* (2019) 'A Characterization of Dendritic Cells and Their Role in Immunotherapy in Glioblastoma: From Preclinical Studies to Clinical Trials', *Cancers*, 11(4), p. 537. Available at: https://doi.org/10.3390/cancers11040537.

Stehantsev, P. *et al.* (2021) 'A structural view onto disease-linked mutations in the human neutral amino acid exchanger ASCT1', *Computational and Structural Biotechnology Journal*, 19, pp. 5246–5254. Available at: https://doi.org/10.1016/j.csbj.2021.09.015.

Tan, F. *et al.* (2012) 'Identification of Isocitrate Dehydrogenase 1 as a Potential Diagnostic and Prognostic Biomarker for Non-small Cell Lung Cancer by Proteomic Analysis', *Molecular & Cellular Proteomics*, 11(2), p. M111.008821. Available at: https://doi.org/10.1074/mcp.M111.008821.

Tan, S., Tan, H.T. and Chung, M.C.M. (2008) 'Membrane proteins and membrane proteomics', *PROTEOMICS*, 8(19), pp. 3924–3932. Available at: https://doi.org/10.1002/pmic.200800597.

Teuho, J. *et al.* (2020a) 'Evaluation of image quality with four positron emitters and three preclinical PET/CT systems', *EJNMMI Research*, 10(1), p. 155. Available at: https://doi.org/10.1186/s13550-020-00724-z.

Teuho, J. *et al.* (2020b) 'Evaluation of image quality with four positron emitters and three preclinical PET/CT systems', *EJNMMI Research*, 10(1), p. 155. Available at: https://doi.org/10.1186/s13550-020-00724-z.

Trusheim, J. *et al.* (2017) 'A state-of-the-art review and guidelines for tumor treating fields treatment planning and patient follow-up in glioblastoma', *CNS Oncology*, 6(1), pp. 29–43. Available at: https://doi.org/10.2217/cns-2016-0032.

Tsun, Z.-Y. and Possemato, R. (2015) 'Amino acid management in cancer', *Seminars in Cell & Developmental Biology*, 43, pp. 22–32. Available at: https://doi.org/10.1016/j.semcdb.2015.08.002.

Ulrich, C.M. and Potter, J.D. (2007) 'Folate and Cancer—Timing Is Everything', *JAMA*, 297(21), p. 2408. Available at: https://doi.org/10.1001/jama.297.21.2408.

Venmar, K.T. *et al.* (2015) 'IL4 receptor α mediates enhanced glucose and glutamine metabolism to support breast cancer growth', *Biochimica et Biophysica Acta (BBA) - Molecular Cell Research*, 1853(5), pp. 1219–1228. Available at: https://doi.org/10.1016/j.bbamcr.2015.02.020.

Venneti, S. *et al.* (2015) 'Glutamine-based PET imaging facilitates enhanced metabolic evaluation of gliomas in vivo', *Science Translational Medicine*, 7(274). Available at: https://doi.org/10.1126/scitranslmed.aaa1009.

Vermeulen, K. *et al.* (2019) 'Design and Challenges of Radiopharmaceuticals', *Seminars in Nuclear Medicine*, 49(5), pp. 339–356. Available at: https://doi.org/10.1053/j.semnuclmed.2019.07.001.

Verweij, N.J.F. *et al.* (2020) 'First in man study of [18F]fluoro-PEG-folate PET: a novel macrophage imaging technique to visualize rheumatoid arthritis', *Scientific Reports*, 10(1), p. 1047. Available at: https://doi.org/10.1038/s41598-020-57841-x.

Vyas, M. *et al.* (2022) '<strong>18F-FDG Production and Quality Control (QC) Parameters Comparison in three different Automatic Synthesis Modules: An Experience of Commercial Centre</strong&gt';, *Journal of Nuclear Medicine*, 63(supplement 2), p. 4123. Available at: http://jnm.snmjournals.org/content/63/supplement_2/4123.abstract.

Wadsak, W. and Mitterhauser, M. (2010) 'Basics and principles of radiopharmaceuticals for PET/CT', *European Journal of Radiology*, 73(3), pp. 461–469. Available at: https://doi.org/10.1016/j.ejrad.2009.12.022.

Wagner, C. (2001) 'BIOCHEMICAL ROLE OF FOLATE IN CELLULAR METABOLISM*', *Clinical Research and Regulatory Affairs*, 18(3), pp. 161–180. Available at: https://doi.org/10.1081/CRP-100108171.

Wahl, D.R. *et al.* (2017) 'Glioblastoma Therapy Can Be Augmented by Targeting IDH1-Mediated NADPH Biosynthesis', *Cancer Research*, 77(4), pp. 960–970. Available at: https://doi.org/10.1158/0008-5472.CAN-16-2008.

Wang, P. *et al.* (2015) 'Oncometabolite D-2-Hydroxyglutarate Inhibits ALKBH DNA Repair Enzymes and Sensitizes IDH Mutant Cells to Alkylating Agents', *Cell Reports*, 13(11), pp. 2353–2361. Available at: https://doi.org/10.1016/j.celrep.2015.11.029.

Wang, Z. *et al.* (2015) 'A current review of folate receptor alpha as a potential tumor target in non-small-cell lung cancer', *Drug Design, Development and Therapy*, p. 4989. Available at: https://doi.org/10.2147/DDDT.S90670.

Wasa, M. *et al.* (1996) 'Glutamine as a Regulator of DNA and Protein Biosynthesis in Human Solid Tumor Cell Lines', *Annals of Surgery*, 224(2), pp. 189–197. Available at: https://doi.org/10.1097/00000658-199608000-00012.

Waterhouse, R. (2003) 'Determination of lipophilicity and its use as a predictor of blood–brain barrier penetration of molecular imaging agents', *Molecular Imaging & Biology*, 5(6), pp. 376–389. Available at: https://doi.org/10.1016/j.mibio.2003.09.014.

Weinberg, R.A. (2013) *The Biology of Cancer*. W.W. Norton & Company. Available at: https://doi.org/10.1201/9780429258794.

Wesolowski, J.R., Rajdev, P. and Mukherji, S.K. (2010) 'Temozolomide (Temodar)', *American Journal of Neuroradiology*, 31(8), pp. 1383–1384. Available at: https://doi.org/10.3174/ajnr.A2170.

Williams, M.A. and Daviter, T. (eds) (2013) *Protein-Ligand Interactions*. Totowa, NJ: Humana Press. Available at: https://doi.org/10.1007/978-1-62703-398-5.

Wise, D.R. and Thompson, C.B. (2010) 'Glutamine addiction: a new therapeutic target in cancer', *Trends in Biochemical Sciences*, 35(8), pp. 427–433. Available at: https://doi.org/10.1016/j.tibs.2010.05.003.

Wu, Z. *et al.* (2014) '[^{18} F](2 *S* ,4 *S*)-4-(3-Fluoropropyl)glutamine as a Tumor Imaging Agent', *Molecular Pharmaceutics*, 11(11), pp. 3852–3866. Available at: https://doi.org/10.1021/mp500236y.

Xia, W. *et al.* (2009) 'A functional folate receptor is induced during macrophage activation and can be used to target drugs to activated macrophages', *Blood*, 113(2), pp. 438–446. Available at: https://doi.org/10.1182/blood-2008-04-150789.

Xu, S. *et al.* (2020) 'Immunotherapy for glioma: Current management and future application', *Cancer Letters*, 476, pp. 1–12. Available at: https://doi.org/10.1016/j.canlet.2020.02.002.

Xu, X. *et al.* (2018) 'Imaging Brain Metastasis Patients With 18F-(2S,4R)-4-Fluoroglutamine', *Clinical Nuclear Medicine*, 43(11), pp. e392–e399. Available at: https://doi.org/10.1097/RLU.0000000000002257.

Yelamanchi, S.D. *et al.* (2016) 'A pathway map of glutamate metabolism', *Journal of Cell Communication and Signaling*, 10(1), pp. 69–75. Available at: https://doi.org/10.1007/s12079-015-0315-5.

Zarei, M. *et al.* (2017) 'Posttranscriptional Upregulation of IDH1 by HuR Establishes a Powerful Survival Phenotype in Pancreatic Cancer Cells', *Cancer Research*, 77(16), pp. 4460–4471. Available at: https://doi.org/10.1158/0008-5472.CAN-17-0015.

Zha, Z. *et al.* (2018) 'Alanine and glycine conjugates of (2S,4R)-4-[18F]fluoroglutamine for tumor imaging', *Nuclear Medicine and Biology*, 60, pp. 19–28. Available at: https://doi.org/10.1016/j.nucmedbio.2018.02.001.

Zhou, R. *et al.* (2017) '[18F](2 *S* ,4 *R*)4-Fluoroglutamine PET Detects Glutamine Pool Size Changes in Triple-Negative Breast Cancer in Response to Glutaminase Inhibition', *Cancer Research*, 77(6), pp. 1476–1484. Available at: https://doi.org/10.1158/0008-5472.CAN-16-1945.

TURUN
YLIOPISTO
UNIVERSITY
OF TURKU

Painosalama, Turku, Finland 2023

ISBN 978-951-29-9337-6 (PRINT)
ISBN 978-951-29-9338-3 (PDF)
ISSN 0355-9483 (Print)
ISSN 2343-3213 (Online)